January 2022

Two Buried And Stacked Ice Masses Dated To Early And Late Pliocene; Ong Valley, Antarctica

Marie Bergelin

TWO BURIED AND STACKED ICE MASSES DATED TO EARLY AND LATE PLIOCENE; ONG VALLEY, ANTARCTICA

by

Marie Bergelin
Bachelor of Science, Bethune-Cookman University, 2014
Master of Science, University of Chicago, 2016

A Dissertation

Submitted to the Graduate Faculty

of the

University of North Dakota

in partial fulfillment of the requirements

for the degree of

Doctor of Philosophy

Grand Forks, North Dakota

May
2022

This dissertation, submitted by Marie Bergelin in partial fulfillment of the requirements for the Degree of Doctor of Philosophy from the University of North Dakota, has been read by the Faculty Advisory Committee under whom the work has been done and is hereby approved.

Jaakko Putkonen

Ronald Matheney

Gregory Vandeberg

Alena Kubátová

This dissertation is being submitted by the appointed advisory committee as having met all of the requirements of the School of Graduate Studies at the University of North Dakota and is hereby approved.

Chris Nelson
Dean of the School of Graduate Studies

Date

PERMISSION

Title	Two buried and stacked ice masses dated to Early and Late Pliocene; Ong Valley, Antarctica
Department	Harold Hamm School of Geology and Geological Engineering
Degree	Doctor of Philosophy

In presenting this dissertation in partial fulfillment of the requirements for a graduate degree from the University of North Dakota, I agree that the library of this University shall make it freely available for inspection. I further agree that permission for extensive copying for scholarly purposes may be granted by the professor who supervised my dissertation work or, in his absence, by the Chairperson of the department or the dean of the School of Graduate Studies. It is understood that any copying or publication or other use of this dissertation or part thereof for financial gain shall not be allowed without my written permission. It is also understood that due recognition shall be given to me and to the University of North Dakota in any scholarly use which may be made of any material in my dissertation.

Marie Bergelin

May 5, 2022

TABLE OF CONTENTS

LIST OF FIGURES

LIST OF TABLES

ACKNOWLEDGEMENT

First and foremost, I would like to express my deepest appreciation to my advisor and mentor, Jaakko Putkonen, who has provided guidance, support, and inspiration during my pursuit and completion of this degree. Jaakko has taught me to go beyond just a doctoral degree and has motivated me to reach for my full potential in ways that I did not think possible, and for that, I am forever grateful. I could not have asked for a better advisor throughout this process, and I look forward to continuing to work with Jaakko in my next endeavors.

I cannot begin to thank Greg Balco and Daniel Morgan enough for their guidance and support. They have been a pure inspiration and motivation. Our many long conversations have always brought me excitement towards this project and have inspired me to continue exploring the world of cosmogenic nuclides.

I thank the National Science Foundation, Harold Hamm School of Geology and Geological Engineering, and the University of North Dakota Graduate Studies for financially supporting my doctoral degree and providing this unforgettable journey. Further, I thank the Polar Geospatial Center for providing satellite images of Ong Valley.

I am grateful to my collaborators, Lee Corbett and Paul Bierman. They have welcomed me multiple times to their cosmogenic nuclide laboratory at the University of Vermont and edited various drafts for publications. In particular, Lee Corbett has provided valuable knowledge

regarding the cosmogenic nuclide extraction process and support in writing the appending document describing this process and reasoning in great detail. I thank Grant Boeckman and Andrew Grant for the support and great times in Ong Valley and Sarah Sturges for her delicious cooking. I thank Polar Engineer Thomas Nylen and Marianne Okal at UNAVCO, who assisted with processing the GNSS data and increasing the accuracy of the measurements. I thank my committee members Ronald Matheney, Gregory Vandeberg, and Alena Kubatova for their guidance and feedback.

I want to express great thanks to the faculty, staff, and students of the Geology and Geological Engineering Department at the University of North Dakota for all the valuable times spent in the classrooms, laboratories, hallways, and on the many unforgettable field trips; all which ultimately have had a significant impact on my success.

Last but not least, none of this would have been possible without the continuous support from my family and friends. For that I am forever grateful.

ABSTRACT

A debris rich ice core was collected from a buried ice mass in Ong Valley, located in Transantarctic Mountains in Antarctica. Measured cosmogenic nuclide concentrations in quartz obtained from the ice core were used to determine the age of the buried ice mass and infer the processes responsible for the emplacement of the debris currently overlaying the ice. Such ice masses are valuable archives of paleoclimate proxies; however, the preservation of ice beyond 800 kyrs is rare and therefore much effort has been recently focused on finding ice that is older than 1 Ma. In Ong Valley, the large, buried ice mass has been previously dated at > 1.1 Ma. In order to further constrain the age, this research focuses on a novel forward model that predicts the accumulation of the cosmic-ray produced nuclides ^{10}Be, ^{21}Ne, and ^{26}Al in quartz in the Ong Valley englacial and supraglacial debris.

Large observed downcore variation in measured cosmogenic nuclide concentrations suggests that the englacial debris is sourced both from subglacially-derived material and recycled surface debris that has experienced surface exposure to cosmic rays prior to entrainment. Modeled results show that the upper section of the ice core is 2.95 +0.18/-0.22 Myrs. The average ice sublimation rate during this time period is 22.86 +0.10/-0.09 m Myr^{-1}, and the surface erosion rate of the debris is 0.206 +0.013/-0.017 m Myr^{-1}. Burial dating of the recycled paleo surface debris suggests that the lower section of the ice core belongs to a separate, older ice mass which is estimated to be 4.3-5.1 Myrs old. The ages of these two stacked, but temporally separate ice masses

can be directly related to glacial advances of the Antarctic ice sheet and potentially coincide with two major global glaciations during the early and late Pliocene Epoch when global temperatures and CO_2 were higher than present. These ancient ice masses represent new opportunities for gathering information on past climates.

CHAPTER 1
INTRODUCTION

Over the last decades, anthropogenic warming has led to shrinking of terrestrial ice, which continues to melt at an accelerating rate (IPCC, 2022). As a result, ice sheets and glaciers have lost mass at an increasing rate which subsequently causes a rise in the global sea level. The processes that lead to the loss of terrestrial ice are complex, but of utmost importance for predicting how terrestrial ice cover will change in the future. While glaciers are currently the most significant contributors to sea level rise, the Antarctic Ice Sheet (AIS) has the potential to be the dominant contributor and controlling component of sea level predictions in the near future (Kopp et al., 2014).

Antarctica holds Earth's largest ice sheet that is divided by the Transantarctic Mountains (TAM) into the East and West Antarctic Ice Sheets. Complete melting of the West Antarctic Ice Sheet (WAIS) would result in a global sea level rise of 3-5 m. The larger, East Antarctic Ice Sheet (EAIS) contains a sea level equivalent of ~53 m (Fretwell et al., 2013).

The sensitivity of these ice sheets to global warming is uncertain. Although it is generally accepted that glacial ice will melt and increase sea level, recent research suggests a more complex response. DeConto et al. (2021) found that the AIS would remain relatively stable if global temperature rise is kept < 2 °C. However, exceedance of this threshold could lead to collapse of

the WAIS, resulting in a rapid sea level rise. On the contrary, Edwards et al. (2021) indicate that the AIS does not show a clear dependence on global warming and compensating factors may balance mass loss and mass gain. This indicates a more resilient AIS and therefore much less sea level contribution. Both these future sea level model predictions include modeled configuration of the past AIS. In particular, this includes modeled ice sheet configuration that occurred during the Pliocene Epoch (5.3-2.6 Ma), where both global surface temperature and atmospheric CO_2 levels were higher than present (Pagani et al., 2010; Seki et al., 2010) and is considered an analog for future anthropogenic warming. However, the exact configuration of the AIS during the Pliocene Epoch remains uncertain as proxy records provide contradictory evidence, leading to vastly different interpretations (Dolan et al., 2018).

Research on the extent and volume of the AIS during the Pliocene may aid in constraining the potential changes in ice volume and sea level caused by future deglaciation (DeConto et al., 2021; Edwards et al., 2021). Since the development of cosmogenic nuclides as an exposure dating technique, many ice-free areas containing glacial deposits have been studied to provide constraints on the past AIS extent. For example, several moraines at Roberts Massif in central TAM have been dated to be ~3 Ma old, inviting the question of whether or not these moraines correspond to glaciations and ice sheet expansion during a Late Pliocene warming period (~3.3 – 3.0 Ma) (Balter-Kennedy et al., 2020). Direct evidence, such as exposed moraines, can provide constraints on the timing and extent of a larger than present ice sheet. However, any evidence of a smaller ice sheet would be concealed below the present ice sheet surface (Balco, 2015). The more widely available indirect evidence from marine sediment and benthic foraminiferal isotopes can reflect ice sheet volumes, but not the exact configuration. Limited direct evidence of glacial deposits and the

primarily dependence of proxy records provide poor constraint on the past AIS. Therefore, little is known about the temporal extent and configuration of both the East and West AIS during the Pliocene Epoch (Balco, 2015).

Ice cores from glaciers and ice sheets are used as an archive for paleoclimate proxies, including: atmospheric gases, chemical compounds, and airborne particles (Castellano et al., 2004; Dansgaard et al., 1969; Fredskild and Wagner, 1974; Willerslev et al., 2007); however, the potential age of ice core records is limited by the fact that ice sheets are subject to deformation, ice flow, and basal melting. The oldest ice that has been recovered from the thickest parts of the AIS is 800,000 years old (Jouzel et al., 2007). Although it is hypothesized that ice up to 1-1.5 Ma may also exist at great depth in the ice sheet (Fischer et al., 2013), recovering this ice would be a complex and costly endeavor. Therefore, we currently lack direct archives of climate information that extend beyond ~0.8 Ma and into the Pliocene Epoch.

Bare ice is, in general, thermodynamically unstable under typical atmospheric pressure-temperature conditions and therefore prone to melt and/or sublimate. However, there exist regions of topographically constrained, extremely slow ice flow in which ice up to 2.7 Ma has been recovered near the surface (Yan et al., 2019). There are also several areas within the TAM where glacial ice is covered by supraglacial debris. A thick debris cover thermally insulates the ice surface and provides a physically plausible means of preserving near-surface ice for long periods. For example, Sugden et al. (1995) found glacier ice in Beacon Valley underlying a supraglacial debris containing an 8.1 Ma volcanic ash, leading them to conclude that the ice is older than 8.1 Ma. However, the antiquity of the Beacon Valley ice has been questioned on the basis of data

suggesting that ice lost to sublimation is dynamically replaced by ice flow from upstream glaciers, resulting in a situation where relatively young ice underlies relatively old debris (Hindmarsh et al., 1998; Ng et al., 2005; Stone et al., 2000; Van der Wateren and Hindmarsh, 1995). The lack of ice older than ~1 Ma severely limits our direct paleoclimate record and creates uncertainties when modeling future climate predictions which include modeled configuration of the past AIS (Bulthuis et al., 2019; Noble et al., 2020), especially during the critical Pliocene Epoch, where great uncertainty persist on the extent of the AIS (Dolan et al., 2018; Haywood et al., 2009).

In Ong Valley, Miller Range, TAM, a mass of glacier ice at least several tens of meters thick is found buried underneath <1 m of supraglacial debris. Cosmogenic nuclide measurements from the supraglacial debris suggest an age of >1.1 Ma, but most likely >1.8 Ma (Bibby et al., 2016). We have therefore collected a 944 cm long ice core from this buried ice mass and use concentrations of the cosmogenic nuclide, ^{10}Be, ^{21}Ne, and ^{26}Al from the englacial debris to further constrain the age of the ice mass.

Our goal is to determine the age of the ice, understand its overall geologic history, and evaluate its potential use as a paleoclimate archive. First, we mapped the glacial moraines and drift boundary, and then measured the movement of eight boulders found on the surface of the drift system, in order to evaluate the stability of this buried ice mass and associated drift system. Second, we apply cosmogenic nuclide dating to determine the age of the buried ice mass and present a novel dating application of cosmogenic nuclides which aims to quantify a complex exposure history of this buried ice mass. By comparing measured cosmogenic nuclide concentrations from the englacial and supraglacial debris with modeled concentrations, the nuclide inventory inherited

from prior exposure can be distinguished from that produced after ice emplacement. We then apply a cosmogenic-nuclide burial dating method to the inherited inventory as an age constraint, and show that two sections of the ice core contain recycled surface debris that can be burial-dated. We find that the upper section of the buried ice mass is ~3 Ma, which we interpret as the emplacement age of the bulk of the buried ice. The lower section has a significantly older burial age of > 4 Ma, and we interpret it as a portion of an older ice mass either *in situ* or transported during emplacement of the younger ice.

CHAPTER 2
GEOLOGIC HISTORY OF THE ANTARCTIC CONTINENT

2.1 The Antarctic Continent

The Antarctic continent is centered within a larger tectonic plate and generally surrounded by passive margins and oceanic lithosphere. The continent itself consists of two primary tectonic regions, 1) East Antarctica, and 2) West Antarctica, with its associated West Antarctica Rift System. These two tectonic regions are separated by a mountain belt known as the Transantarctic Mountains (TAM) (Fig. 2.1). The ice sheet dynamic of East and West Antarctica differs and are controlled by the tectonic differences between them. This in turn controls their sensitivity to climatic forcing.

The East Antarctic region consists of a tectonically stable, coherent, continental crust that is generally 35-45 km thick, with topographically high elevations below the ice sheet (Cogley, 1984). The continental lithology is dominated by several, generally accepted, Precambrian cratons (> 550 Ma) with margins of at least four orogenic belts that in parts consist of gneiss (Summarized in Talarico et al., 2022).

In contrast, West Antarctica is a geologically complex region and less tectonically stable. The continent consists of multiple low-lying, younger crustal blocks with a general thickness of 20-35 km. These crustal blocks are essentially an assemblage of four micro continents: Antarctic

Peninsula, Thurston Island, Ellsworth-Whitmore mountains, and Marie Byrd Land. Each block, has a separate geological history, developed in parts by a paleo-pacific subduction zone on the margin of the supercontinent Gondwana around 550-180 Ma (Fig. 2.2) (Jordan et al., 2020). The West Antarctic Rift System extends through the interior of West Antarctica and is bordered by the TAM and the Marie Byrd Land. This crustal rift mostly developed during the late Mesozoic (Behrendt et al., 1991), and is the reason for the volcanic activity in the region. In a study by Behrendt (2013), two active subglacial volcanoes have been suggested to potentially affect the WAIS. Further, the low-lying crust results in the bed of the WAIS being grounded below sea level, making it a marine-based ice sheet. This younger, low-lying, and tectonically active crust results in a WAIS dynamic that is less stable and more sensitive to tectonic and climatic forcing compared to the EAIS. These differences will be discussed in greater detail in subsequent sections.

The TAM are approximately 2500 km long and 200 km wide mountain belt that extends from the coast of the northern Victoria Land to the Pensacola Mountains near the Weddell Sea. Active rifting and uplift of ~6 km have shaped the TAM since the Early Cenozoic Era. The mountain peaks currently rise to the elevation of 4.5 km above sea level, reflecting a complex geologic history and lithologies varying in ages from approximately 3 Byrs to recent time. Much of its geology and history is hidden under the EAIS or outlet glaciers which flow across the mountain belt and into the Ross Bay. These outlet glaciers typically occupy large-scale fault structures that have developed from tectonic activities. The relationship between such tectonic activity and glacial erosion have influenced the topography of the mountain range (Kerr and Huybrechts, 1999).

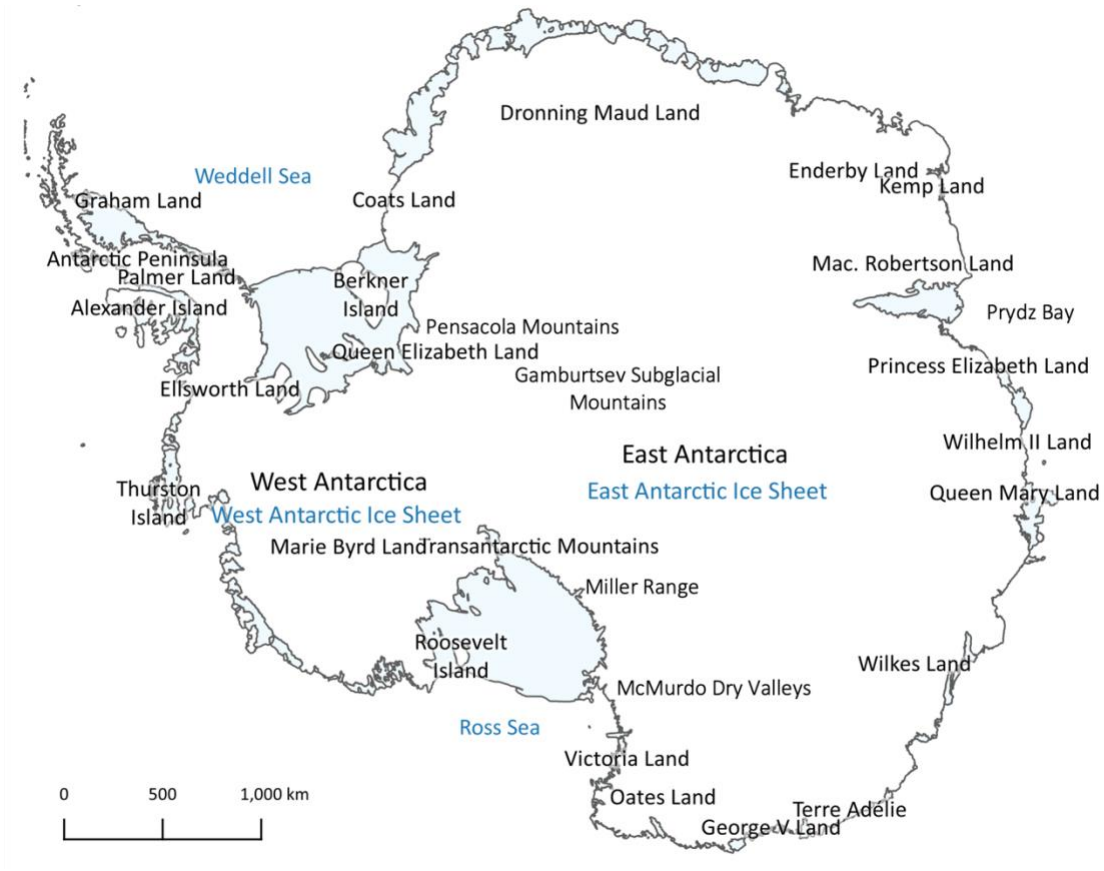

Figure 2.1 Map of Antarctica.

2.2 Continental Evolution of Antarctica

The Antarctic continent started its path to isolation when the supercontinent Gondwana began to rift apart at around 200 Myrs ago during the Early Jurassic Period (Fig. 2.2). Over a span of approximately 150 Myrs it became separated from the currently existing continents: South America, Africa, India, Australia, and New Zealand. The Antarctic continent took its position at the south pole around the Early Cretaceous (~100 Ma) (Lawver et al., 1992), where the fossil records show the presence of a subtropical climate during much of the Jurassic (~201-145 Ma) and Cretaceous Period (~145-66 Ma), with mean temperatures above freezing (Francis et al., 2007).

During the Eocene (~56-34 Ma) the climate shifted from a subtropical to a more temperate climate (Dingle and Lavelle, 1998). The presence of *Nothofagus* (southern Beeches) in the plant records indicates that temperatures cooled and a strong seasonal climate was implied with winter temperatures below freezing (Francis et al., 2007). Tectonically, this is a period where the Indian ocean is fully opened, the Tasmanian passage is forming deep ocean circulations, and the opening of the Drake passage is initiated (Lawver et al., 1992). Such opening of the continuous ocean surrounding the Antarctic continent, provides the cooling effect that leads to a climatic shift. Further, this is also the period when the TAM were uplifted (Goodge, 2020). Combined, a persistent cooling of temperatures and opening of the Drake passage resulted in an Antarctic glaciation and development of a large ice sheet at the Eocene-Oligocene boundary (~34 Ma) (Kennett et al., 1975; McKay et al., 2016; Zachos et al., 2008).

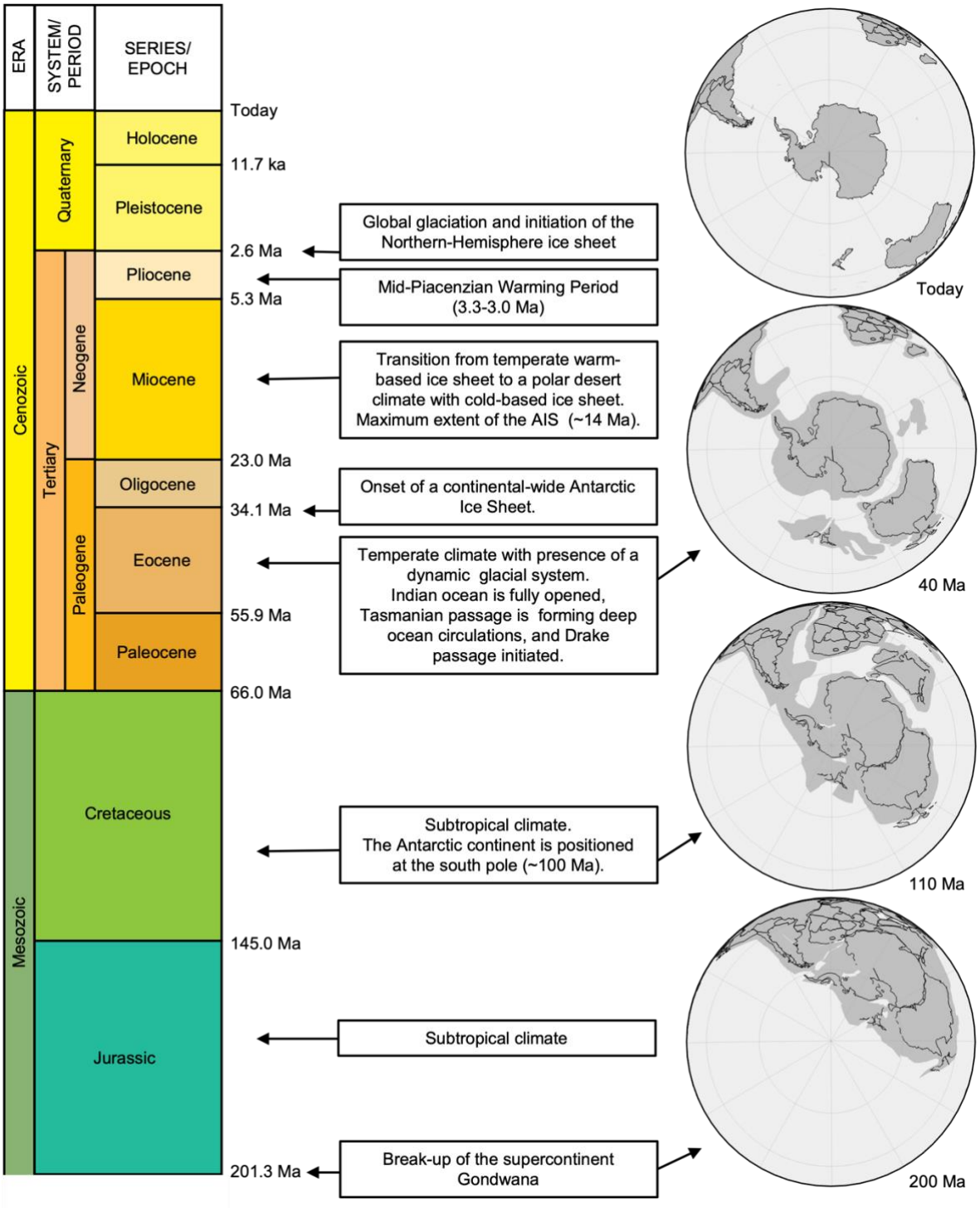

Figure 2.2 Geologic time scale with major events during the evolution of the Antarctic continent. The geologic time scale is modified from the U.S Geological Survey (USGS, 2016). The plate tectonic reconstruction is generated through GPlates software using the PALEO MAP project (Scotese et al., 2018) and follow the reconstruction of Cao et al. (2017). The tectonic plate reconstruction is shown for 200 Ma, 110 Ma, 40 Ma and current time, where grey shade show paleo plate configuration with current continental boundaries outlined in black.

CHAPTER 3
GLACIAL HISTORY OF ANTARCTICA

3.1 Glaciations Since the Eocene Epoch

The onset of the Antarctic glaciation and the presence of the widespread ice sheet have been known to occur at the Eocene-Oligocene transition (~34 Ma). However, alpine glaciers have been found to exist prior to that boundary. Numerical modeling of the present subglacial topography has shown that both the Queen Maud Land and Gamburtsev Mountain region were once high elevation orogenic mountain belts. Along with the TAM, these high elevations were most likely sites for the first alpine glaciers to form (Bo et al., 2009; Deconto and Pollard, 2003; Ferraccioli et al., 2011). This is believed to have occurred prior to the development of the EAIS, sometime between the Late Cretaceous and Eocene Epoch (100 Ma to 34 Ma)(Rose et al., 2013). The uplift of the TAM around this time provided a growing buttress and restriction for ice flowing toward West Antarctica and into Ross Sea. Further, these ancient mountains are believed to be the nuclei for the early and highly dynamic, temperate glacial system that has expanded and contracted to orbital forcing. During this time, minimized summer insolation caused by either reduced obliquity, low eccentricity, or timing of precession during period of relatively high eccentricity has been linked to ice growth on a cycle of a few hundred thousand years (Zachos et al., 2001). Such dynamic glacial system persisted until the occurrences of a continental wide ice sheet at ~34 Ma (Deconto and Pollard, 2003).

The initiation of a large scale AIS has long been attributed solely to its gradual thermal isolation caused by the tectonic opening of the oceanic pathways and the development of the Antarctic Circumpolar Current (Zachos et al., 1992). While this undoubtfully cooled the continent, a decline in atmospheric CO_2 through the Paleogene may have had a more significant impact and is now considered a fundamental factor (Deconto and Pollard, 2003). This decrease in CO_2 led to a gradual cooling and lowering of the snow line, to which the ice sheet extent eventually became limited by the continental shoreline.

Both the West and East Antarctic marine basins were largely above sea level during the Eocene-Oligocene transition and therefore a terrestrial ice sheet formed, as distinct from the current marine-based ice sheet (Paxman et al., 2019). A terrestrial ice sheet is much less sensitive to changes in the oceanic heat flux compared to today, and therefore a high elevation, terrestrial ice sheet requires less cooling to sustain. This means that, although the global mean temperature was much warmer 34 Myrs ago than it is today, the AIS could have hosted a larger volume of terrestrial ice (Wilson et al., 2013). In addition, much of the mass of a marine-based ice sheet is already displaced in the ocean, compared to a terrestrial ice sheet. Therefore, a fluctuation in the past terrestrial ice sheet would have had a much greater impact on the sea level compared to a today.

Ice-sheet modeling, ocean cores and stratigraphic evidence suggest that for a period of 20 million years following the Eocene-Oligocene boundary (34-14 Ma), the AIS has continued to be affected by orbital forcing, CO_2 and temperature variations (Bo et al., 2009; Deconto and Pollard, 2003; Naish et al., 2001). As a response, the AIS volume has therefore oscillated between states

of both larger and smaller than present. Such environmental conditions resemble that of the unstable Northern Hemisphere Ice sheet in the past 2.5 Myrs (Naish et al., 2001). In addition, this was a period in which global mean temperatures were 3-4°C warmer than today and where a tundra biota was present at high elevations in Antarctica (Lewis et al., 2007).

Another significant change in the Antarctic climate occurred during the mid-Miocene Epoch (~14 Ma). During this time, the marine isotopes indicate a sea surface cooling of 6-7°C (Shevenell et al., 2004). This cooling resulted in a transition from a temperate, warm-based glacial ice sheet to that of a polar desert climate, and cold-based glacial ice as observed today, in which limited weathering and erosion has occurred (Denton and Sugden, 2005). Since then, there has been an overall decrease in the size of the AIS, with proxy records suggesting potential significant retreat during past warming periods, such as the mid-Piacenzian warming period (mPWP) (3.3-3.0 Ma).

However, while the AIS is overall decreasing, the stability of the WAIS since the mid-Miocene (~14 Ma) is still of debate and may have experienced multiple collapses during the Pliocene, and again at ~1 Ma (Pollard and Deconto, 2009; Spector et al., 2018, and references therein). Exposure dating has found the most recent glaciation and, therefore, the Last Glacial Maximum (LGM) to have reached ~45 m above current ice sheet elevations (Ackert et al., 1999).

3.2 Glaciations in the Pliocene Epoch

The Pliocene Epoch (5.3-2.6 Ma) is a period where Earth's global climate transitioned from a relatively warmer to a cooler climate of the Pleistocene. In general, the Pliocene is considered an analogue for current anthropogenic warming with global temperature of 2-3 °C warmer than present and atmospheric CO_2 concentrations between 350 and 430 ppm, compared to current levels of ~420 ppm (Pagani et al., 2010; Seki et al., 2010). Only limited direct evidence from glacial deposits in Antarctica are available. Therefore, the exact configuration of the AIS during this period is debatable, as much of the information stems from proxy records such as marine sediment cores. Here, a short summary is provided of what is generally known about the AIS during this critical period.

While the AIS has overall decreased since mid-Miocene (~14 Ma), small amplitudes of glacial/interglacial variation has occurred and caused fluctuations in the cold-based, polar desert ice sheet during the Pliocene. The change in ice sheet volume is much less prominent in the EAIS compared to the WAIS which is more sensitive to climatic changes (Gohl et al., 2021).

Both marine sediment cores and terrestrial glacial deposits provide evidence of two, globally recognizable glaciations identified in the southern hemisphere (summarized in De Schepper et al., 2014); one occurring during the early Pliocene (4.9-4.8 Ma), and another during the Late Pliocene (~3.3 Ma), also identified as the Marine Isotope Stage (MIS) M2 glaciation. The latter is followed by a warmer-than present mPWP (~3.3-3.0 Ma) (De Schepper et al., 2014; Dowsett et al., 2016; Haywood et al., 2013), which ends with the Late Pliocene cooling, post ~3

Ma, leading to a global glaciation around the Pliocene-Pleistocene transition (De Schepper et al., 2014).

The Early Pliocene glaciation (4.9-4.8 Ma) is recorded both in the marine cores and terrestrial glacial deposits in the northern hemisphere and from Patagonia, making this the first early Pliocene bipolar glaciation (De Schepper et al., 2014). The ice sheet volume is inferred to be similar to or slightly larger than present (Naish and Wilson, 2009), however the cause of this global glacial expansion is still unclear (De Schepper et al., 2014).

This Early Pliocene glaciation is followed by a prolonged warming and decrease in the EAIS from ~4.6 to 4.0 Ma, recorded by a decrease in ice-rafted debris accumulation from Prydz Bay marine cores (Passchier, 2011). A peak warming occurred during this interglacial at 4.2 Ma (Golledge et al., 2017; Pagani et al., 2010). Modeling of the sensitivity of the AIS indicates a contribution to global sea level of ~8.5 m (Golledge et al., 2017) . Such contribution is primarily from partial or complete collapse of the WAIS driven by ocean thermal forcing, and secondarily from long-term surface lowering of the EAIS driven by atmospheric warming (Pollard and Deconto, 2009).

The second global glaciation during the Pliocene, is known as the Marine Isotope Stage (MIS) M2 (3.3 Ma), which terminated the early Pliocene warming period, and led to major expansion of the AIS with sea surface cooling of 2.5 °C. This cooling is observed in both the northern hemisphere glacial deposits and benthic isotopes from marine cores (De Schepper et al., 2014). The initiation of this cooling and subsequent glaciation has been linked to strengthening of

westerly winds and changes in ocean circulations (McKay et al., 2012). In a study by Yamane et al. (2015), cosmogenic nuclide exposure ages coupled with ice sheet modeling where used to suggest that the interior ice sheet could have been up to 600 m thicker and therefore higher in elevation sometime during the Pliocene and at least once prior to 3 Ma.

Modeling of the mPWP suggests a relative increase in temperature and atmospheric CO_2, and closely resembling that of modern anthropogenic warming (Haywood et al., 2016). Further, there is a general agreement of ice sheets retreat to a sea level equivalence of 15-28 m, in which the upper bound requires a complete collapse of WAIS and melting of the marine-based glaciers of the EAIS (Colleoni et al., 2022, and references herein). However, the exact configuration of the EAIS during this warming period is still uncertain (Balco, 2015).

The Pliocene Epoch terminates with a global cooling and decrease in atmospheric CO_2 from ~400 to ~280 ppm, where an increased AIS is recorded in diatomite and benthic isotopes from marine cores (McKay et al., 2012). The cooling is believed to be a continuation of the MIS M2 cooling between 3.3 and 2.6 Ma, where progressive increase in obliquity and closing of the Isthmus of Panama (linking of the South and North American continents) caused a change in oceanic circulation. Subsequently, this led to an initiation of the Northern Hemisphere ice sheet expansion and global glaciation at the Pliocene-Pleistocene transition at ~2.6 Ma (Haug and Tiedemann, 1998).

3.3 The Ice Sheet Debate, and Climate Model Predictions for the Pliocene Epoch

Terrestrial records of past glaciations are scattered and difficult to interpret, resulting in difficulties for conclusions on the nature, timing, extent, and evolution of the AIS (Dolan et al., 2018). This creates great uncertainties when modeling future climate predictions which include modeled configuration of the past AIS (Bulthuis et al., 2019; Noble et al., 2020). The uncertainty regarding the AIS started in part with the discovery of the Sirius Group deposit (Mercer, 1972). The Sirius Group is a glacial deposit of diamict that was initially believed to be deposited during the Queen Maud Glaciation, occurring > 4.2 Myr ago (Mayewski, 1975) and can be traced throughout the TAM at both higher and lower elevations. The presence of fossilized vegetation suggests that the Sirius Group was deposited during a period of temperate glaciation.

In the past few decades there has been great controversy regarding the age of the Sirius Group deposit and therefore, the response of the AIS during a warmer Pliocene Epoch. This has led to two main views. One, is the view of a stable ice sheet, the 'stabilist'. Exposure dating of the Sirius Group has been found to predate the Pliocene Epoch (Ivy-Ochs et al., 1995) with an age of > 10 Ma, in some locations (Balter-Kennedy et al., 2020; Schäfer et al., 1999). The preservation of these deposits since the mid-Miocene has led to the view of the EAIS remaining stable and cold since then (Denton et al., 1993).

The other view is that of the 'dynamist' and initially presented by Webb et al. (1984). This view relies on the dating of Sirius Group sediment using diatoms and suggesting a mid-Pliocene

age (~3 Ma). This view suggests that the EAIS was much reduced and that the WAIS had collapsed, which subsequently resulted in massive sea level rise.

A more recent debate is that of the Late Pliocene, which stems from the Sirius debate and has led to two hypotheses regarding the resilience of the EAIS during the mPWP. One, is that the EAIS were similar or slightly larger than current (Sugden et al., 1993; Winnick and Caves, 2015), which is possible due to increased precipitation under warmer atmospheric conditions (Frieler et al., 2015). The other, is that the EAIS was significantly smaller that today (Scherer et al., 2016; Webb et al., 1984) with enhanced retreat along the margins and associated collapse of the WAIS (Deconto and Pollard, 2016). However, the exact configuration and changes in the AIS remains unknown as most of the evidence for a lower AIS would be hidden below the current ice surface (Balco, 2015)

Given the sparsity of direct evidence on Pliocene glacial dynamics, ancient, buried ice masses may provide critical limitations on the possible mPWP amplitude, as the ice would have melted if large enough warming had occurred. Thus, the survival of the ice can be used for numerical estimates of the limits of such warming.

CHAPTER 4
DEBRIS-COVERED GLACIERS AND BURIED ICE MASSES IN ANTARCTICA.

A debris-covered glacier, also referred to as a rock glacier, is generally a glacier in which large parts of its surface area is covered by a layer of rock debris, including ash, dust, and sediment of various sizes (Cogley et al., 2010). While globally distributed, the majority of debris-covered glaciers are found in rapidly eroding alpine landscapes such as Alaska, the Alps, the Himalayas, North and South East Asia, and New Zealand (Herreid and Pellicciotti, 2020). In recent decades the extent of debris cover has expanded due to the increase in the equilibrium line altitude, which enhances melting and, therefore, the accumulation of debris further up-glacier and thickening of debris cover down-glacier (Kirkbride and Deline, 2013). A thickening of debris cover is known to insulate the glacial ice and decrease the effect of ablation (Evatt et al., 2015; Kowalewski et al., 2011; Mihalcea et al., 2006; östrem, 1959). However, surface features such as ice cliffs, water channels, and ponds can enhance ablation (Ragettli et al., 2016). Therefore, the response of debris-covered glaciers to a warming climate is not well understood. In Antarctica, debris-covered ice is one of three main preservation mechanisms for old glacial ice (e.g., Bibby et al., 2016), which also includes basal ice at ice sheet domes (Jouzel et al., 2007) and blue ice at the TAM margins (Yan et al., 2019).

The debris, covering a glacier, can originate from various sources. Therefore, the formation of debris-covered glaciers varies greatly. Debris-covered glaciers are often formed by rockfalls

and/or rock avalanches from adjacent slopes being deposited on top of an active glacier which becomes buried and subsequently insulated from direct solar radiation. They can also form by freezing of surface water that infiltrates talus slopes (Luckman, 2007). Further, supraglacial debris can accumulate on the ice surface by exhumation of the englacial and subglacial debris in the ablation zone (Jennings et al., 2014; Kirkbride and Deline, 2013). In Antarctica, much of the ice sheet and glaciers contain minimal to nonexistent debris cover due to the lack of source slopes for rock falls. However, debris-covered glaciers and buried ice masses have been found in valleys that are otherwise free of exposed glacial ice.

In Antarctica, these debris-covered ice masses, such as those in Beacon Valley, McMurdo Dry Valleys, and in Ong Valley, are found to be remnants of stagnant glacier ice that has been sublimating slowly over long period of time. As the ice sublimates, englacial debris of the sublimating ice is slowly accumulating as a lag on the ice surface that is lowered. As this process continues, the debris layer at the surface becomes thicker and begins to shield the ice. A debris thickness greater than a few centimeters has been found to insulate the ice thermally and therefore limit its vapor loss (Evatt et al., 2015; Kowalewski et al., 2011; Mihalcea et al., 2006; östrem, 1959). This shielding and insulation are the main reasons why glacial ice underlying supraglacial debris in Ong Valley has been preserved for more than a million years (Bibby et al., 2016). In Beacon Valley, it should be noted that, there is a possible recharge of the underlying ice from a smaller, up valley, alpine glacier that results in younger ice underlying a much older supraglacial debris layer (Hindmarsh et al., 1998; Ng et al., 2005; Stone et al., 2000; Van der Wateren and Hindmarsh, 1995).

In order for debris to accumulate at the ice surface due to sublimation, a certain amount of englacial debris must exist within the glacial ice. There are multiple basal processes that cause such debris to be entrained. One process referred to as regelation is where ice melts and refreezes around subglacial sediment grains because of increased pressure of the overlying ice. This can cause the incorporation of thin, dense sediment layers extending tens of meters up into the basal glacial ice (Hubbard and Sharp, 1993). In another process, debris suspended in meltwater that moves along the ice-bed interface or in englacial fractures, can become supercooled by rapid decompression, resulting in laminated debris layers of varying thickness (Alley et al., 1998; Ensminger et al., 2001; Lawson et al., 1998). While these entrainment processes are mostly present in temperate glaciers, cold-based glaciers erode basal bedrock to a lesser extent and result in the entrainment of debris as well. This is caused by subfreezing, where interfacial water film causes sliding and therefore abrasion (Cuffey et al., 2000).

The ablation rate for a debris-covered glacier is found to decrease with increasing debris thickness (Evatt et al., 2015; Mihalcea et al., 2006; östrem, 1959). That is, in Antarctica, the sublimation rate would be expected to approach zero at some point in time. However, this is not the case. The debris layer above the glacier ice is commonly covered by patches of desert pavement, indicating that surface erosion has occurred to some extent. Thinning of the debris cover due to erosion allows for sublimation of the underlying ice to continue, and perhaps a balance is achieved between the long-term surface erosion and ice sublimation rate. Maybe such equilibrium is reached when a debris layer becomes ~0.5-1 m thick (Bibby et al., 2016; Mackay and Marchant, 2016; Sugden et al., 1995). This relationship between sublimation rate, debris thickness, and

erosion rates is not well constrained, and therefore an average sublimation rate is commonly reported for these deposits (Bibby, 2014; Morgan et al., 2010a, b)

CHAPTER 5
STUDY AREA

5.1 Prior Geomorphological Research and Surface Dating in the Transantarctic Mountains

The Transantarctic Mountains (TAM) in Antarctica are perhaps the least studied terrestrial area on Earth, and its exact glacial history is therefore poorly understood. This is in part due to its remoteness and hostile environment. Much of the prior research has been focused on glaciology, paleontology, bedrock geology, volcanology, and evolution of the continent, where only a handful of scientists initially studied the geomorphology, surface processes, and glacial geology (e.g., Ackert and Kurz, 2004; Bockheim et al., 1989; Bromley et al., 2010; Denton et al., 1989; Grindley, 1967; LaPrade, 1984; Mayewski, 1975; Mayewski and Goldthwait, 1986; Mercer, 1968; Todd et al., 2010).

The early geomorphic studies involved extensive mapping and stratigraphic correlation of glacial deposits in Antarctica. As part of these studies, four glacial deposits were found and correlated to glaciation, and subsequently traced through the TAM (Fig. 5.1). The oldest of these four deposits is known as the Sirius Group. The other three deposits are a set of younger lateral moraines referred to as Low, Middle, and High and correspond to the Amundson, Shackleton, and Scott glaciations (Mayewski, 1975). A similar set of lateral moraines has been identified at the Dominion range and named the Beardmore, Meyer, and Dominion drifts (Denton et al., 1989;

Mercer, 1972). These were later exposure-dated by Ackert and Kurz (2004) and range in ages from the Holocene (~10ka) to Late Pliocene (>2 Ma). The youngest deposit (Low moraine or Beardmore drift) is virtually unweathered (Denton et al., 1989) and has now been extensively exposure-dated to 10-18 ka at Reedy Glacier in the southernmost TAM (Fig. 5.1), and therefore deposited during the LGM (Todd et al., 2010).

Much exposure dating in Antarctica, since its development in the early 1990's, has been focused on solving geochronological problems arising from previous geomorphic and stratigraphic correlations such as those deposits described above. Specifically, exposure dating techniques were directed toward the glacial geology of the EAIS during the Miocene through Pleistocene Epoch, which is, in general, recorded by glacial deposits in the TAM (e.g. Denton et al., 1993; Stroeven and Prentice, 1997). Some of these deposits were dated and found to have been exposed at the surface for millions of years (e.g. Marchant et al., 1996). Exposure dating of these glacial deposits i) aid in quantifying the extremely low erosion rates responsible for the preservation of these ancient deposits, and ii) could provide geological evidence for the configuration of the EAIS from the Miocene through the Pleistocene, which has been debated since the finding of the Sirius Group (Bruno et al., 1997; Schäfer et al., 1999) and more recently for modeling of the future sea-level rise as discussed in previous sections.

Improvements in cosmogenic nuclides measurement made it possible to exposure date younger glacial deposits relating to the LGM. Therefore, part of the geomorphic studies in Antarctica were later aimed at reconstructing the elevation changes of the AIS from LGM through the Holocene. Much of this research involved exposure dating of glacial deposits where nunataks

were present (Ackert et al., 1999; Bentley et al., 2010; Johnson et al., 2008; Stone et al., 2003; Todd et al., 2010).

Today, various other moraines have been mapped and chronologically constrained throughout the TAM, including Southern Victoria Land (Brook et al., 1995; Brook et al., 1993; Brown et al., 1991; Bruno et al., 1997; Ivy-Ochs et al., 1995; Strasky et al., 2008), Law (Kaplan et al., 2017), Scott (Spector et al., 2017) and Reedy glaciers (Bromley et al., 2010; Todd et al., 2010) (Fig. 5.1). More recently, exposure dating of a series of moraines at Roberts Massif has revealed ages from 0.4 – 12.8 Myrs (Balter-Kennedy et al., 2020). The oldest and highest moraines at Roberts Massif, along with a compilation of all Antarctic exposure ages provide a maximum exposure age of mid-Miocene (14-15 Myrs ago) which also marks the transition to a polar desert climate that provides limited weathering and erosion processes as observed today (Denton and Sugden, 2005). Further, it has been shown that, since then, the ice sheet has never covered the highest nunataks along the TAM. (Spector and Balco, 2020; Spector et al., 2020).

In Ong Valley, a system of three drifts has been identified as young, middle, and old drift increasing in ages up valley from 11 kyrs to > 2.6 Ma (Bibby et al., 2016). However, limited age constraint on these three drifts make correlation difficult with other moraines and drifts found throughout the TAM.

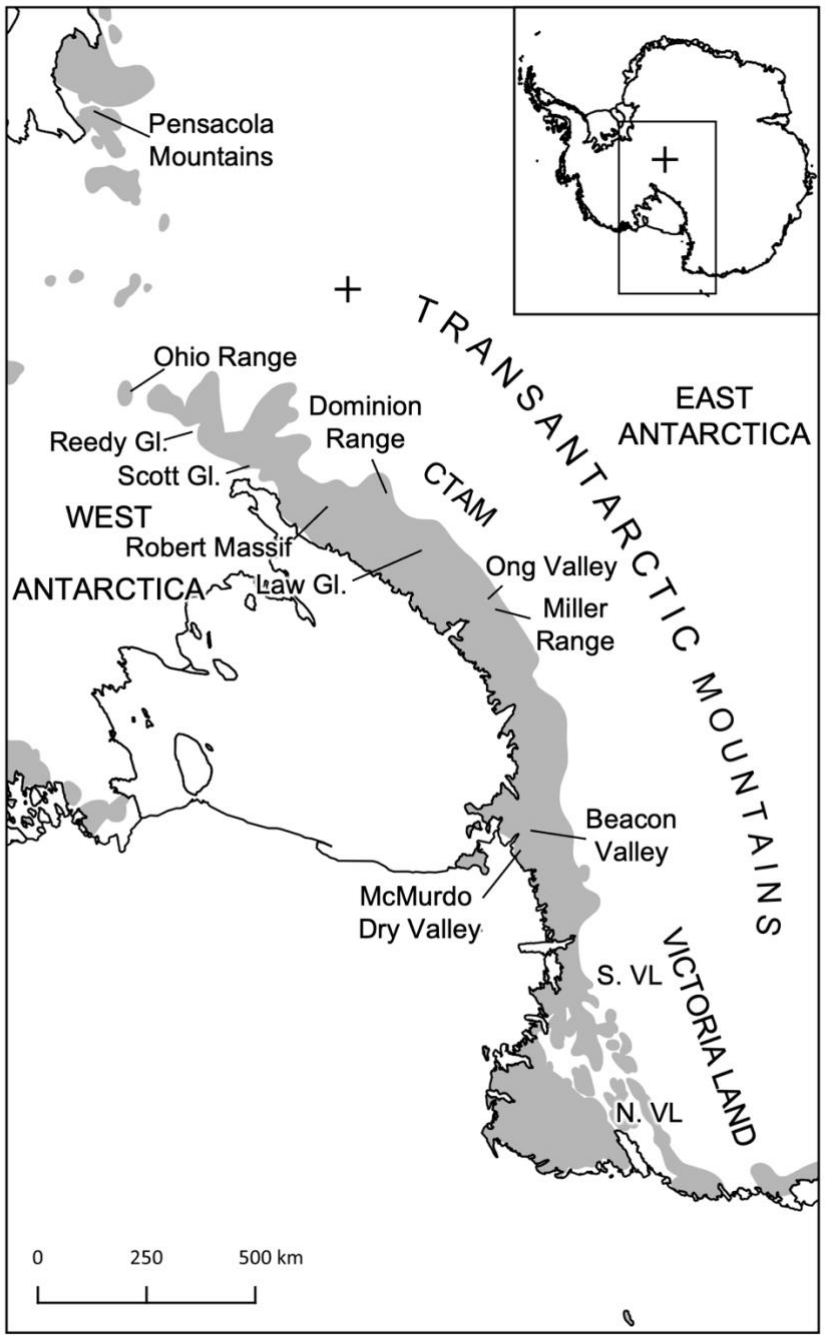

Figure 5.1 Map of the Transantarctic Mountains range. Grey shading indicates areas that have patches of exposed bedrock with place names referring to those mentioned in text.

5.2 Ong Valley

Ong Valley is a ~1.5 km wide and ~7 km long glacial valley located in the Miller Range of the central TAM, Antarctica (83.25°S, 157.72°E). The current valley floor gradually rises from an elevation of 1500 m above sea level (masl) to 1700 masl at the valley head. Over the span of one year (2011), the recorded air temperature in the valley ranged between -49.0°C and -4.0°C, with mean of -23.9°C (Bibby et al., 2016). In the head of the valley is a small alpine glacier, and the valley mouth is blocked by a 2 km wide exposed glacial ice front of the Argosy Glacier (Fig. 5.2).

The valley floor is mostly covered by a well-developed and distinctive system of three glacial drifts; referred to as young, middle, and old (Bibby et al., 2016) (Fig. 5.2 and Fig. 5.3). These deposits were first described in 1975 and later identified as soil chronosequences, increasing in age and maturity with distance from the Argosy Glacier (Mayewski, 1975; Scarrow et al., 2014). Bibby et al. (2016) found that the three drift units were ablation tills formed by sublimation of debris-rich glacier ice that advanced into the valley. Eventually the ice became stagnant and began to sublimate, which led the englacial debris to accumulate on the surface as supraglacial debris. Although some of the supraglacial debris in Ong Valley could originate from a rockfall or colluvium from adjacent slopes, the drifts either have convex topography (middle and younger drifts) or are bounded by prominent moraine ridges (older drift), and therefore significant input from local slopes is only possible immediately adjacent to valley walls. In addition, surfaces of active glaciers in the region uniformly lack significant surface sediment. While aeolian sediment

transport onto the drifts is possible, drift surfaces are mainly composed of clasts and boulders too large for aeolian transport.

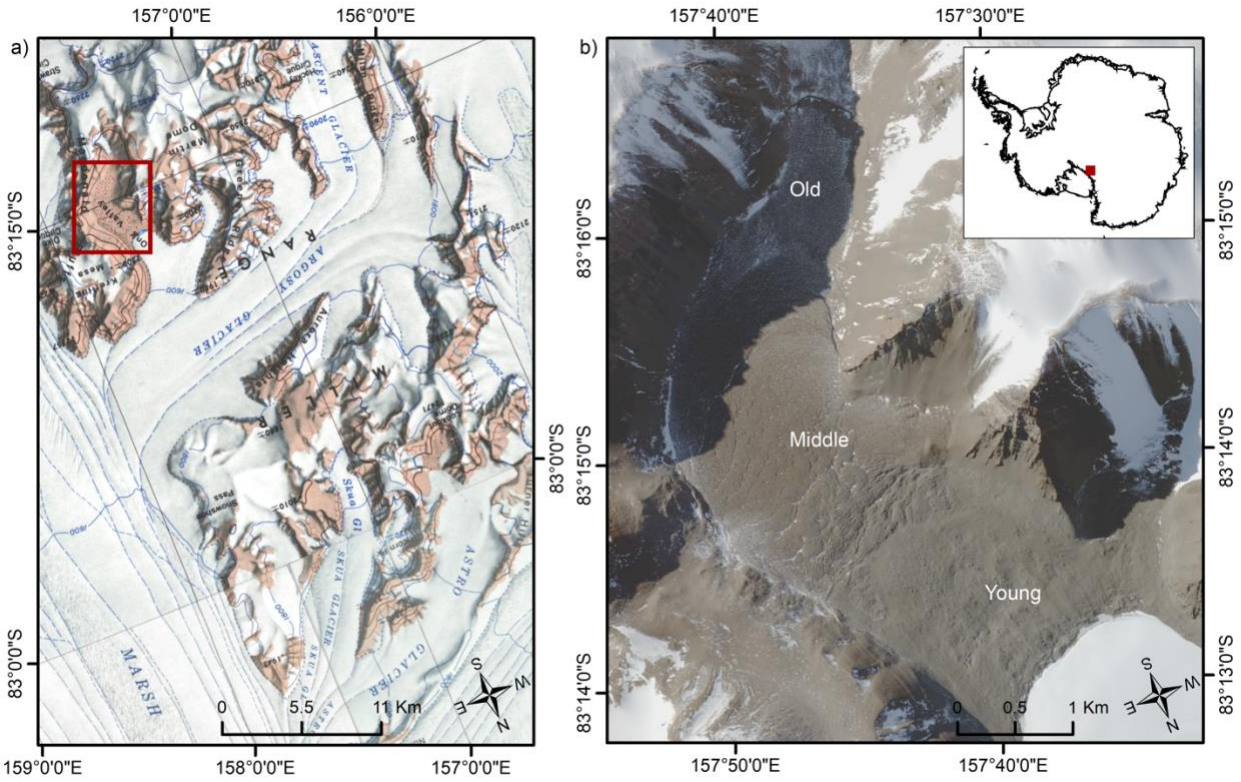

Figure 5.2 Location of Ong Valley. (a) Cropped USGS 1:250,000 scale topographic map of Miller Range, Antarctica, showing the location of Ong Valley. The red rectangle indicates the location of Ong Valley opening perpendicular to Argosy Glacier. (b) Worldview 2 satellite image of Ong Valley, Antarctica (© 2016 Maxar).

Exposure dating of the supraglacial debris from each drift has revealed the ages of 11-13kyr (young), >1.1 Myr (middle), and >2.7 Myr (old) (Bibby et al., 2016). The young and middle drift have buried ice under 0.1-0.5 m (young) and 0.6-0.8 m (middle) of loose supraglacial debris completely concealing the ice. In this paper we refer to the buried ice below the middle drift as the middle ice. Contrary, the oldest drift is devoid of buried ice, which, presumably, has sublimated over extended exposure (Bibby et al., 2016). The absence of buried ice is evident from the u-

shaped valley floor and pits reaching depths of 78 cm (Bibby et al., 2016). The highest surface elevation of these buried ice masses in the valley is located on top of the middle drift and ~200 m above the current Argosy Glacier surface elevation at the valley mouth. Bibby et al. (2016) used cosmogenic-nuclide data from the surface debris layer to estimate that sublimation rates of 19-23 m Myr^{-1} and surface erosion rates of 0.7-0.9 m Myr^{-1} have persisted where ice and debris is present in the valley since deposition of the drifts. All three drifts have related lateral moraines on the valley walls that trace the original elevation of the ice surface. The oldest drift also has a distinct end moraine close to the head of the valley, which shows no signs of influence from the small alpine glacier currently located at the head of the valley.

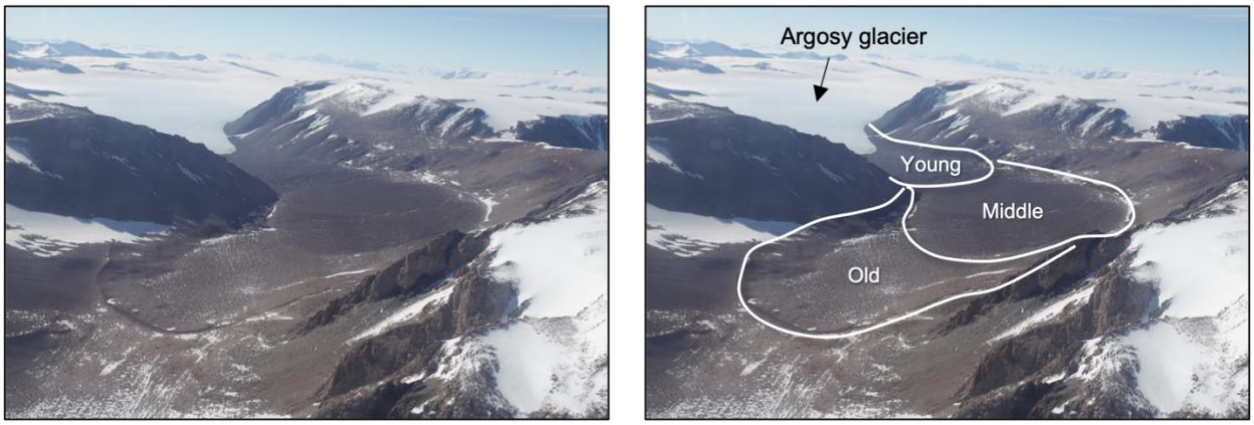

Figure 5.3 Oblique aerial photograph of Ong Valley (left) with added markings (right) indicating the young, middle, and old drifts (Bibby et al., 2016). The photograph is looking northward and down valley. The dots represent the sampling sites as identified in Fig. 5.2.

Major and minor mineral analysis of englacial debris and the supraglacial debris from each of the three drifts display a shared provenance significantly different from the local bedrock of Ong Valley (Edwards et al., 2014; Morgan et al., 2020). The local bedrock is primarily dominated by Hope Granite and Argosy Gneiss (Barrett et al., 1970). This indicates that these drifts were deposited by past advances of the Argosy Glacier.,

CHAPTER 6
THE DEVELOPMENT OF COSMOGENIC NUCLIDE DATING, AND ITS APPLICATIONS TO ANTARCTICA

Cosmogenic nuclide exposure dating uses the accumulation of cosmogenic nuclides to determine the near-surface exposure history of mineral matter. These cosmogenic nuclides are rare isotopes produced by cosmic-ray interactions with matter near Earth's surface and include the radioactive nuclides; ^{10}Be, ^{14}C, ^{26}Al, ^{36}Cl, ^{41}Ca, and ^{53}Mn, and the stable noble gas nuclides; ^{3}He, ^{21}Ne, ^{22}Ne, ^{36}Ar, ^{38}Ar and various Kr and Xe isotopes. Of these, ^{3}He, ^{10}Be, ^{21}Ne, ^{26}Al, and ^{36}Cl, are commonly used in Earth-science applications (Dunai, 2010). Among many other applications, if given a set of basic geological assumptions, measured cosmogenic nuclide concentrations in a sample can yield information about glacial events by determining the exposure age of that sample. Further, such dating methods can determine whether a sample has been subjected to erosion, and/or has experienced any short or long-term burial during its exposure history.

In this study, we use measured concentrations of the cosmic-ray-produced nuclides ^{10}Be, ^{21}Ne, and ^{26}Al in both the supraglacial debris covering the buried ice mass in Ong Valley and in debris within the buried ice. This was done in order to determine the age of the ice, its sublimation and erosion rate, and the geologic history of the englacial debris. Because the cosmic-ray flux is rapidly attenuated with depth, the concentration of cosmogenic nuclides can be used to date or quantify geologic processes that form or bury the supraglacial debris in Ong Valley.

The following subsections highlight important discoveries of terrestrial *in situ* produced cosmogenic nuclides, with focus on the nuclides of interest (^{10}Be, ^{21}Ne and ^{26}Al) for this study. Further, the various cosmogenic nuclide dating techniques used in this study are described. In following chapters, these dating methods are combined into a forward model and used to exposure date the buried ice mass in Ong Valley.

6.1 The Discovery of Cosmogenic Nuclides

Cosmogenic nuclide dating of glacial erratics was first explored in 1955 in a study of the *in situ* produced cosmogenic nuclide ^{36}Cl in rock surfaces (Davis and Schaeffer, 1955). It was then proposed that cosmogenic nuclides produced within mineral matter at Earth's surface could be applied to geological problems. Davis and Schaeffer (1955) were the first to suggest that erratic boulders carried by glaciers and deposited on moraines could potentially be used for dating purposes and correlated to glacial processes. Further, with a half-life of 0.3 Ma, ^{36}Cl was proposed to be a viable tool for studying glacial processes occurring during the Pleistocene Epoch (2.6Ma - 0.012Ma), covering the LGM.

A theoretical approach for the interaction of cosmic-rays in terrestrial mineral matter and the production rate of various cosmogenic nuclides was laid out by Lal and Peters (1967). However, it was not until the development of the Accelerator Mass Spectrometry (AMS) and the highly sensitive noble-gas mass spectrometry (MS) in the early 1980's that it became possible to routinely measure exceedingly low concentrations of *in situ* produced cosmogenic nuclides (Brown, 1984). Shortly after, the first measurements of terrestrial *in situ* produced ^{10}Be and ^{26}Al

were reported from the Libyan Desert quartz grains (Yiou et al., 1984). It was then suggested that there is a possibility to construct complex exposure scenarios when measuring a pair of nuclides due to the difference in their half-lives. As a result, an exposure history which includes surface erosion and a subsequent burial event was defined by Lal and Arnold (1985), and later explored as a continuation of the study on the Libyan desert quartz. Here, Klein et al. (1986) investigated the ^{10}Be and ^{26}Al ratios measured in quartz grains as a means for determining a sample's exposure, erosion and burial history. Later refinements by Lal (1991) resulted in an erosion model that can be used with either a single or pair of nuclides to obtain geomorphic information and has until today been widely used.

Some of these initial studies of ^{10}Be and ^{26}Al, and the suitability of using quartz as a target mineral, involved samples obtained from Allan Hills in Antarctica (Nishiizumi et al., 1986). These same samples were later used by Graf et al. (1991) for the first measurements of terrestrial produced ^{21}Ne. The use of the cosmogenic nuclide ^{21}Ne has important additional applications because, similar to ^{10}Be and ^{26}Al, it is produced in quartz. However, ^{21}Ne is a stable nuclide and can therefore provide additional age information compared to the ^{26}Al/^{10}Be ratio, which is limited by the shorter half-life of ^{26}Al (Table 6.1). Further, the ^{10}Be/^{21}Ne and ^{26}Al/^{21}Ne ratios can be used to resolve processes such as uplift and temporary coverage/burial by ice or other deposits (Graf et al., 1991).

Exposure dating of samples from Antarctica quickly became of interest, since glacial deposits were found to have been exposed at or near the surface for millions of years (Marchant et al., 1996). Due to its long surface exposure, these samples were expected to have extremely high

concentrations of cosmogenic nuclides that could be measured by AMS and noble-gas MS. Exposure dating of such deposits was important in developing cosmogenic nuclide techniques and provides consistency between other studies on long-term exposure (Balco, 2011).

6.2 Production of Cosmogenic Nuclides

Cosmogenic nuclides are produced predominantly by high-energy, secondary cosmic-ray particles. These cosmic-ray particles originate from the explosions of supernovas and constantly bombard Earth's surface. The high-energy particles enter Earth's atmosphere as primary cosmic rays that consist of protons and α-particles. When interacting with atmospheric matter, the primary cosmic rays cause a spallation reaction that releases a cascade of secondary cosmic-rays consisting of neutrons, protons, and muons. A significant amount of the secondary cosmic-ray neutron and muon particles reach Earth's surface producing terrestrial *in situ* cosmogenic nuclides (Lal, 1991). At the surface, the production of these nuclides is dominated by the spallation reaction caused by neutrons and only less than 1% are caused by muon production. However, at greater depth below the surface the production of cosmogenic nuclides is solely due to muons.

A spallation reaction is a nuclear reaction where a secondary, high-energy neutron collides with a target nucleus. This collision causes a nucleon (proton and/or neutron) to be ejected from the target nucleus. This reaction releases multiple particles such as protons, neutrons, and clusters of nucleons. The loss of mass results in the production of a lower mass cosmogenic nuclide (Gosse and Phillips, 2001). A spallation-produced nucleus maintains the direction of the impacting particle and continues to induce spallation in other target nuclei, resulting in a nucleus cascade.

The spallation reactions that cause the production of the cosmogenic nuclides ^{10}Be, ^{21}Ne and ^{26}Al are shown in Table 6.1.

Table 6.1 Reactions of the cosmogenic nuclides ^{10}Be, ^{21}Ne, and ^{26}Al in quartz and their half-lives.

Isotope	Half-life (Myr)	Spallation	Muon
^{10}Be	1.39	${}^{16}_{8}O(n,4p3n){}^{10}_{4}Be$ ${}^{28}_{14}Si(n,x){}^{10}_{4}Be$	${}^{16}_{8}O(\mu^-,\alpha pn){}^{10}_{4}Be$ ${}^{28}_{14}Si(\mu^-,x){}^{10}_{4}Be$
^{21}Ne	Stable	${}^{28}_{14}Si(n,x){}^{21}_{10}Ne$	${}^{28}_{14}Si(\mu^-,\alpha 2n){}^{21}_{10}Ne$
^{26}Al	0.71	${}^{28}_{14}Si(n,p2n){}^{26}_{13}Al$	${}^{28}_{14}Si(\mu^-,2n){}^{26}_{13}Al$

The abundance of secondary neutrons decreases with atmospheric depth defined by its attenuation length. The attenuation length is the change in energy a particle experience as it travels through matter and is dependent on mass depth (g cm^{-2}) and is therefore the same for the atmosphere and lithosphere. The attenuation length is defined as the distance in which the energy of a particle decreases by a factor of e^{-1} and ranges from 140 g cm^{-2} near the poles to 180 g cm^{-2} at lower latitudes (Balco et al., 2019; Gosse and Phillips, 2001). By the time the cascade of secondary neutrons reaches Earth's surface the energy decreases, and so the spallation reaction and therefore the production of cosmogenic nuclides due to spallation decreases rapidly with depth below Earth's surface.

While muons are shorter lived particles, their attenuation length is much longer as they have a much weaker interaction with atomic matter compared to spallation. For those reasons muons are much more abundant at the surface. However, because muons have a lower production rate in matter, the spallation nucleon components dominate cosmogenic nuclide production at the

surface, whereas muon production is dominant at depth in the subsurface as muons can penetrate greater mass depth before stopping.

Most of the muon production in cosmogenic nuclides is due to either negative muon capture or fast muon reactions (Heisinger et al., 1997). As a negative muon is slowed, it can be captured into an electron orbit, and subsequently collapse into the nucleus where it can react with protons and results in the loss of excess energy, nucleons, and in some cases an α-particle (Table 6.1). Cosmogenic nuclide production due to fast muons involve various reactions and are generally treated as one continuum rather than independent processes (Heisinger et al., 2002b). The muon reactions that result in the production of the cosmogenic nuclide ^{10}Be, ^{21}Ne and ^{26}Al are defined in Table 6.1.

In contrast to ^{10}Be and ^{26}Al, ^{21}Ne is also produced by nucleogenic pathway by capture of α-particles derived from decay of naturally occurring uranium (U) and thorium (Th) by the reaction ${}^{18}_{8}O(\alpha, n){}^{21}_{10}Ne$ (Niedermann et al., 1993). The production of nucleogenic ^{21}Ne presents an obstacle for accurately determining the amount of cosmogenic ^{21}Ne. However, nucleogenic and cosmogenic ^{21}Ne can be distinguished (Balco et al., 2019), which is implemented later in sect. 7.2.2.2

6.3 Production Rates of Cosmogenic Nuclides

Many target elements produce cosmogenic nuclides, including but not limited to O, Mg, Al, Si, Mn, and Fe (Gosse and Phillips, 2001). Therefore, the production rate of the cosmogenic

nuclide concentrations depends on the target rocks or mineral matter. However, many cosmogenic nuclides are produced by the target elements silicon (Si) and oxygen (O), the two components that make up quartz, therefore making quartz a favorable target for cosmogenic nuclide measurements as it effectively excludes other target elements (Lal and Arnold, 1985; Nishiizumi et al., 1986). Further, quartz is one of the most abundant minerals occurring on Earth and its resistance to physical and chemical weathering makes it abundant in most sedimentary deposits. In addition, the tight crystal structure limits the diffusion loss of ^{21}Ne over geological time and is likely to reveal more reliable measurements (Graf et al., 1991)

The production rate of a given cosmogenic nuclide is not the same everywhere on Earth's surface and is dependent on the cosmic-rays flux influenced by Earth's magnetic field and atmospheric mass (Lal, 1991). Primary cosmic rays are positively charged and therefore accelerated or decelerated by Earth's electrical field, and deflected by the magnetic field. Due to the shape of Earth's magnetic field, the cosmic-ray flux increases with magnetic latitude and is higher at the poles than in equatorial regions (Dunai, 2010). Further, as the cosmic-ray flux attenuates with atmospheric depth, the variability of the cosmic-rays at Earth's surface depends on both latitude and altitude. The production rate for a specific sampling site can then be found from the product of a reference production rate and a scaling factor that accounts for this variation.

The reference production rate is calibrated from a data set of known exposure ages and averaged to yield a best estimate of a true value of 4.00 atoms g^{-1} yr^{-1} for spallation (Balco, 2008). The calibration data set from which the reference production rate is derived includes a more comprehensive data set of ^{10}Be compared to ^{26}Al and ^{21}Ne (Balco et al., 2008). Therefore, to

decrease the uncertainties, the production rate for ^{26}Al and ^{21}Ne is derived from a production rate ratio. The $^{26}Al/^{10}Be$ production ratio in quartz is 6.75, whereas the $^{21}Ne/^{10}Be$ production ratio is 4.03.

Two main methods are currently used to obtain a scaling factor for the production rate. One, is a simple scaling method known as 'St', which requires the latitude and altitude parameter for a specific sampling site (Lal, 1991). The 'St' scaling method was later updated to account for the atmospheric pressure rather than altitude by Stone (2000). This is important since the atmospheric pressure above Antarctica is 20-40 mbar lower than standard atmospheric values. This pressure anomaly is caused by the airflow across the ice sheet. Not accounting for this can cause a systematic error of 20-30% as the production rate is much higher in Antarctica compared to similar altitudes in the norther hemisphere (Stone, 2000).

The other scaling method, known as 'LSD' by Lifton et al. (2014) quantifies the temporal variability in the geomagnetic field and as a result yields a long-term (> 1 Ma) average production rate. In polar regions this scaling method predicts a larger altitude dependence compared to the 'St' method. In Antarctica the 'LSD' scaling method has been suggested to perform better in high altitudes compared to the widely used 'St' scaling method which was found to overestimate exposure ages at high altitudes in polar regions (Balco, 2016).

6.4 Surface Exposure Dating

A surface sample exposed to cosmic-rays can be dated by the measured accumulation of cosmogenic nuclides. Exposure dating of glacial events relies largely on subglacially derived debris and boulders transported to the ice margins and deposited as moraines or exposed by glacial retreat as a drift. The basic assumptions for such exposure dating are that a sample (i) has never been exposed to cosmic-rays prior to entrainment; (ii) has only been exposed to cosmic-rays since deposition; and (iii) has then never been covered, displaced, nor disturbed while exposed at the surface. If these assumptions of exposure dating are met, then measured cosmogenic nuclide concentration in debris and boulders is directly related to the exposure time of such samples (Lal, 1991; Niedermann, 2002) and, subsequently the age of glacial events. The accumulation of cosmogenic nuclide concentration N(atoms g^{-1}) for a radionuclide i during exposure time t (yr) can be expressed by Eq. (1). Eq. (2) describes the accumulation of stable nuclides.

$$N_i(t) = \frac{P_i(0)}{\lambda_i}\left(1 - e^{-\lambda_i t}\right) \quad (1)$$

$$N_{21}(t) = P_{21}(0)t \quad (2)$$

Where λ is the decay constant (yr $^{-1}$), and $P(0)$ is the scaled surface production rate (atoms g^{-1} yr^{-1}) for nuclide *i*. The exposure time *t* in Eq. (1) and Eq. (2) is considered the "apparent" exposure age if the geological history such as surface erosion, prior exposure (inherited) and

incomplete exposure due to shielding is unknown. However, many of these processes can be resolved by measuring two cosmogenic nuclides having different half-lives (Lal, 1991).

6.5 Concepts Determining Age and Erosion Rates

A sample that experiences surface erosion will have a lower measured nuclide concentration, as material of low nuclide concentrations from below will approach the surface at a rate of erosion. The exposure age determined in Eq. (1) and Eq. (2) will therefore only provide a minimum age. On average, global erosion rates are found to be approximately 12 m Myr^{-1} for bedrock and 218 m Myr^{-1} for drainage basins (Portenga and Bierman, 2011). However, spatially, these rates range from some of the lowest erosion rates of < 0.1 m Myr^{-1} reported in older exposed surface boulders in the absolute desert of Atacama (Placzek et al., 2014) to highest erosion rates of 2500 m Myr^{-1} for catchment basins in Himalaya (Lavé and Avouac, 2001). While the cold, arid environment of Antarctica provides limited surface erosion, low erosion rates of 0.2 – 5 m Myr^{-1} as reported for various lithologies throughout the continent can increase the exposure age (Marrero et al., 2018). The accumulation of cosmogenic nuclides of an eroding surface can be expressed as

$$N_i(t) = \frac{P_i(0)}{\lambda_i + \frac{\rho\varepsilon}{\Lambda}}\left(1 - e^{-\left(\lambda_i + \frac{\rho\varepsilon}{\Lambda}\right)t}\right) \quad (3)$$

Where ε is the erosion rate (cm yr^{-1}), ρ is the density (g cm^{-3}) of the eroding material, and Λ is the attenuation length (g cm^{-2}) of the cosmic rays. For a stable nuclide the decay constant in Eq. (3) becomes zero. The concentration of each nuclide is a function of exposure age and surface

erosion rates. Therefore, measurements of two nuclides yield two independent equations in which both unknowns can be solved for in certain circumstances.

The initial ratio between two nuclides is that of their production ratio. With increasing exposure time this ratio decreases at a known trajectory determined by the decay rates of the radionuclides and is shown in Fig. 6.1 as ‘simple exposure’. Any effect of surface erosion or burial leads to a further decrease in the nuclide ratio with time and can be solved for as described in Lal (1991). When plotting the relationship between the ratio of two nuclides and the concentration of the longest lived nuclide of the two (commonly used burial plot), a surface sample that has not experienced any burial but may have been subjected to erosion will plot within a zone of steady-state-erosion (Lal, 1991). In Fig. 6.1 this steady state-erosion zone is found between ‘simple exposure’ and ‘steady erosion’ line. In situations where the exposure history does not satisfy all the assumptions associated with a surface exposure with erosion, and where a sample has experienced variation in cosmogenic nuclide production, and/or episodic burial, etc. a sample will plot outside this zone.

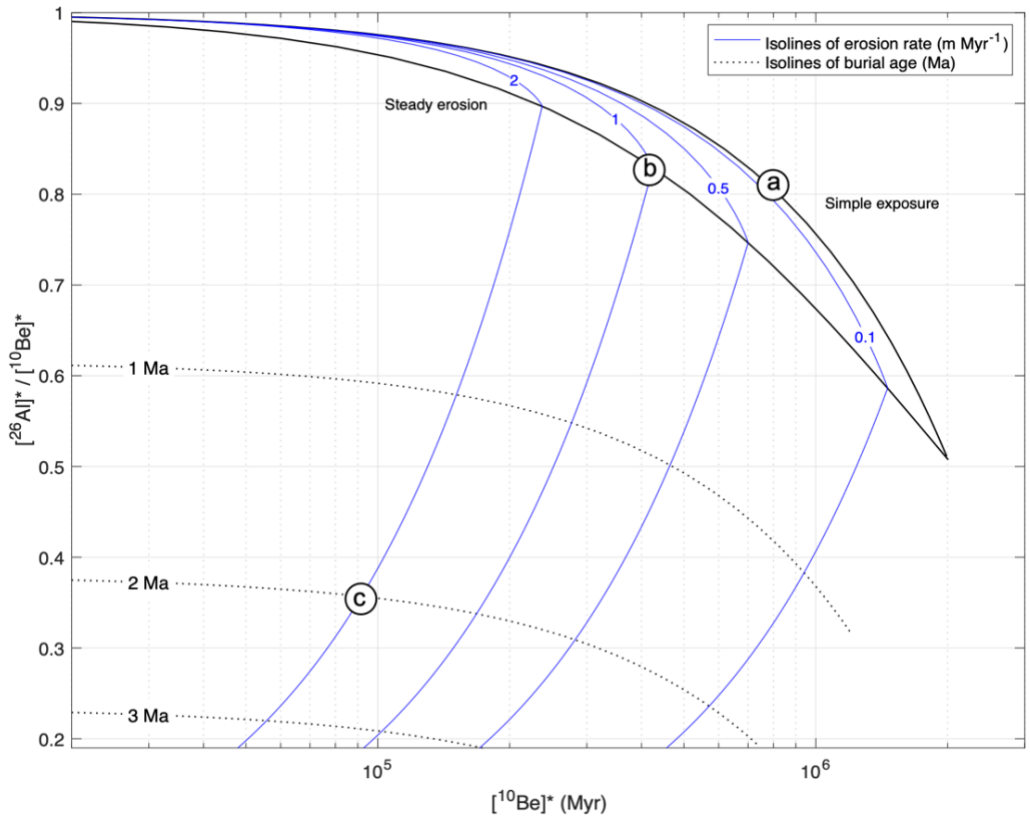

Figure 6.1 Paired ^{26}Al-^{10}Be nuclide diagram. Solid black lines show the 'simple exposure' and 'steady erosion' which confines the steady-state erosion zone. Dashed black lines show the burial lines as Million-year decay isochrons. *Nuclide concentrations normalized to respective surface production rate. A sample exposed at the surface for a duration of e.g., 1 Ma having experienced no surface erosion (Eq. 1) will have a paired nuclide concentration as that of (a). A surface sample that has been subjected to a steady erosion will take the path of the blue isoline within the steady-state erosion zone (Eq. 3). If this sample has been exposed at the surface for an extended period of time and has reached saturation with a steady erosion rate of e.g., 1 m Myr^{-1}, it will have a paired nuclide concentration as that of (b). If a sample exposed at the surface is subsequently buried to a depth of where production diminish, decay of the radionuclide will result in a paired nuclide concentration as that of (c) after e.g, ~2 Ma, following Eq. (4)-(6) depending on the exposure history prior to burial.

6.6 Burial Dating

The principle of burial dating is that different cosmogenic nuclides, such as ^{10}Be and ^{26}Al, in the same mineral are produced at a fixed ratio that depends on the production rates. Samples that have experienced a single period of exposure at the surface have nuclide concentration ratios corresponding to the production ratio and decay of each nuclide (Fig. 6.1). If the two nuclides have

different half-lives, burial of the sample to a depth at which the cosmic ray flux is diminished causes the observed ratio to change through time due to the different rates of radioactive decay (Lal, 1991). Thus, given several other assumptions, the ratio reflects the duration of burial. If any burial has occurred, a sample exposed at the surface will then plot in a burial zone below the steady-state-erosion zone (Fig. 6.1).

If a sample has experienced a two-stage exposure history. That is, it has been exposed at the surface for an extended period time and experienced erosion, and then subsequently buried. Then the total concentration of cosmogenic nuclide i is,

$$N_i = \frac{P_i(0)}{\lambda_i + \frac{\rho\varepsilon}{\Lambda}}\left(1 - e^{-\left(\lambda_i + \frac{\rho\varepsilon}{\Lambda}\right)t}\right)\left(e^{(-\lambda_i t_b)}\right) + \frac{P_i(z_b)}{\lambda_i}\left(1 - e^{-(\lambda_i)t_b}\right) \quad (4)$$

Where, t_b is the duration (yr) of burial, b. To simplify the text and mathematic in this paper, the depth, z is described in units of g cm^{-2} to reflect the attenuation length of the cosmic-ray flux according to the mass traversed. This measure of depth is often referred to as 'mass depth' or 'shielding depth', and defined as the depth, d (cm) below the surface and the density, ρ of the overlying material, such that $z = d\rho$.

In Eq. (4) the first term represents the exposure of an eroding sample (as seen in Eq. (3)), with a radioactive decay factor applied to correct for the burial. The second term is the nuclide concentration accumulated post-burial, that is, the amount of nuclides produced between the time of burial and the present. This second term becomes insignificantly small if a sample is buried at

sufficient depth to which it is shielded from cosmic-rays (Balco and Rovey, 2008). With a half-life of 1.39 and 0.71 for ^{10}Be and ^{26}Al respectively, the ^{26}Al-^{10}Be ratio can provide a useful burial dating time range of approximately 0.2-4 Ma (Balco and Rovey, 2008), and is extended for a nuclide pair including ^{21}Ne.

For a sample exposed for long enough time at the surface such that it reached steady-state erosion prior to burial and then buried deeply enough, then Eq. (4) can be simplified to

$$N_i = \frac{P_i(0)}{\lambda + \frac{\rho\varepsilon}{\Lambda}}\left(e^{(-\lambda_i t_b)}\right) \tag{5}$$

Measurement of two nuclides having different production and decay rates yield two independent equations from which both the burial age and erosion rate can be estimated.

On the contrary, if no surface erosion occurred prior to burial of the sample, then the following simplified equation can be used to solve for the burial age and pre-burial exposure time,

$$N_i = \frac{P_i(0)}{\lambda}\left(1 - e^{-\lambda t}\right)\left(e^{(-\lambda_i t_b)}\right) \tag{6}$$

In many cases, erosion cannot be neglected. Therefore, if assuming that some unknown amount of erosion has occurred then when solving for the pre-burial exposure time t in Eq. (6) can only provide a minimum exposure.

6.7 Cosmogenic Nuclide Depth-Profile Dating

Because the cosmic-ray flux is rapidly attenuated with depth below the surface, the concentration of cosmogenic nuclides at depth below the surface can be used to exposure date or quantify geologic processes of, e.g., debris deposit (Lal, 1991; Nishiizumi et al., 1993). Such dating method is generally referred to as "depth-profile dating" (Hidy et al., 2010). Analysis of a single nuclide depth profile, in which equilibrium is not yet reach, can provide a unique solution of exposure age, erosion rate and inheritance in various geomorphic settings (Anderson et al., 1996; Braucher et al., 2009).

Debris in glacial deposits, as well as other deposits, may have had significant pre-exposure prior to transportation and deposition in which the grains and/or clasts may contain a mixture of various exposure history. By sampling bulk sediment, at various depths an average inheritance for the deposited debris can be estimated (Anderson et al., 1996), and results in the addition of the inherited nuclide concentration variable N_{inh} (atoms g^{-1}),

$$N_i(z,t) = N_{i,inh}e^{(-\lambda_i t)} + \frac{P_i(z)}{\lambda_i + \frac{\rho\varepsilon}{\Lambda}}\left(1 - e^{-\left(\lambda_i + \frac{\rho\varepsilon}{\Lambda}\right)t}\right) \quad (7)$$

Where z is mass depth (g cm^{-2}) below the surface. As previously mentioned, the attenuation length for spallation, sp is shorter than that of muons, μ. The attenuation rate for negative muon has been well characterized as a function of depth and can be expressed as a single function

(Heisinger et al., 2002a; Heisinger et al., 2002b). Therefore, the total production, P of cosmogenic nuclide i is then,

$$P_i(z) = P_{\mu,i}(z) + P_{sp,i}(0)\, e^{\left(\frac{-z}{\Lambda}\right)} \quad (8)$$

By knowing the total production rate at depth, then the depositional age, erosion rate and inherited nuclide inventory can be modeled and quantified by a geologically constrained Monte Carlo simulation (Braucher et al., 2009; Hidy et al., 2010).

Various cosmogenic nuclide depth profiles have been applied to quantify depositional ages and erosion rates of moraines (Schaller et al., 2009) and alluvial terraces (Granger and Smith, 2000; Phillips et al., 1998; Siame et al., 2004; Wolkowinsky and Granger, 2004). In many such cases it is important to account for mixing of the cosmogenic nuclide inventory in the surface layer, known as the bioturbation zone (Lal and Chen, 2005; Perg et al., 2002). Any partial or full vertical mixing can influence the age and/or the erosion rate of deposit.

In Antarctica, multiple depth profile studies have shown that cosmogenic-nuclide concentrations in samples within supraglacial debris overlying buried ice can also be used to establish limits on the rate of sublimation of the ice (Bibby et al., 2016; Marchant et al., 2002; Ng et al., 2005; Schäfer et al., 2000) as well as samples from the debris within the ice (Stone et al., 2000). Further, Morgan et al. (2010a, 2010b) showed that samples collected from debris in the McMurdo Dry Valleys indicate that sublimation has occurred although the ice no longer is preserved under this debris. Additionally, the concentration of ^{10}Be and ^{26}Al at depth below the

surface of such debris is a result of both the sublimation rate of the ice and the erosion of the overlying debris. However, they were only able to constrain the rates of sublimation and erosion, and not the emplacement age of the no-longer present ice.

6.8 Limitations to Maximum Measured Time Period

Although both time and erosion rates are presented as variable, e.g., Eq. (1) and (3), it is not always possible to uniquely solve for both age and erosion rates. A common problem in cosmogenic nuclide analysis is that the cosmogenic nuclide concentrations reach equilibrium between the production and decay rates. With the presence of erosion, this equilibrium will be reached more rapidly (Gillespie and Bierman, 1995). The time it takes for cosmogenic nuclide concentration to reach equilibrium with acting erosion rates is controlled by an effective half-life,

$$\tau_{i,1/2,e} = \frac{\ln(2)}{\left(\lambda_i + \frac{\rho\varepsilon}{\Lambda}\right)} \tag{9}$$

An equilibrium of the cosmogenic nuclide concentrations can be reach after 3-4 effective half-lives have passed (Ivy-ochs and Kober, 2008). Thereafter, it is only possible to confidently state the erosion rates and not the exposure age of the deposit. With an erosion rate of 0.8 m Myr^{-1}as recorded for the supraglacial debris in Ong Valley (Bibby et al., 2016), an equilibrium is reached after approximately 3.7 Myrs and 2.7 Myrs for the radionuclide ^{10}Be and ^{26}Al, respectively (Fig. 6.2). Although ^{21}Ne is a stable isotope, it will still be affected by erosion and will also reach equilibrium with a degradation rate.

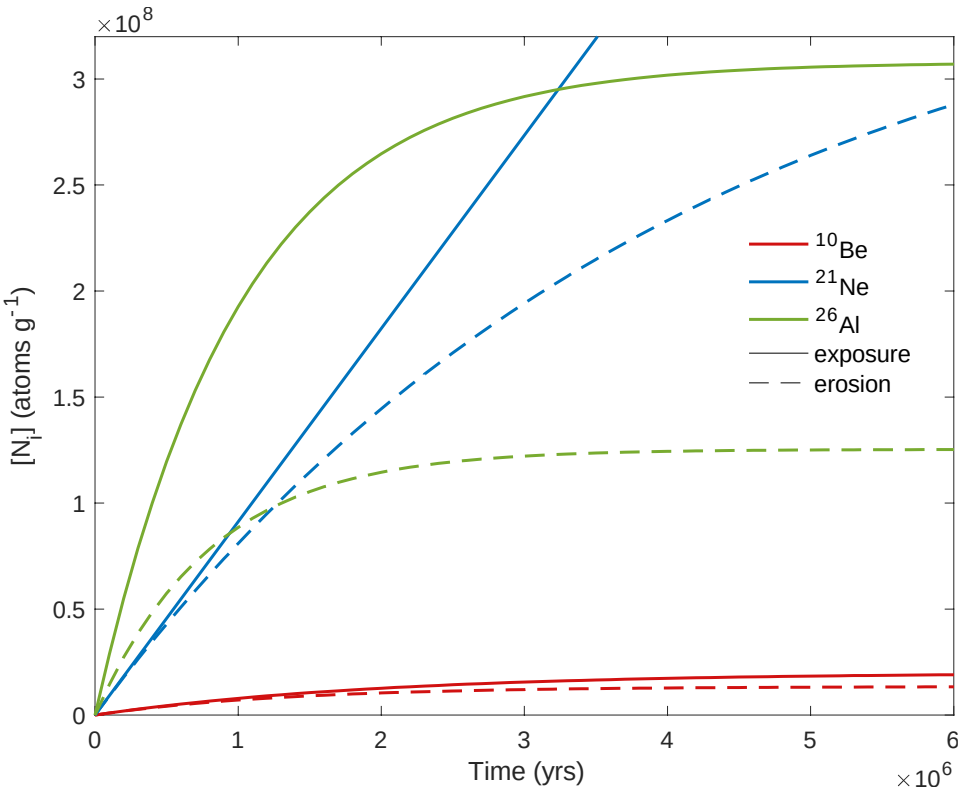

Figure 6.2 Accumulation of cosmogenic nuclides ^{10}Be, ^{21}Ne, and ^{26}Al with time for simple surface exposure (solid line) and with an effective surface erosion of 0.8 m Myr^{-1} (dashed line). An equilibrium between the production and decay rates is reached after a few half-lives.

6.9 Cosmogenic Nuclides Methods Utilized for Dating Ong Valley Buried Ice

In Ong Valley, there are three means by which we can apply cosmogenic-nuclide data to determine the age of the buried ice mass. First, we can apply exposure-dating to the supraglacial debris; this approach was taken by Bibby et al. (2016). However, because the supraglacial debris is formed by sublimation after the deposition of glacial ice, the duration of the surficial exposure of the supraglacial debris is, by definition, less than the age of the ice. Thus, in this case, a surficial exposure-dating is expected to yield only a minimum age. We can exposure date the supraglacial debris by determining the apparent exposure age of the surface defined as the exposure age calculated from a nuclide concentration with the assumption of a single period of exposure

continuing until today without erosion or burial. Further, we can use two nuclides to quantify both erosion and exposure time (Lal, 1991).

The second approach that we use to determine the age of the buried ice mass is the depth-profile dating method and involves measurements of both surface and subsurface nuclide concentrations. This approach relies on the observation that surface concentrations show a greater dependence on sublimation and/or surface erosion rates and lesser dependence on emplacement age compared to concentrations in the subsurface below several meters depth (Braucher et al., 2009; Stone et al., 1998). Thus, paired subsurface and surface measurements can, in principle, yield a unique solution for both ice age and erosion rate. In Ong Valley, we apply this approach to both the supraglacial debris and subsurface englacial debris in the core by creating a forward model that predicts nuclide concentrations at all depths as a function of the age of a deposit, the surface erosion rate of the deposit, and, in this case, the ice sublimation rate leading to formation of the supraglacial debris deposit. Fitting this forward model to a data set then yields best-fitting estimates of these input parameters.

The third approach can be used if any of the englacial debris has formerly been exposed at the Earth's surface and subsequently buried. Then we can apply a burial dating method based on the decay of cosmogenic radionuclides produced during the initial period of exposure. Although we had no prior reason to expect the englacial debris to be sourced from recycled surface debris, we show later that it is, in fact, the case in Ong Valley. Therefore, at our field site, burial dating can be used as an approach to constrain the age of the ice.

CHAPTER 7
METHODS

To determine the age of the buried ice mass in Ong Valley and understand it's overall geologic history we apply methods of both cosmogenic nuclide exposure dating and high-precision positioning. In the following subsections, we explain the use of high-precision positioning to map the glacial moraines and drift boundaries, and to detect surface movement in order to evaluate the stability of this buried ice mass and associated drift system. Later, we apply cosmogenic nuclide dating to determine the age of the buried ice mass and present a novel dating application of cosmogenic nuclides which aims to quantify a complex exposure history of this buried ice mass.

7.1 Differential High-Precision Positioning

Ong valley contains three glacial drifts separated by lateral and end moraines. To utilize these drifts for paleoclimatological and geomorphological analyses, it is important to determine their stability. The long-term stability of such drifts has been studied elsewhere in Antarctica (Putkonen et al., 2008). However, no comparable studies have been done in the central TAM. Therefore, to evaluate the stability of the drift system in Ong Valley we use high-precision positioning to map the glacial moraines and drift boundaries, and the current boundary of the buried ice. Further, we measure the high precision positions of eight surface boulders located on

the drifts over seven years to determine the mobility and stability of these drifts and buried ice masses.

Differential high-precision positioning allows for the determination of an accurate location of an object by making use of a reference point to correct for transient errors and attains a precision level of centimeter to millimeter scale. High-precision positioning utilizes the Global Navigation Satellite System (GNSS), a constellation of satellites used to determine a receiver's location. Various nations have deployed multiple navigation systems, including the most commonly used Global Positioning System (GPS) in the United States, Global Navigation Satellite Systems (GLONSS), Galileo, BeiDou, etc. These satellite navigation systems broadcast signals that the receivers use for calculating the position. The time it takes for the signal from individual satellites to travel to the receiver is used to calculate the unique location of the receiver. Once the receiver collects data from at least four satellites, it can provide a location estimate. Today, a common handheld device using GPS can achieve a meter scale accuracy at a 95% confidence level. Such accuracy is adequate for the everyday navigation purposes of a hiker or a driver of a vehicle. However, for our research purposes, where centimeter accuracy is required, high-precision positioning is necessary. In Ong Valley, we use a combination of the various GNSS and differential correction schemes between two GNSS receivers to acquire a high accuracy position for moraine mapping and for detection of boulder movement.

Various high-precision positioning schemes can be utilized, two of which are kinematic and static surveying. To understand the stability of the drift systems in Ong Valley, we take advantage of both. Kinematic GNSS is a fast-surveying method in which measuring periods are of

short duration and typically under two minutes. However, such relatively quick surveying decreases the accuracy but makes it practical for the rapid mapping of large numbers of objects or points. Therefore, kinematic GNSS surveys are often used where lower accuracy standards are adequate. Kinematic GNSS is ideal for mapping of moraines and drift boundaries. In instances where higher accuracy is desired, static or fast-static is preferred. However, static surveying requires much longer survey sessions, typically more than 20 min in which the antenna remains fixed during the period of observation. Static surveying was used for boulder positioning to increase the potential of detecting even small surface movements of the drift systems.

7.1.1 Moraine Mapping

Mapping the distribution of glacial features and deposits can aid in understanding the behavior of past glacial advancements, such as the extent and dimensions, locally and potentially continental-wide. In this subsection, we explain the procedures for mapping the lateral and end moraines observed in Ong Valley and the current location of the drift boundaries and buried ice masses.

In addition, by obtaining constraints on the emplacement age of the middle ice and sublimation rate through cosmogenic nuclide exposure dating, we can predict a total amount of sublimation and, hence, surface lowering over the lifespan of the ice mass. This, in turn, can be compared with the elevation differences between the current drift surface and lateral moraines. The highest moraines correspond to the maximum extent and elevation of those glaciers when they

advanced into the valley. This will provide an independent verification of our modeling and help to validate our results.

7.1.1.1 Data Collection

During the 2017/2018 Antarctic field season, GNSS coordinates were collected along the crests of multiple glacial moraines throughout Ong Valley (Fig. 7.1). Each moraine was measured using stop-and-go kinematic surveying. A stop-and-go surveying requires an initialization of the receiver for approximately 20 min prior to data collection but then allows the ability to go from one point to the next while collecting only a few seconds of data at each individual point location along the traverse. The moraines were mapped by following the crest or perimeter and measuring the positions for approximately 15 sec, every 5-15 meter. The moraine positions were collected using a Trimble R7 receiver, with a Zephyr Geodetic antenna mounted to a 2 m survey pole with an attached leveler. The continuous base station data were collected by a Trimble R9 receiver and Zephyr Geodetic 2 RoHS antenna with a 0.07655 m high leveler base mounted to a permanent anchor-bolt drilled into bedrock.

Six visible moraines were not accessible for direct GNSS measurements because of their location up on steep valley walls. Instead, the positions of these moraines were determined by measuring their position with a laser ranger and a reference location on the valley floor that was mapped by GPS. A reference point perpendicular to each moraine crest (valley-wall) and 100-500 m away towards mid-valley was located and recorded using Garmin GPSMAP 76 GPS. From the reference point, the elevation difference to the moraine was then measured using a Nikon Forestry

Pro Laser Range finder aimed perpendicular to the moraine. The locations and elevation differences were recorded and later used for mapping.

Figure 7.1 Photograph of the western valley wall adjacent to the old drift in Ong Valley, Antarctica. White dashed line indicates some of the moraines traversed.

7.1.1.2 Differential GNSS Processing of traverse

All GNSS data collected during moraine traverse were processed using Trimble Business Center (TBC) v5.20 software package provided by UNAVCO. The 2017/2018 Ong Valley base station was set to record daily and hourly (1Hz1Hr) positioning. With stop-and-go surveying being less accurate than static GNSS surveying, the collected moraine data were processed against 1Hz1Hr hourly base data, with a horizontal and vertical precision failure set at 0.50 m. The baseline processing steps are outlined in Appendix A. After completing baseline processing, data were exported as a geodatabase file for data analysis in ArcGIS and outlined in Appendix B.

7.1.1.3 Moraine Position Analysis

The moraine data point handling and analysis was preformed using ArcGIS Desktop 10.7.1. To analyze the moraine data, a 1-m resolution, time-stamped Digital Surface Model (DSM) of Ong Valley was obtained from the Polar Geospatial Center's (PGC) Reference Elevation Model of Antarctica (REMA) (Howat et al., 2019). Further, an 8-band multispectral, high resolution (1.9 m) WorldView2 satellite imagery were obtained for Ong Valley. The satellite image was overlaid and visually georeferenced to the DSM hillshade raster imagery using WGS84 Antarctic Polar Stereographic spatial coordinate system. This results in a 2-meter resolution satellite image of Ong Valley overlaying a 1-meter resolution elevation data used for analyzing the moraine data points. The laser measured moraines were manually added to the moraine point data, based on field measurements, satellite imagery, and raster elevation values.

To correlate glacial features across the valley walls in Ong Valley, an elongated two-dimensional profile of Ong Valley was created. First, a smooth curved profile line was drawn along the center of the valley, using the DSM raster for elevation values. Then all moraine data points where projected, in planar view, onto the profile line based on nearest analysis. Using MatLab_R2020a software, the resulting profile of Ong Valley was plotted with the projected moraine points. When visually analyzing the profile, one must consider that the projected moraine data point's location on the line does not represent a true relation to its surrounding data points in the figure because of projection onto a curved line, but rather an approximate relation.

7.1.2 Boulder Positioning and Movement

To evaluate the stability for each of the three drifts and determine if any movement has occurred in Ong Valley, we repeatedly measured the position of eight boulders from the three drifts. The positions of the surface boulders were originally measured during the Austral summer 2010, and again in 2011 and 2017. The general assumption is that the drift system is currently experiencing no or limited movement, and we therefore utilized high-precision positioning for this analysis.

7.1.2.1 Data Collection

During the Austral summer, 2010/2011, bolts were installed in eight boulders (prefix: OV-GPS-*) found on the surface of the three Ong Valley drifts (Fig. 7.2 and Fig. 7.3). These bolts are ~30 cm long and were manually drilled and mounted as close to vertical orientation as possible, into the upper surface of the boulders. The actual measurement point is a small (~2 mm diameter) dimple stamped on the middle of the flat, top surface of the rock bolt. To perform the final leveling of the GNSS antenna, a leveling mount of known shaft dimension was screwed on the rock bolt. The leveling mount consists of an adjustable system of plates and screws to allow for leveling the top surface of the mount with the aid of a carpenter level. Once the mount was leveled the antenna was attached to the mount for determining the exact position of the stamped dimple.

Two boulders were chosen from the youngest drift, three from the middle drift, two from the oldest drift, and one near the boundary between the middle- and old drift. The boulders were

originally selected based on their evidence for stability in the drift. Each boulder was >1.5 m in longest dimension and partially submerged in the supraglacial debris, such that any movement is assumed to be caused by either from ice movement or active polygons. However, no ideal boulder was available at the boundary between the middle and old drift, and therefore the boulder OV-GPS-08 was chosen although it is entirely perched above the drift. A GNSS base station bolt was established in Ong Valley on an elevated bedrock outcrop central to the valley and less than 2 km from any of the eight boulders. The base station antenna was installed at the beginning of each field expedition in Ong Valley and disassembled at the end of each expedition.

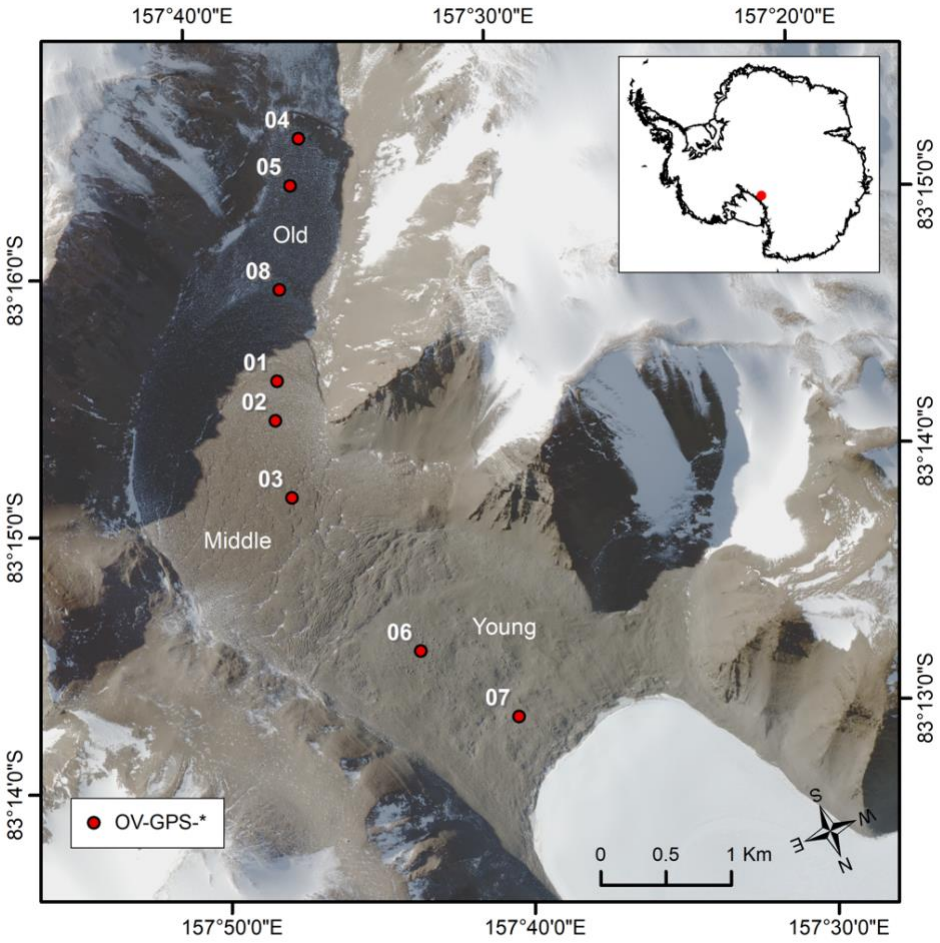

Figure 7.2 Boulder locations for high-precision GNSS measurements in Ong Valley, Antarctica (WV2 satellite image © 2016 Maxar). Red dots indicate the locations of the boulders. The legend shows the prefix for the boulder names.

Figure 7.3 Photographs of surface boulders used for GNSS high-precision movement analysis. (a) OV-GPS-01, (b) OV-GPS-02, (c) OV-GPS-03, (d) OV-GPS-04, (e) OV-GPS-05, and (f) OV-GPS-06, (g) OV-GPS-07, and (h) OV-GPS-08.

The installed bolts in each boulder were revisited twice over the years. On these re-occupations we followed the original antenna mounting procedure and determined the exact locations of the 2 mm diameter dimples at the top end of the stationary rock bolts.

If no boulder movement has occurred between each measurement, the antenna is assumed to be in the exact location for every measurement. We were able to attach the antenna to a horizonal accuracy of <1°, resulting in a centered offset of <0.2 cm of the antenna between the years of repeating measurement. The position of each boulder was measured during the Austral summer 2010, 2011, and 2017 by collecting GNSS data using receivers and antenna provided by UNAVCO (Table 7.1). With the base station <2 km away, each boulder location was recorded for a duration of 18-60 min for optimal accuracy.

Table 7.1 Receiver and Antenna used for measuring boulder.

	2010	2011	2017
Base station			
Receiver	Trimble R7	Trimble R7	Trimble R9
Antenna	Trimble zephyr geodetic	Trimble zephyr geodetic	Trimble zephyr geodetic 2 RoHS
Leveler height from bottom of antenna mount (m)	0.078	0.078	0.07655
Rover			
Receiver	Trimble 5700	Trimble R7	Trimble R7
Antenna	Trimble zephyr geodetic	Trimble zephyr geodetic	Trimble zephyr geodetic
Leveler height from bottom of antenna mount (m)	0.077	0.075	0.07840

7.1.2.2 Postprocessing of High-Precision Boulder Positions

Many factors contribute to the degradation of the GNSS signal and systematic biases, therefore affecting the accuracy. These factors include the atmospheric (ionosphere and troposphere) signal delay, uncertainty in a satellite's orbit and atomic clock, the number of satellites visible by the receiver, clock and software delays in the receiver, and path error at the site of the receiver. To significantly reduce these systematic biases and increase the accuracy for each boulder position, we perform a baseline process using differential GNSS correction.

A differential GNSS correction uses two receivers in close proximity to each other, typically <5 km, in which they are expected to experience similar atmospheric and satellite signal conditions. One receiver, the base station, is at a fixed, known point and collects continuous position measurements. The other receiver is, in this case, the rover used to measure the positions of the boulders. The base station and rover collect data simultaneously during the active measurement period. A baseline (distance) is developed between the two receivers when processing the data. Both receivers are in fixed locations, however the base station has been recording its location continuously for a month, resulting in high accuracy of its estimated position which is used as a quality control point for the base station each year. Any distortion in the signal can be calculated and corrected during post-processing of the boulder GNSS data.

The measured data from each boulder, when processed, results in a unique point for every boulder. The true position of any of the boulders at any time is unknown. However, baseline processing provides an estimated position within a confidence interval. Therefore, all points

undergo a baseline processing using the base station data as the reference point to obtain a high-precision position. That is, an estimated position with high confidence. The baseline processing results in a point defined by a Northing, Easting, and elevation value, with a vertical and horizontal precision derived from all data points collected during the measurement period. The procedure for the baseline processing is outlined in Appendix A.

All GPS data were processed using Trimble Business Center (TBC) v5.20 software package provided by University Navstar Consortium (UNAVCO). During field season 2010 and 2011, only daily data files were available (as opposed to hourly), and therefore only daily data files from the base station were used for all baseline processing. All daily base station files (Austral summer 2010, 2011, and 2017) were merged and corrected to a control quality point in TBC, creating a reference point for the baseline processing. The boulder GPS points were processed by first importing the raw .T0 GNSS files into TBC. A rinex file (.obs and .nav) was used only for point OV-GPS-02-2017, as the raw .T01 GNSS boulder measurement file straddled the base station files, causing issues during the baseline process. Further, no base data is available for point OV-GPS-08-2010 and therefore is not included in the processing.

With the location of the base station being near a vertical cliff, parts of the receiver's sky view is blocked and degrades the receiver signal. Other temporary and/or permanent base stations have been installed throughout the continent in Antarctica. These base stations are positioned at high elevation ridges with unlimited view of the sky. The nearest of these base stations is the IGGY station, which is installed at the Iggy Ridge in Miller Range, Antarctica, approximately 20 km from Ong Valley. Therefore, in an attempt to increase the accuracy, the boulder data were

processed against the IGGY base station. Data from the IGGY base station was available from 2011, which was processed and compared with that of the Ong valley base station. The processed boulder data from IGGY did not increase the precision. Therefore, the post processing of the GNSS data was limited to only to the data obtained in Ong Valley.

7.1.2.3 Boulder Movement Analysis

The movement of a boulder is determined from its change in position between the repeated measurements from 2010 to 2017. That is, we can calculate the distance between the measured location for a boulder between the years 2010-2011, 2011-2017, and 2010-2017. If the distance exceeds that of the uncertainty between two points, then the boulder is assumed to have moved. The position of the point is measured over a processing period in which multiple positions are continuously being recorded. The position after baseline processing is the calculated mean of x (Easting), y (Northing), and z (elevation) position during the measured period. Therefore, the calculated distance a boulder moved is that of the distance between the mean x, y, and z estimated for two separate years. Since the distance between the points is assumed to be <10 cm, the spherical effect of Earth's curvature can be ignored, and the distance *d* (m) is calculated by the Euclidean distance between two points P_1 and P_2, such that

$$d(P_1, P_2) = \sqrt{(x_2 - x_1)^2 + (y_2 - y_1)^2 + (z_2 - z_1)^2} \quad (10)$$

Where x_q, y_q and z_q represent the coordinates for point P_q, identified by q. When determining the horizontal distance only, the z-component of Eq. (10) can be ignored.

When determining the uncertainty associated with the Euclidean distance between two points, it is important to understand the uncertainty of the individual variables. The vertical precision is a one-dimensional component in the z-direction at the 95% confidence interval and is found by scaling the estimated 1-sigma standard deviation of all measured z-values by the coverage factor of 1.960 (Trimble, 2019).

The associated horizontal precision value is a two-dimensional standard error circle at the 95% confidence interval, representing the local accuracy. That is, the uncertainty in the x- and y-direction is combined into one horizontal precision value. All positions recorded during the measured period for the boulder results in a cluster of points that can be defined in a horizontal plane. From this cluster, a standard error ellipse can be defined as the uncertainty in the horizontal plane, where the mean value (x,y) is located at the center of the error ellipse. The dimension of this error ellipse is defined by a semi-major and semi-minor axis, in which the semi-major axis corresponds to the largest error (Fig. 7.4). A standard error circle is then derived from the covariance between the horizontal components using least square adjustment and scaled from the estimated 1-sigma standard deviation by a coverage factor of 2.448 (Trimble, 2019). The horizontal precision is the radius of a 95% confidence circle. A smaller circle represents a higher accuracy, and a more circular error ellipse indicates less variance in the horizontal direction, which results in a more reliable estimated position (Fig. 7.4).

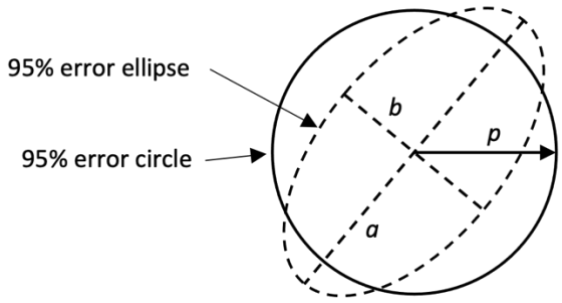

Figure 7.4 The 95% error circle and ellipse, with semi-major (a) and semi-minor (b) axis, and the precision (p).

The uncertainty in the Euclidean distance between two points is that of the combined standard uncertainty u_c (m) and is determined through error propagation using summation in quadrature. Mathematically, the combined uncertainty for a function *f(x,y)* and is the positive square root of the combined covariance $u_c^2(f)$, given by,

$$u_c^2(f) = \left(\frac{\partial f}{\partial x}\right)^2 u^2(x) + \left(\frac{\partial f}{\partial y}\right)^2 u^2(y) + 2r_{x,y}\left(\frac{\partial f}{\partial x}\frac{\delta f}{\delta y}\right)u(x)u(y) \qquad (11)$$

Where *u(a)* is the uncertainty of variable *a* in the function *f(a)*. The last term represents the correlation between the uncertainty of the variables. The correlation coefficient *r* is obtained from the covariance matrix, where $-1 \leq r \geq +1$. If x and y are independent, that is, the variables are uncorrelated, then the correlation coefficient is zero, and the correlation term can be neglected.

The covariance matrix for each position results in a 3x3 matrix providing the variance and covariance of the x, y, and z components. For each point, the uncertainty of the x, y, and z components are correlated, such that if the point changes in one direction, it must also change in the other direction. However, since it is assumed that the position of the boulder has moved with time, P_1 is then independent of P_2, and therefore no correlation exists between the two points. This

results in some variables of the Euclidian distance $d(P_1,P_2)$ being correlated and others uncorrelated. The combined standard uncertainty for the Euclidean distance is expressed as the positive root of the combined covariance $u_c^2(d)$, and defined as,

$$u_c^2(d) = \left(\frac{\partial d}{\partial x_1}\right)^2 u^2(x_1) + \left(\frac{\partial d}{\partial x_2}\right)^2 u^2(x_2) + \left(\frac{\partial d}{\partial y_1}\right)^2 u^2(y_1) + \left(\frac{\partial d}{\partial y_2}\right)^2 u^2(y_2)$$
$$+ \left(\frac{\partial d}{\partial z_1}\right)^2 u^2(z_1) + \left(\frac{\partial d}{\partial z_2}\right)^2 u^2(z_2) + 2r_{x_1,y_1}\left(\frac{\partial d}{\partial x_1}\frac{\partial d}{\partial y_1}\right)u(x_1)u(y_1)$$
$$+ 2r_{x_1,z_1}\left(\frac{\partial d}{\partial x_1}\frac{\partial d}{\partial z_1}\right)u(x_1)u(z_1) + 2r_{y_1,z_1}\left(\frac{\partial d}{\partial y_1}\frac{\partial d}{\partial z_1}\right)u(y_1)u(z_1)$$
$$+ 2r_{x_2,y_2}\left(\frac{\partial d}{\partial x_2}\frac{\partial d}{\partial y_2}\right)u(x_2)u(y_2) + 2r_{x_2,z_2}\left(\frac{\partial d}{\partial x_2}\frac{\partial d}{\partial z_2}\right)u(x_2)u(z_2)$$
$$+ 2r_{y_2,z_2}\left(\frac{\partial d}{\partial y_2}\frac{\partial d}{\partial z_2}\right)u(y_2)u(z_2) \quad (12)$$

Where the partial differential for the x, y and z variable is,

$$\frac{\partial d}{\partial x_l} = \frac{|x_2 - x_1|}{d} \quad (13)$$

$$\frac{\partial d}{\partial y_l} = \frac{|y_2 - y_1|}{d} \quad (14)$$

$$\frac{\partial d}{\partial z_l} = \frac{|z_2 - z_1|}{d} \quad (15)$$

The correlation coefficient $r_{m(q),n(q)}$ for any two-dimension (m,n) in is derived from the covariance matrix for each point, P_q and has the unit of m^2. The correlation coefficient and the covariance matrix are therefore,

$$r_{m,n} = \frac{\sigma_{mn}}{\sigma_m \sigma_n} \tag{16}$$

$$covmat_q = \begin{bmatrix} \sigma_x^2 & \sigma_{yx} & \sigma_{zx} \\ \sigma_{xy} & \sigma_y^2 & \sigma_{zy} \\ \sigma_{xz} & \sigma_{yz} & \sigma_z^2 \end{bmatrix} \tag{17}$$

The error associated with the vertical z-component is in general twice as large as the horizontal error. Therefore, we calculate both a two- and three-dimensional boulder movement. For the two-dimension movement, the z- component for Eq. (10-17) can be ignored.

Boulder movement is considered when the distance between two point is larger than the combined uncertainty, $d > u_c$. If a boulder displays any movement, we can then calculate the azimuth direction that the boulder has moved and the degree from horizontal for the three-dimensional movement. The direction of movement is derived from the cartesian coordinates (r, θ, φ), such that

$$v = \sqrt{\vec{x}^2 + \vec{y}^2 + \vec{z}^2} \tag{18}$$

$$\theta = \cos^{-1}\left(\frac{\vec{z}}{v}\right) \tag{19}$$

$$\varphi = \tan^{-1}\left(\frac{\vec{y}}{\vec{x}}\right) \quad (20)$$

Where v is the length of the vector, and θ is the angle between the positive z-axis and the vector, such that $0 \leq \theta \leq \pi$, and is converted to a degree the boulder moves from a horizontal plane. The calculated φ is the angle between the projection of the vector onto the xy-plane and the positive x-axis such that $-\pi \leq \varphi \leq \pi$ and is converted into an azimuth degree.

7.2 Cosmogenic Nuclide Dating of Middle Ice

In the following subsections we describe the methods for sample collection, measurement of concentrations of the cosmogenic nuclides ^{10}Be, ^{21}Ne, and ^{26}Al, and a numerical forward model which is based on geological and geomorphic observations and used to predict nuclide concentrations that can be compared with our measurements. In a later section we describe how the model is used to interpret the measured nuclide concentrations and how we apply specific approaches of exposure- and burial dating to determine the age of the buried ice mass and gain information on the englacial debris.

7.2.1 Sample Collection

During the Austral summer, 2017/2018, we collected; (i) pit samples from unconsolidated supraglacial debris at drill site 17-OD1, (ii) an ice core taken directly below the pit samples, and (iii) erratic boulders from other locations on the middle drift surface and correlative lateral moraines (Fig. 7.5). The drill site OD1 was located at a central highpoint within the middle drift.

We chose this site because any deformation of the buried ice should be minimized at this location, and colluvium and rockfall from the valley walls cannot reach the site. We determined the location and elevation of the core site using postprocessed differential GPS. Boulder samples were located using uncorrected handheld GPS and their elevations were checked against the Reference Elevation Model of Antarctica (REMA) Digital Elevation Model (DEM) (Howat et al., 2019). Topographic shielding calculations for the sites follow (Balco et al., 2008, with accompanying online material).

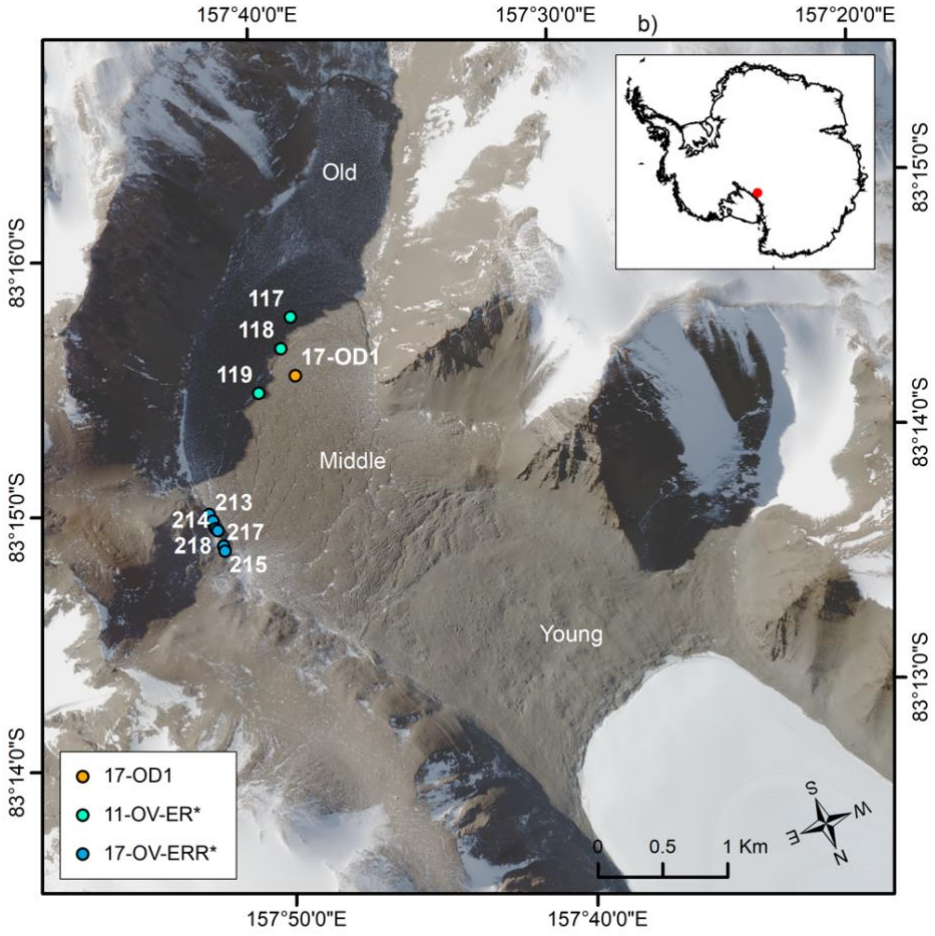

Figure 7.5 Sample sites for cosmogenic nuclides shown on Worldview 2 satellite image of Ong Valley, Antarctica (© 2016 Maxar). The dots indicate sampling sites for pit and ice core (orange), middle drift surface boulders (cyan), and lateral moraine boulders (blue). The legend shows the prefixes of sample names.

7.2.1.1 Vertical Pit Sampling of Surficial Regolith

We excavated a hand dug pit for sampling the vertical section of the supraglacial debris (Fig. 7.6a). The pit was located in the center of a patterned ground polygon formation in which the surface did not show signs of reworking caused by former active polygon boundaries. The supraglacial debris is a sandy diamict with clasts of all sizes up to large boulders. The debris surface is covered by a lag deposit of clasts larger than approximately 5-10 cm. The clasts are mostly angular with occasional faceted and/or weakly polished surfaces. Clast lithologies include both local bedrock and other rock types not locally present. The supraglacial debris shows no sign of stratification nor presence of ice cemented regolith and a sharp boundary can be observed between the debris and the underlying debris-rich ice mass (Fig. 7.6a).

Bulk sediment samples spanning 3-8 cm in sample depth were collected at approximately 10 cm depth intervals (Table 8.2). A total of 6 samples were collected throughout the pit, from the surface to the ice/debris boundary. The depth of the pit is 62 cm reaching from the surface of the supraglacial debris down to the ice surface.

7.2.1.2 Ice Core Sampling

We collected a 944 cm long and 7 cm diameter vertical ice core directly below the deepest supraglacial debris sample. This allows us to construct a depth profile of cosmogenic nuclide concentrations extending from the surface of the supraglacial debris to the bottom of the ice core. An updated Winkie drill (Fig. 7.6b) was used for drilling in mixed-media ice (debris-rich ice)

(Boeckmann et al., 2020). The recovered ice core was divided into segment lengths of 21 cm or less and stored frozen in individual watertight sample containers at the drill site. The samples were kept frozen at <-20°C until processed in the geochemistry laboratory at University of North Dakota.

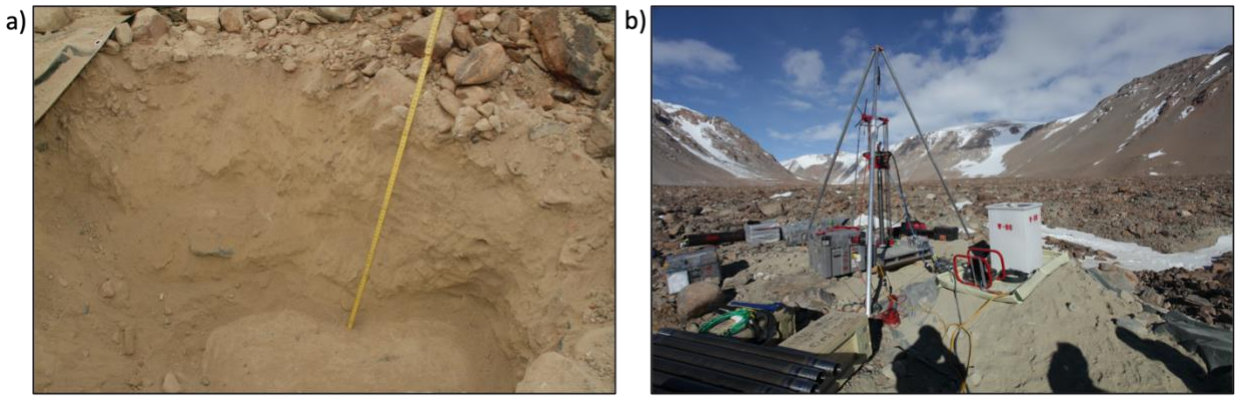

Figure 7.6 Photographs of the drill site 17-OD1. (a) excavated pit for sampling of the supraglacial debris. The middle drift ice surface is found at the bottom of the pit. The yellow ruler in the image measure ~60 cm from the bottom of the pit to the surface of the supraglacial debris. (b) Winkie drill installed above the excavated pit for ice coring. Photograph looking south.

7.2.1.3 Sampling of Middle Drift Boulders

Samples of glacially transported boulders were collected during the 2011/12 field season (middle drift boulders) and the 2017/18 field season (lateral moraine boulders) (Fig. 7.7). Boulders were selected for sampling based on their evidence for stability in the drift. We preferentially selected boulders that were partially buried in supraglacial debris, and that otherwise showed no signs of overturning due to cryoturbation processes post-deposition. We also selected boulders that rose > 50 cm from the debris surface to limit burial by snow. For the middle drift samples (sample prefixes 11-OV-ER*, Fig. 7.5), we identified samples in the center of the valley to avoid any rockfall from the valley wall. For the lateral moraine boulders (sample prefixes 17-OV-ERR*, Fig.

7.5) on the valley wall, we avoided rectangular boulders that were perched on the debris surface as these appeared to be jointed boulders more recently eroded out of the bedrock. At all sites, deeply weathered boulders were avoided in an attempt to limit samples with complex exposure histories. All boulders sampled were either granite or gneiss that contained a high percentage of quartz. With a hammer and chisel, we removed a 1-2 kg sample from the top of each boulder. GPS location, exposure geometry, and sample thickness were recorded. Boulders in the middle of the drift should provide minimum exposure ages for the middle drift as they were exposed as the middle ice has sublimated.

Figure 7.7 Photographs of surface boulders sampled from (a-c) the middle drift surface and (d-f) the East lateral moraine; (a) 11-OV-ER-117, (b) 11-OV-ER-118, (c) 11-OV-ER-119, (d) 17-OV-ERR-213, (e) 17-OV-ERR-217, and (f) 17-OV-ERR-218.

7.2.2 Sample Processing

7.2.2.1 Sample Preparation

Each ice core segment containing visible englacial debris was weighed before the ice was melted at room temperature. The liquid was then separated from the englacial debris, and the debris was oven dried at ~70°C. Then the samples were re-weighed. Resulting masses of ice and debris in each core segment were then used to compute the density of the core using Eq. (24). Figure 7.8 shows pictures of the core and corresponding debris concentrations (blue) by weight as the function of depth. The ice core alternates between sections of clean ice and debris rich ice with a maximum debris concentration of 0.57 by weight. Ice core segments with little or no debris were assumed to have the density of $_{ice,}$ 0.917 g cm^{-3}.

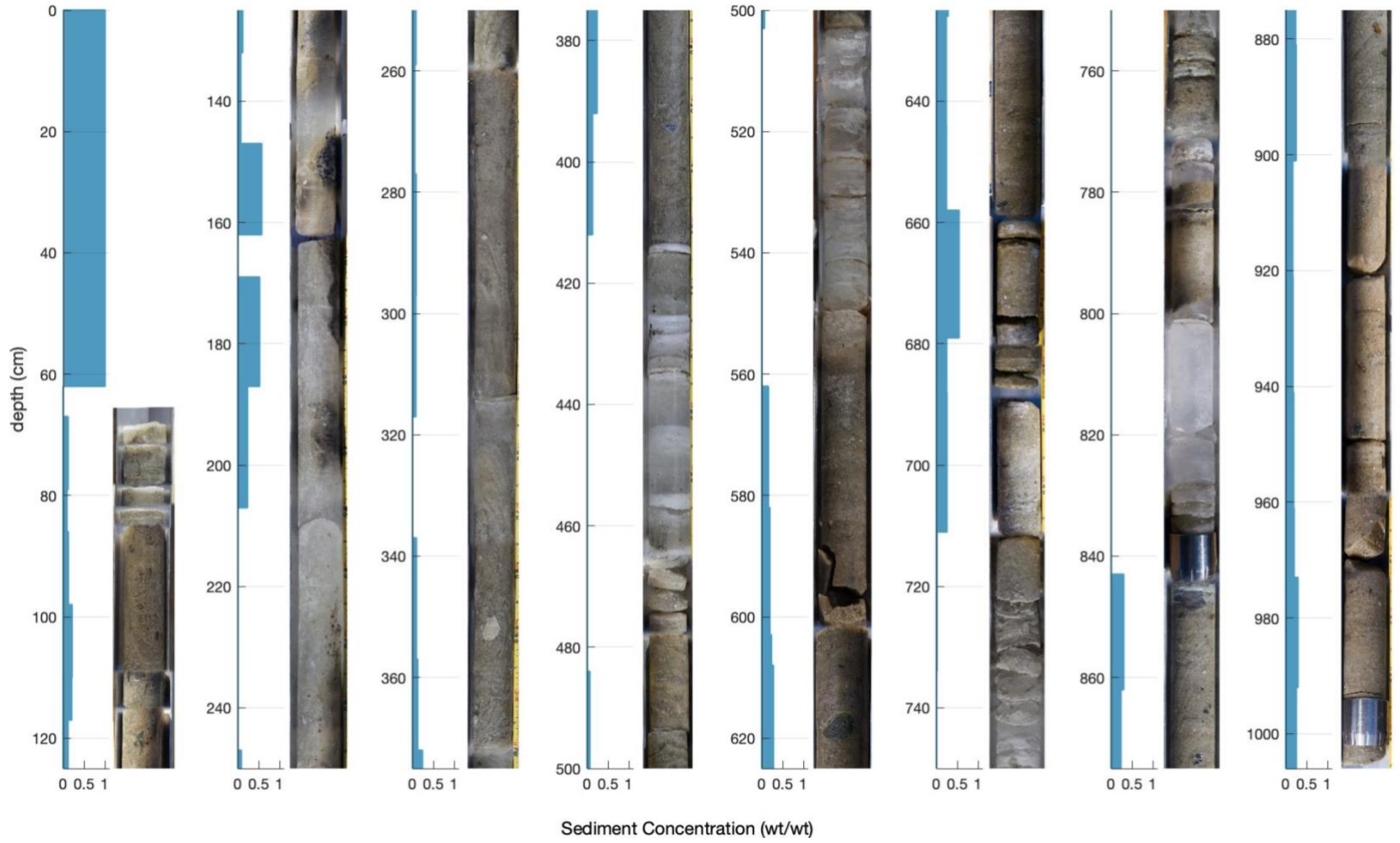

Figure 7.8 Image of the 17-OD1 ice core. The full image is stitched together from multiple individual pictures each covering approximately 20 cm of core length. The blue graph shows the corresponding debris concentration calculated by weight at depth below the surface. The topmost 62 cm is the thickness of the overlying supraglacial debris layer (not shown in pictures).

The density of the supraglacial debris was measured by packing the sediment sample into a measuring cup of known volume and weighing it. This process was repeated five times for each sample to obtain a representative mean density of the supraglacial debris of ~1.8 g cm^{-3}, excluding grains > 2 cm.

For cosmogenic nuclide analyses, the pit samples from the supraglacial debris were sieved to separate a grain size fraction of 250-500 μm, and the englacial debris was sieved to a grain size of 250-833 μm. This was done to maximize the amount of sample for cosmogenic nuclide analyses. Quartz grains were isolated and cleaned following the procedure described in Stone (2004). When needed, adjacent segments were merged so that enough quartz was available to permit precise beryllium and aluminum measurements (see Table 8.2 for details).

7.2.2.2 Cosmogenic Nuclide Extraction and Analysis

After quartz preparation but prior to dissolution for Be-Al extraction, a ~0.5 g aliquot of the prepared quartz was split off for ^{21}Ne measurements. These employed the "Ohio" noble gas mass spectrometer and extraction line at the Berkeley Geochronology Center (BGC). Details of neon (Ne) isotope measurements on this system are described in Balco and Shuster (2009) and Balter-Kennedy et al. (2020). ^{21}Ne concentrations in replicate analyses of the CRONUS-A intercomparison standard (Vermeesch et al., 2015) measured during analytical sessions in this study ranged from 314.3 ± 9.4 to 320.8 ± 6.1 Matoms g^{-1}, indistinguishable from the accepted value of 320 Matoms g^{-1}. In Tables 8.2 and 8.3, and in Appendix C , we report ^{21}Ne concentrations as excess ^{21}Ne relative to atmospheric composition. Excess ^{21}Ne includes both cosmogenic ^{21}Ne

and, potentially, nucleogenic ^{21}Ne derived from uranium (U) and thorium (Th) decay. U and Th concentrations in quartz from Ong Valley lithologies (Sams, 2016), expected Ne closure ages of these lithologies, and the observation that ^{21}Ne concentrations in drift and boulder samples from the youngest drift are significantly higher than expected for the LGM age of that drift, all indicate that nucleogenic ^{21}Ne is significant in quartz in these lithologies. For samples from supraglacial and englacial debris used to fit our forward model for nuclide accumulation, we did not make a correction for nucleogenic ^{21}Ne because it would be equivalent to inherited cosmogenic ^{21}Ne in our model simulations. Thus, such a correction would not affect values for ages or process rates inferred from the model simulations. In calculating exposure ages and erosion rates for boulder samples, we corrected for nucleogenic ^{21}Ne using an estimate of 7 ± 3 Matoms g^{-1} obtained from ^{21}Ne data on boulders of similar lithology from the youngest drift (Sams, 2016). With this estimate, nucleogenic ^{21}Ne comprises 2-7% of total excess ^{21}Ne in boulder samples. In addition, as discussed below, we applied this correction to subsurface samples used for burial dating.

Chemical extraction and preparation of beryllium and aluminum from remaining quartz extracted from drill core samples were performed at the University of Vermont/National Science Foundation (UVM/NSF) Community Cosmogenic Facility following the process described in Corbett et al. (2016). Description, reasoning, and chemical processes for each procedural step preformed at the (UVM/NSF) Community Cosmogenic Facility is detailed in the Appendix D. The pit and ice core samples were processed in two separate batches of 12 samples, in which each batch included a process blank and a standard. For all samples, 250 µg ^{9}Be was added with a beryl carrier made at the facility with a concentration of 291 µg mL^{-1}. In addition, a ^{27}Al carrier commercially available as an ICP standard from SPEX with a concentration of 1000 µg mL^{-1} was

added only to samples having < 1500 μg, of total Al. The amount of ^{27}Al carrier added was based on the total amount of native ^{27}Al in a sample quantified by Inductively Coupled Plasma Optical Emission Spectroscopy (ICP-OES) analysis. Quartz isolation and beryllium extraction for boulder samples followed the same procedure, except that three of the boulder samples (11-OV-ER-117, 118, 119) were processed in chemistry laboratories at the Center for Accelerator Mass Spectrometry, Lawrence Livermore National Laboratory (LLNL-CAMS).

Ratios of ^{10}Be/^{9}Be measured at Lawrence Livermore National Laboratory (LLNL) are normalized to the 07KNSTD3110 standard (Nishiizumi et al., 2007) with an assumed ^{10}Be/^{9}Be ratio of 2.85 x 10^{-12}. All ^{26}Al/^{27}Al ratios were measured at PRIME and normalized to the KNSTD-01-5-2 standard (Nishiizumi, 2004) with an assumed ^{26}Al/^{27}Al ratio of 1.818 x 10^{-12}.

Both ^{10}Be and ^{26}Al measurements were corrected for background using a procedural blank measured in each batch. Procedural blanks run with samples from the core site and were 14.9 ± 3.3 x 10^3 and 49.8 ± 9.4 x 10^3 atoms ^{10}Be and 259 ± 45 x 10^3 and 37 ± 20 x 10^3 atoms ^{26}Al, and blanks run with boulder samples ranged from 24-109 x 10^3 atoms ^{10}Be. For the majority of samples, blank corrections account for less than 1% of total ^{10}Be or ^{26}Al atoms present. The exception is several samples of englacial debris from the ice core, for which blank corrections were up to 4% of total ^{26}Al atoms present and up to 9% of total ^{10}Be atoms present. The reported uncertainty in the measured nuclide concentrations accounts for all sources of analytical errors, including AMS measurement uncertainties, concentration measurement of ^{10}Be and ^{26}Al, and procedural blanks. Measurement details appear in the Appendix C.

7.2.3 Forward Exposure Model

The exposure history of the middle drift in Ong Valley is complex, and the nuclide production cannot be accounted for by simply exposure-dating the supraglacial debris. Therefore, we apply a forward model which attempts to account for the geological processes that result in the thickening of the supraglacial debris and accumulation of cosmogenic nuclides at depth. As described in Bibby et al. (2016) , the concentration of cosmogenic nuclides in the ice mass and the supraglacial debris is expected to result from a series of events: i) debris rich glacial ice was deposited into Ong Valley during glacial advancement, ii) the ice mass became stagnant and began to sublimate which caused the englacial debris to accumulate on the ice surface as a supraglacial debris layer; iii) as the ice continued to sublimate additional debris was added to the supraglacial debris layer from below, bringing deeper samples closer to the surface; iv) at the same time the supraglacial debris layer was subjected to surface erosion at a rate slower than the accumulation of debris from sublimation, such that the supraglacial debris thickness increased with time. The present-day thickness of the supraglacial debris layer is therefore a function of the age of ice emplacement, rate of ice sublimation, concentration of debris in ice, and rate of surface erosion. The numerical forward model attempts to account for the series of events listed above which lead to the cosmogenic nuclide concentrations measured today at depth below the surface in the middle ice. Input parameters to the model include the age of ice emplacement, the sublimation rate of the ice, and the surface erosion rate of the supraglacial debris layer. The model then predicts nuclide concentrations in supraglacial and englacial debris. By fitting the model to the observed nuclide concentrations, we obtain estimates for the age of the ice and for sublimation/erosion rates.

7.2.3.1 Shielding Mass

The production rate of cosmogenic nuclides at and below the surface is dependent on the shielding mass which attenuates the cosmic ray flux. The shielding mass is the cumulative mass of sediment and ice overlying each sample per unit area and has units of g cm^{-2}. It is equal to the product of the sample depth (cm) and the mean density of the overlying material (g cm^{-3}). The density is related to the concentration of the suspended debris C_D and the ice C_I in each core segment, and is calculated from the total segment weight, M_t (g), and dried sediment weight, M_s (g) such that,

$$C_D = \frac{M_s}{M_t} \tag{21}$$

$$C_I = 1 - C_D \tag{22}$$

The density of the ice core can then be calculated by mixing the two ice core components based on volume. Assuming the density of the ice ρ_I to be 0.917 g cm^{-3} and the density of the debris ρ_D to be that of rock, 2.68 g cm^{-3}, for an ice core segment weight of 1 g, the total weight of the ice core segment is then,

$$M_t = C_D + C_I \tag{23}$$

resulting in the density of the ice-debris mixture in an ice core segment ρ_M to be,

$$\rho_M = \frac{1}{\left(\frac{C_D}{\rho_D}\right) + \left(\frac{C_I}{\rho_I}\right)} \quad (24)$$

7.2.3.2 Depth as a Function of Time

Once an ice mass with a mixture of ice and debris is emplaced at some time in the past defined as T (yr), the shielding mass above a given sample in the ice is decreasing through time at the rate determined by the sum of the sublimation rate of the ice and the surface erosion rate of the supraglacial debris. As the sample reaches the top of the ice, it becomes part of the supraglacial debris and then approaches the surface solely at the rate of surface erosion. The sublimation rate, s (cm yr^{-1}) is defined as a constant rate in which the surface of the ice-debris mixture (bottom of the supraglacial debris layer) is lowering. Note that this parameter represents a surface lowering rate due to sublimation and is not the same as a sublimation rate of pure ice as would be considered in a thermodynamics context. Therefore, the initial surface of the ice mass is sT (cm) above the present surface.

The rate at which mass is being lost by sublimation is the product of the sublimation rate and the density of the sublimating material. Since the ice mass consists of a mixture of ice and debris, only part of the ice mass is sublimating. The rate of mass loss associated with sublimation is given by $s(1 - C_D)\rho_M$ (g cm^{-2} yr^{-1}). While the ice is sublimating, the debris suspended in the ice mass is left behind on the ice surface and accumulating as supraglacial debris. The rate at which mass is added to the bottom of the supraglacial debris by sublimation is then, $sC_D\rho_M$ (g cm^{-2} yr^{-1}). By assuming that at time of emplacement, the thickness of the supraglacial debris above the ice

mass was zero, then with constant sublimation rate and erosion rate the total mass thickness of the supraglacial debris, Z_{till} (g cm^{-2}) created by ice sublimation can be expressed as

$$Z_{till} = TsC_D\rho_M - TE \tag{25}$$

Where T is the age in years before present the ice was emplaced, and E is the erosion rate expressed in mass units (g cm^{-2} yr^{-1}). Equation (25) leads to the constraint that $sC_D\rho_M > E$, as the thickness of the supraglacial debris cannot be negative.

From field measurements, the thickness of the supraglacial debris is known to be 110 g cm^{-2} for 17-OD1-Pit2. Therefore, for any arbitrary values of age, sublimation rate, and erosion rate, the debris concentration must be chosen such that the measured supraglacial debris mass thickness is obtained after T years. Assuming the ice mass mixture only consists of ice and debris, then the term C_D and ρ_M are different representations of the debris mass embedded in the sublimating ice.

Multiplying Eq. (24) with C_D, the debris concentration of the lost mass associated with sublimation can be solved,

$$C_D = \frac{\rho_D(C_D\rho_M)}{\rho_D\rho_I - (\rho_I - \rho_D)(C_D\rho_M)} \tag{26}$$

Equation (25) and (26) are two independent equations including the term $C_D\rho_M$. By isolating and substituting the term $C_D\rho_M$ in Eq. (25) into Eq. (26) the debris concentration now

becomes independent of density of the ice core, and instead a function of sublimation rate (s), erosion rate (E) and age of ice emplacement (T),

$$C_D = \frac{\rho_D \left(\frac{Z_{till} + TE}{Ts}\right)}{\rho_D \rho_I - (\rho_I - \rho_D)\left(\frac{Z_{till} + TE}{Ts}\right)} \tag{27}$$

The debris concentration is constrained such that $0 \geq C_D \leq 1$.

When predicting the concentration of cosmogenic nuclides, it is crucial to know a sample's depth at present, defined as $Z_{S,now}$ in units of mass depth (g cm^{-2}), and its depth at some time, t (yr) in the past, $z(t)$. Since the samples collected consist of both ice core samples and sediment from the above laying supraglacial debris, there are two separate cases of how a sample has approached the surface in the past.

In case 1, the sample is in the ice at present such that the sample depth is greater than the depth of the supraglacial debris, $Z_{S,now} > Z_{till}$. From time of ice emplacement, the sample has then approached the surface at the rate of the ice sublimating and the rate of surface erosion, such that

$$z(t) = Z_{s,now} + ts(1 - C_D)\rho_M + tE \tag{28}$$

In case 2, the sample is in the supraglacial debris at present, such that , $Z_{S,now} < Z_{till}$. The time that the sample has been in the supraglacial debris is then defined as the mass height of the

sample above the supraglacial debris base depth divided by the rate of mass addition to the supraglacial debris,

$$T_{till} = \frac{\left(Z_{till} - Z_{S,now}\right)}{sC_D\rho_M} \tag{29}$$

By the time of emplacement, the sample has then approached the surface in the same way as above. However, once the sample reaches the top of the ice and becomes part of the supraglacial debris, it approaches the surface at the rate of surface erosion only. This further allows for two scenarios to occur.

In case 2a, if at time t the sample is in the supraglacial debris, such that $t < T_{till}$, then

$$z(t) = Z_{S,now} + tE \tag{30}$$

In case 2b, if at time t, the sample is in the ice, where $t > T_{till}$, then

$$z(t) = Z_{S,now} + T_{till}E + (t - T_{till})(s(1 - C_D)\rho_M + \mathrm{E}) \tag{31}$$

With this, it is now possible to calculate the depth of a sample at any given time in the past since the ice emplacement. This is needed in order to predict the total accumulation of nuclides in a sample, which is dependent on the nuclide production at depth.

7.2.3.3 Cosmogenic Nuclide Production at Depth

The cosmogenic nuclides ^{10}Be, ^{26}Al, and ^{21}Ne are produced by high-energy spallation, negative muon capture, and fast muon interactions (Dunai, 2010). The high-energy spallation particles are likely to react with mass in the atmosphere and at Earth's surface. Therefore, the production of cosmogenic nuclides due to spallation reaction is highest at the surface and considerably decreases with depth. Muons are much less likely to interact with mass, and therefore travel farther below the surface before stopping (Lal, 1991). While cosmogenic nuclide production at depth below the surface is solely due to muon production, muons are responsible for less than 1% of the total production at the surface for all nuclides (Balco, 2017).

We calculated the ^{10}Be production rate using the 'LSDn' scaling method (Lifton et al., 2014) as implemented in version 3 of the online exposure age calculator originally described by Balco et al. (2008) and subsequently updated, and the CRONUS-Earth "primary" calibration data set (Borchers et al., 2016). This yields a long-term (> 1 Ma) average production rate due to spallation of 25.3 atoms ^{10}Be g^{-1} quartz yr^{-1}. We then assumed that the ^{21}Ne/^{10}Be production ratio is 4.03 (Balco et al., 2019) and the ^{26}Al/^{10}Be production ratio is 6.75 (Balco et al., 2008).

The spallation production rate at the surface $P_{sp}(0)$ for a given cosmogenic nuclide decreases exponentially with depth (Lal, 1991), such that

$$P_{sp}(z) = P_{sp}(0)\, e^{\left(\frac{-z}{\Lambda}\right)} \tag{32}$$

Where z is the mass depth (g cm^{-2}) and Λ is the attenuation length, defined as the distance where the energetic cosmic-ray flux intensity reduces by a factor of e^{-1} due to scattering and absorption processes. The attenuation value varies depending on altitude and latitude and is taken to be 140 g cm^{-2} in Antarctica for ^{10}Be, ^{26}Al, and ^{21}Ne (Balco et al., 2019; Borchers et al., 2016).

Muon production rates are not well approximated by a single exponential function. As depth increases, the energy of the remaining muons that have not yet stopped is higher, and therefore it takes proportionally longer for those to stop. The calculations of the production rates due to negative muon capture follows that of Heisinger et al. (2002a) and production rates due to fast muon interactions according to Heisinger et al. (2002b) and are combined into a total muon production rate at depth, $P_\mu(z)$. The surface topography surrounding the sampling site also shields the samples of cosmic rays and will need to be accounted for when computing the production rate. This topographic shielding scaling factor S_G is applied to the spallation and not the muon production rate (Balco et al., 2008). A topographic shielding of 0.993 was measured for drill site 17-OD1. The total production rate as function of depth can then be described as,

$$P(z) = S_G P_{sp}(z) + P_\mu(z) \tag{33}$$

The influence of each production path on the total production rate can be observed in Fig. 7.9. Since the density of the ice is less than that of debris, the production of cosmogenic nuclide due to spallation decrease less rapidly with depth below the surface and is responsible for 12-20% of the total production rate for the cosmogenic nuclides ^{10}Be, ^{21}Ne and ^{26}Al at the bottom of the ice core.

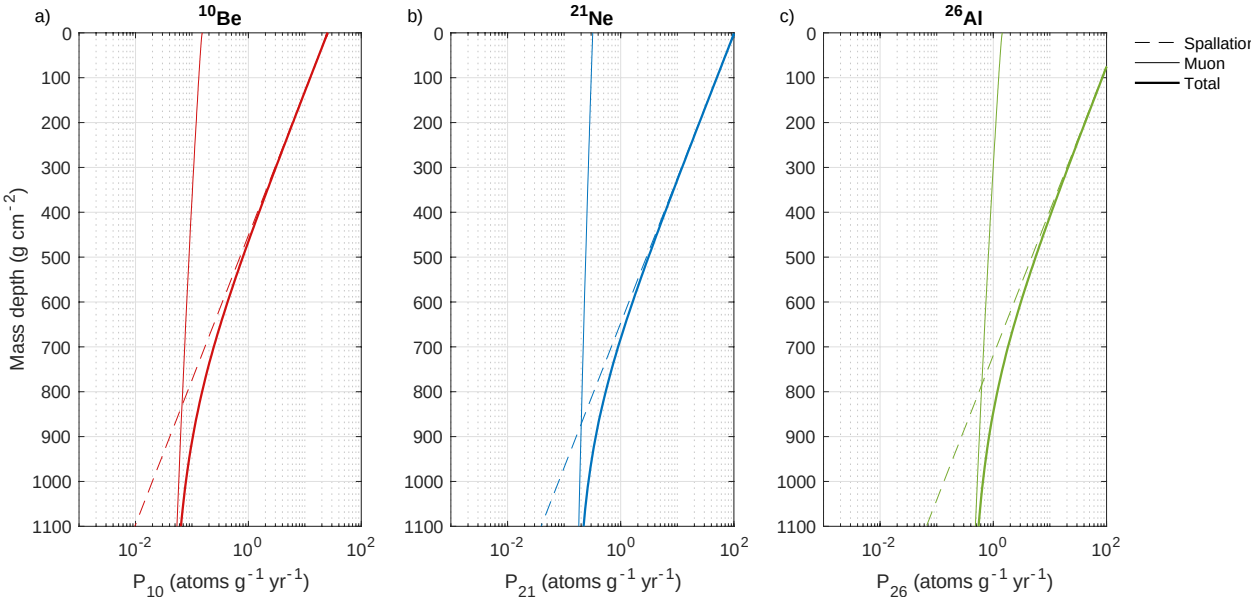

Figure 7.9 Change in production rate with depth for the cosmogenic nuclide (a) ^{10}Be, (b) ^{21}Ne, and (c) ^{26}Al. The lines represent production due to spallation (dashed), muon (solid thin), and the total production (solid thick).

In Fig. 7.10 we show the calculated changes in mass depth and production rate for a sample collected in the supraglacial debris 50 cm below the surface. The following arbitrary, but illustrative model parameter values are used for ice emplacement age, sublimation rates, and erosion rates: 1 Ma, 20 m Myr^{-1}, and 0.1 m Myr^{-1} respectively. The supraglacial debris thickness is that measured at drill site 17-OD1 and is 62 cm (110.15 g cm^{-2}). From the time of ice emplacement, a sample's depth has decreased linearly due to ice sublimation and surface erosion as the age of the ice increases, with a distinct change in rate once the sample exits the ice and becomes part of the supraglacial debris following that of Eq. (30) and Eq. (31). It is also observed that such samples experience great changes in nuclide production rates, following that of Eq. (33), from time of emplacement until present.

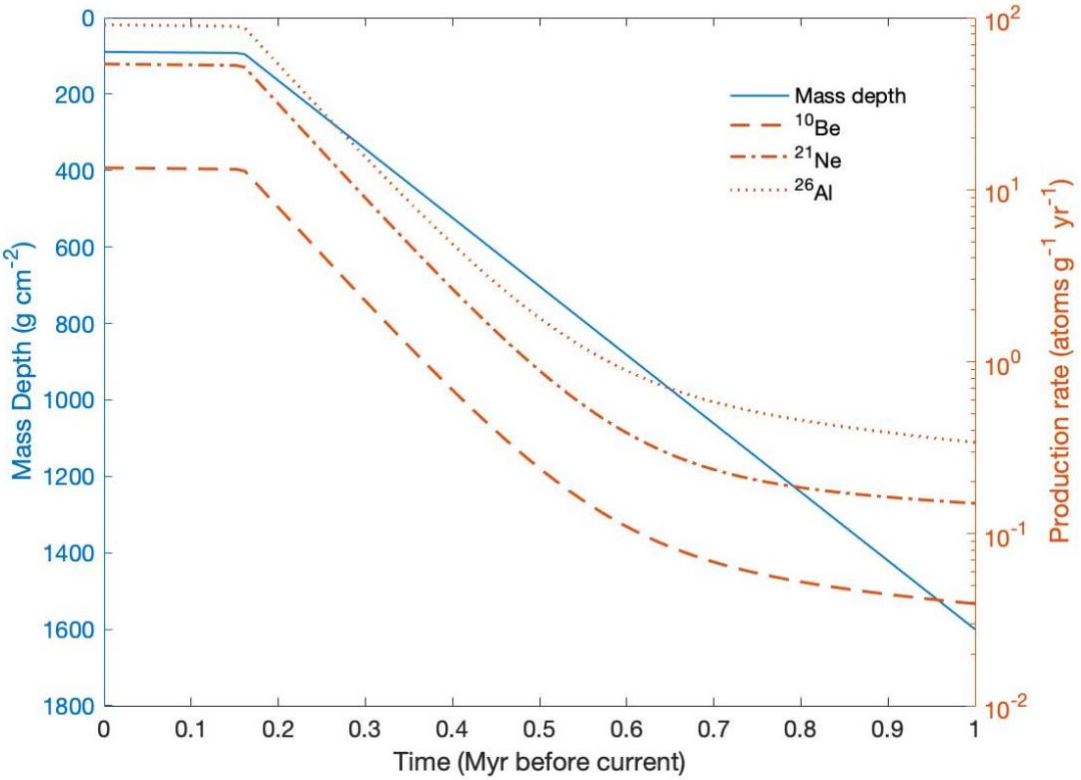

Figure 7.10 Graphical representation of the temporal change in mass depth (blue line) and production rates (orange lines) since ice emplacement for a sample found today at 90 g cm-2 (~50 cm below the surface) in the supraglacial debris. Here, the given sample has an initial shielding mass of 1600 g cm-2 (~14 m) and approaches the surface at the combined rate of sublimation and erosion (Eq. 31). Once the sample reaches the ice surface it becomes part of the supraglacial debris (~0.2 Ma) and approaches the surface solely at the rate of surface erosion (Eq. 30). As the sample's mass depth decreases it experiences considerable changes in production rates of cosmogenic nuclides (Eq. 33). The arbitrary model parameter values for these calculations are: 1 Ma ice emplacement, 20 m Myr-1 sublimation rate, and 0.1 m Myr-1 erosion rate.

7.2.3.4 Predicting Cosmogenic Nuclide Concentrations at Depth

When exposed to cosmic-rays, a sample will begin to accumulate cosmogenic nuclides over exposure time T, such that the total accumulation, N (atoms g^{-1}) in a subsurface sample at depth z (g cm^{-2}) can be expressed as the integral of the production rate a sample undergoes from time of ice emplacement to the present. Since the exposure history of the englacial debris goes beyond the exposure history of the ice mass, some amount of inherited background nuclides N_{inh} (atoms g^{-1}) is present. While the concentration of the stable cosmogenic nuclide ^{21}Ne continues to build up, some of the unstable radionuclides, ^{10}Be and ^{26}Al, are lost to radioactive decay. This is expressed as an exponential, such that the total number of cosmogenic radionuclides for a sample can be calculated using Eq. (34) and simplified to Eq. (35) for the stable nuclide ^{21}Ne.

$$N_i = N_{i,inh} e^{(-\lambda_i T)} + \int_0^T P_i\big(z(t)\big) e^{(-\lambda_i t)} dt \tag{34}$$

$$N_{21} = N_{21,inh} + \int_0^T P_{21}\big(z(t)\big) dt \tag{35}$$

The subscript i refers to the radionuclide of interest, ^{10}Be or ^{26}Al, and λ_i is the decay constant for the radionuclide i. The decay constants used in this paper are 4.99 x 10^{-7} and 9.83 x 10^{-7} for ^{10}Be and ^{27}Al, respectively. We evaluate these integrals numerically using the default algorithm (integral) in MATLAB.

Given a set of environmental conditions; i) age of ice emplacement, ii) sublimation rate of ice, iii) surface erosion rate of the supraglacial debris, and iv) inherited nuclide concentration for each of the nuclides, as well as measurable site conditions (e.g., elevation and supraglacial debris thickness) Eq. (34) and Eq. (35) predicts the current total cosmogenic nuclide concentration in a sample at a unique depth *z* at present time.

7.2.3.5 Model Fitting Statistics

Modeled results are obtained by comparing the observed nuclide concentrations with those predicted by the model. However, the measured cosmogenic nuclide concentration is not related to a single depth but rather a sample segment range in depths. As discussed in sect. 7.2.2.1, there are some cases where adjacent segments were merged to allow for enough quartz to permit precise nuclide measurements. Therefore, a measured sample segment consists of one or more subsamples, each with varying subsegment depths and amount of quartz present, which needs to be accounted for. The average predicted cosmogenic nuclide concentration within a segment if found by using the Reimann sum and a trapezoidal integration method. When comparing the predicted cosmogenic nuclide concentration with that of the measured in a thick sample segment, the predicted cosmogenic nuclide concentration $N_{i,p}$ then become

$$N_{i,p,j} = \frac{\sum_k N_{i,p,j,k} W_{qtz,j,k}}{\sum_k W_{qtz,j,k}} \tag{36}$$

The subscript i refers the cosmogenic nuclide of interest and k is the subsample in a sample segment j, where W_{qtz} is the weight of quartz.

A misfit statistic is defined by comparing observed nuclide concentrations with those predicted by the model as the reduced χ^2 statistic weighted by the relative uncertainty in measurements of all three nuclide concentrations in each sample, such that

$$\chi^2 = \sum_i \sum_j \left(\frac{N_{i,p,j} - N_{i,j}}{N_{i,j}} \right)^2 \quad (37)$$

A best fit is found using the constrained nonlinear multivariable optimizing function (fmincon) in MATLAB while optimizing for the free parameters; (i) the age that the ice was emplaced, (ii) sublimation rate of the ice since emplacement, (iii) surface erosion rate of the accumulating supraglacial debris, and (iv) the inherited nuclide concentrations in the englacial debris at the time of ice emplacement.

Uncertainty distributions on the best-fit values of the model parameters are derived from a 10,000-iteration Monte Carlo simulation. Each Monte Carlo iteration draws from a set of normally distributed uncertainty for the measured nuclide concentrations and uses an initial guess for the free model parameters based on published values for the middle drift in Ong Valley (Bibby et al., 2016); 1.83 Ma ice emplacement age, 22.7 m Myr^{-1} sublimation rate, 0.89 m Myr^{-1} surface erosion rate, and inherited nuclide concentration of 0.14 x 10^6 atom g_{qtz}^{-1}, 11.4 x 10^6 atom g_{qtz}^{-1}, and 0.82 x 10^6 atom g_{qtz}^{-1} for ^{10}Be, ^{21}Ne, and ^{26}Al, respectively. Although uncertainties in calculated nuclide

production rates are similar in magnitude to the uncertainty measured in nuclide concentrations, they are not included in these results as all the samples are from the same location, and therefore must have the same surface production rate. Further, any of the Monte Carlo simulation results which did neither converge nor satisfy the optimization function evaluation or resulted in an ice emplacement age younger than the LGM (< 20ky) were excluded.

7.2.3.6 The Sensitivity of the Modeled Nuclide Concentrations to Model Parameters

The application of cosmogenic nuclide depth profile that reaches depths dominated by muon production, limits the potential of the parameters, having multiple combination that could yield a best fit (Braucher et al., 2009; Stone et al., 1998). The effect that sublimation rate, erosions rate, and exposure age have on total build-up of cosmogenic nuclide concentrations in the supraglacial debris and englacial debris varies greatly with depth (Fig. 7.11).

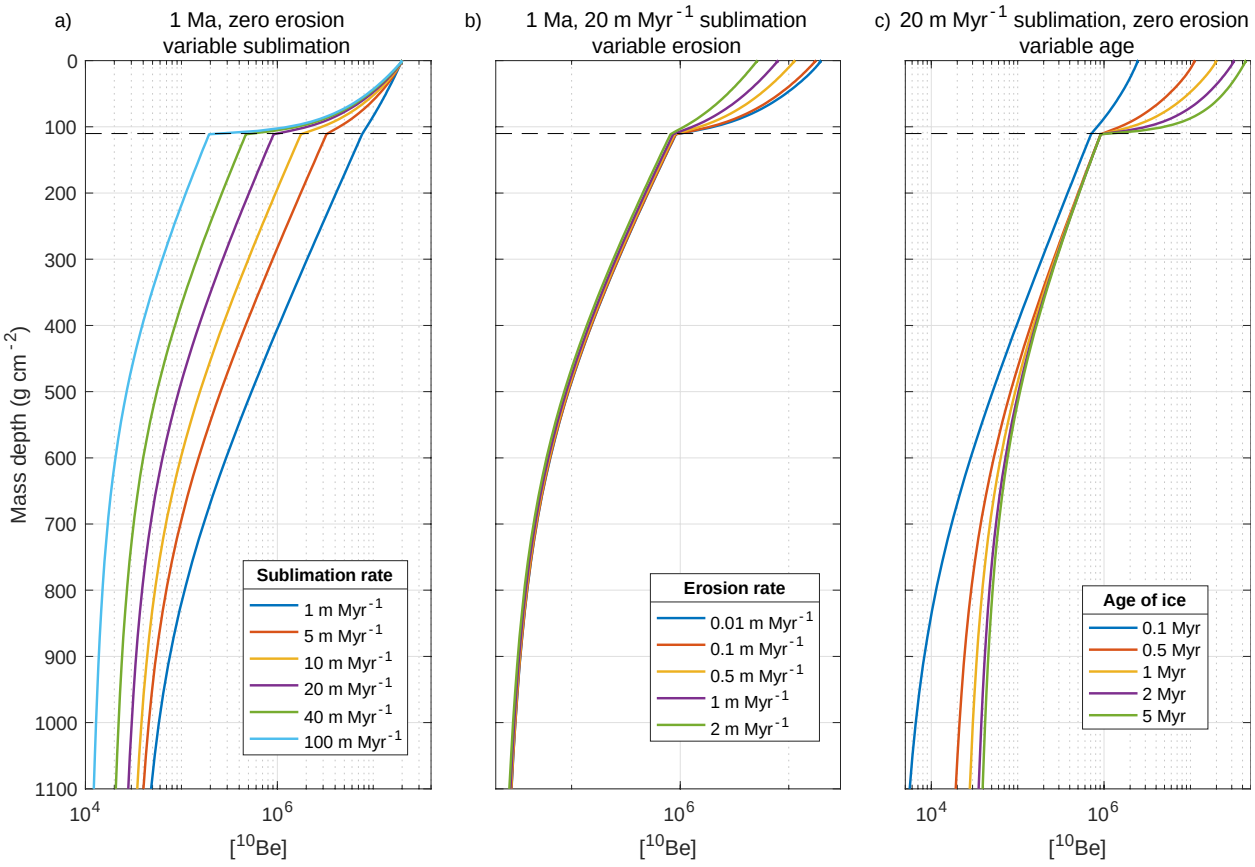

Figure 7.11 Prediction of cosmogenic nuclide concentration in the supraglacial debris layer and top meter of the underlying ice with constant age of 1 Ma, 20 m/My sublimation rate and zero erosion, and varying parameters of (a) sublimation rates, (b) surface erosion rates, and (c) age of ice emplacement. Dashed line represents the boundary between the overlying supraglacial debris and the ice surface. The effect of sublimation rates on cosmogenic nuclide concentrations are most eminent in the ice and lower supraglacial debris samples, while erosion rates primarily affect the nuclide concentration in the upper supraglacial debris. The age is not well constrained in the ice nor supraglacial debris in combination with erosion rates. However, as sublimation and erosion rates must corroborate together with the supraglacial debris thickness and debris concentration, the age can be constrained.

The effect of sublimation rate is most prominent in the top meter of the ice (Fig. 7.11a). However, the sublimation can also be observed in the lower samples of the supraglacial debris, as the samples have spent more time within the ice compared to those samples above in the supraglacial debris. With increasing sublimation rate a sample having low nuclide concentration at depth (caused by increased shielding mass) in the ice is approaching the ice surface more rapidly. Having spent less time near the ice surface, a sample found in the top meter of the ice will have a

lower total nuclide concentration. A measured difference in nuclide concentration between the top ice core samples and the lower supraglacial debris samples, aid in the constrain of the sublimation rate.

The effect of erosion rates on cosmogenic nuclide concentrations are primarily observed in the top supraglacial debris samples (Fig. 7.11b). An increased erosion rate lowers the total nuclide concentration at the current surface as shielded lower concentration debris are brought to the surface at a higher rate, while higher nuclide concentrations at the surface are being removed by erosion.

Concentrations of cosmogenic nuclides produced by spallation at an eroding surface reaches equilibrium more rapidly than those produced at depth predominantly by deeper penetrating muons. Therefore, cosmogenic nuclide concentrations produced at several meters' depth can be used to constrain the age of ice emplacement (Fig. 7.11c). It should be noted that the variation in predicted cosmogenic nuclide concentrations observed at the surface of the supraglacial debris cause by an increase in age, is the result of zero erosion as modeled here. However, as the erosion increases, this difference in prediction cosmogenic nuclide concentration near the surface becomes less apparent.

Sublimation and erosion rates must corroborate together with other measurable geological features (e.g., supraglacial debris thickness and debris concentration in the ice) within the age frame to produce a supraglacial debris thickness observed today. Previous model predictions of cosmogenic nuclide concentrations in a depth profile from supraglacial debris overlying buried ice

(Morgan et al., 2010a, Bibby et al., 2016) does not account for such relationship. Therefore, previous models do not account for the unique distinction of measured cosmogenic nuclide concentrations between the supraglacial debris and ice boundary, and therefore cannot uniquely solve for an absolute age, but rather a minimum age.

CHAPTER 8
RESULTS

8.1 Moraines Mapping Results

Based on the mapping of the lateral and terminal moraines in Ong Valley it is evident that the Argosy Glacier has, during glacial advancement, expanded up and into the valley at least three times, leaving behind glacial drifts; previously identified by Bibby et al. (2016) as the old, middle and young drift (Fig. 8.1 and Fig. 8.2). Using both field observations, moraine mapping, two-dimensional profile, and DSM, we are able to correlate between the mapped lateral and terminal moraines and assign inferred boundaries. Further, we find that majority of the moraines can be continuously traced across the valley walls (Fig. 8.2).

The current, exposed Argosy Glacier lobe in Ong Valley is found at the valley mouth at an elevation of 1480 masl. The farthest advancement observed in the valley is that of the old drift. This advancement is well defined by a 1.8 km long, uninterrupted terminal moraine near the valley head. The old terminal moraine is found 6.2 km up valley from the Argosy Glacier lobe and at an elevation of 1725 masl. This results in at least a 245 m increase of ice surface elevation above current in Ong Valley during the deposition of the old drift. The highest lateral moraine that can be correlated to the old terminal moraine is found at 1920 masl on the East valley wall close to the valley mouth, and is 440 m above current ice elevation.

The extent of the middle drift is defined by a 330 m long terminal moraine positioned on the western side of the drift. This terminal moraine is found 4.9 km from the Argosy Glacier lobe at an elevation of 1645 masl, and therefore it is 165 m above current ice elevation. The current extent of the middle ice, buried below supraglacial debris, is located 110 m down valley from the middle terminal moraine at an elevation of 1636 masl, indicating that this part of the middle drift is depleted of ice. Further, we find that the highest point of the middle ice (along the topographic profile) is at 1695 masl, providing a minimum increase in elevation of the Argosy Glacier of 215 m above current during the deposition of the middle ice.

The drill site 17-OD1, located centrally within the middle drift is found at 1685 masl, using the DSM (Fig. 8.1). From the drill site and directly perpendicular to the valley wall, the current middle ice boundary is found at an elevation of 1699 masl and 1694 masl for the East and West valley wall, respectively. This results in the current boundary of the middle ice to be 9-14 m above the drill site. Further, the lateral moraines associated with the emplacement of the middle ice is 1722 masl. This provides an ice surface lowering, local to the drill site, of at least 37 m since emplacement.

The most recent advancement has been dated to occur during the LGM (11-13 kyr) (Bibby et al., 2016). During the LGM, the Argosy Glacier lobe expanded 2.3 km up valley reaching an elevation of 1600 masl and, therefore, a 120 m increase in ice surface elevation above current.

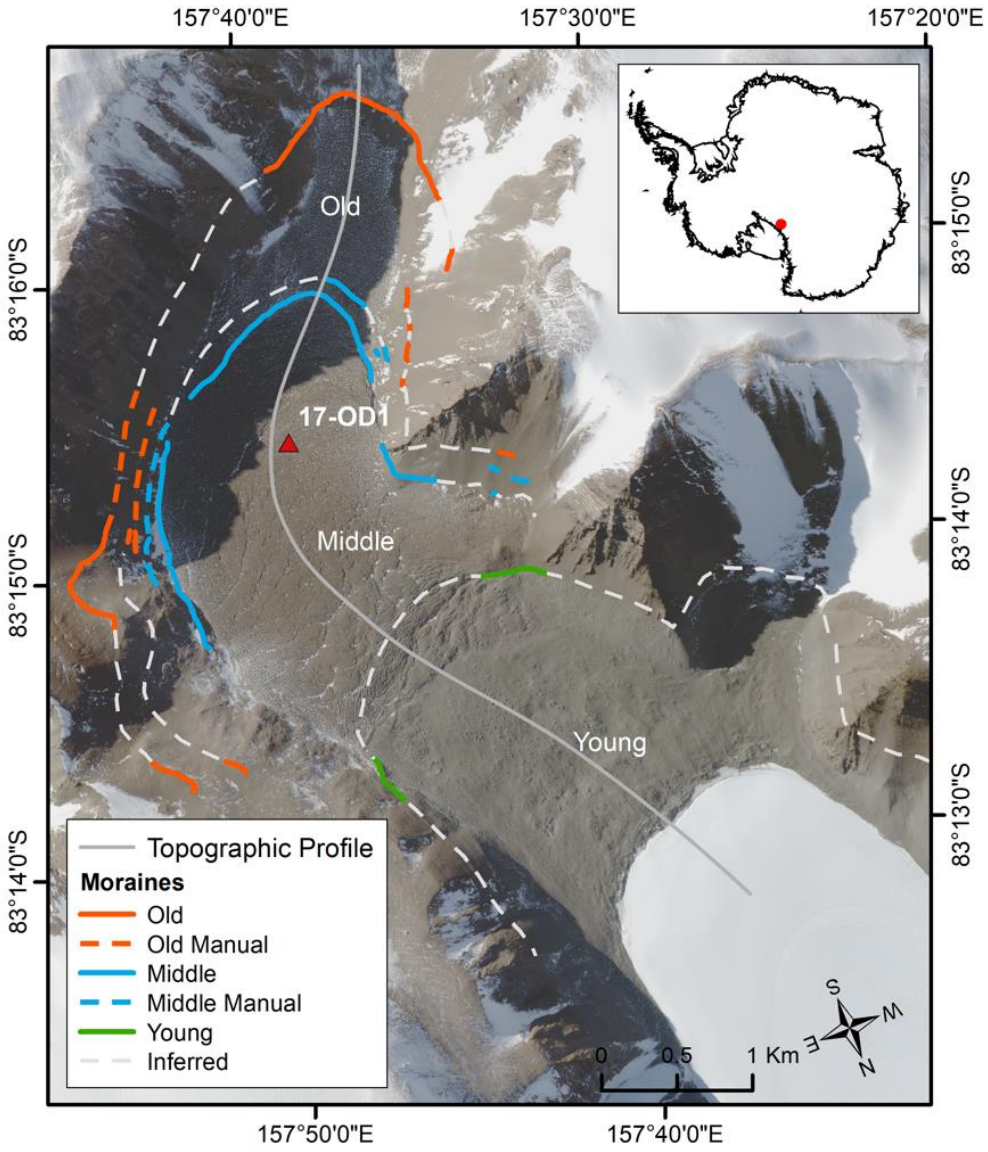

Figure 8.1 Moraine and drift boundaries mapped in Ong Valley, Antarctica (WV2 satellite image © 2016 Maxar). Solid lines indicate the lateral and end moraines traversed for the old drift (orange), middle drift (blue), and young drift (green). Dashed lines indicate the lateral moraines mapped by elevation laser measurement (orange and blue) and inferred from continuously tracing the moraines (white). Also shown is the track of the topographic profile line (solid grey) used for the 2-dimensional topographic profile of Ong Valley (Fig. 8.2) and the location of the 17-OD1 drill site for reference (red triangle).

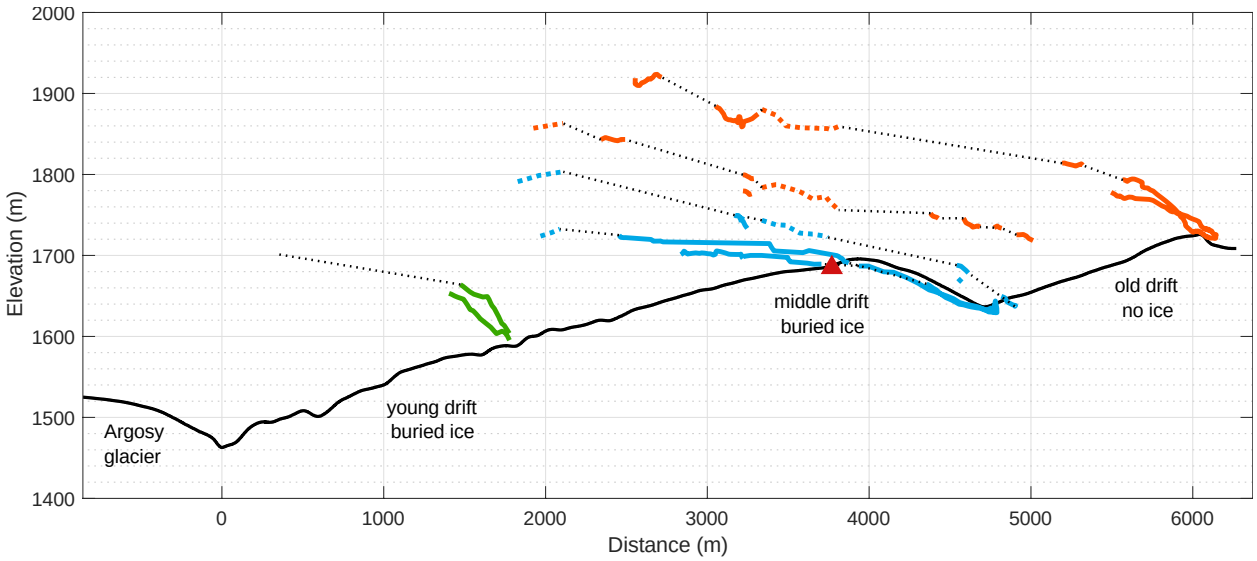

Figure 8.2 Longitudinal topographic profile along the valley floor of Ong Valley, Antarctica. The horizontal axis represents the distance along the topographic profile (black solid line) from the Argosy Glacier lope positioned at the mouth of Ong Valley. Elevation data is obtained from a 1-m resolution, time-stamped Digital Surface Model (DSM) with a vertical exaggeration (VE) of 5. Colored solid lines indicate the lateral and end moraines traversed for the old drift (orange), middle drift (blue), and young drift (green). Dashed lines indicate the lateral moraines mapped by elevation laser measurement (orange and blue) and inferred from continuously tracing the moraines (black). Also shown is the location of the 17-OD1 drill site for reference (red triangle).

8.2 Boulder Movement Results

We measured the position of eight boulders located on the surface of the three drifts in Ong Valley during the Austal summers of 2010, 2011, and 2017 in order to determine if any recent surface movement has occurred. A boulder is considered to have moved if the distance between any of the measured points for any temporal interval is larger than the measurement uncertainty. By movement, we refer to any vertical, and/or horizontal movement, or slight tilt in the boulder that causes the bolt position to have changed. With a 95% confidence interval, we find that four of the eight boulders (OV-GPS-03, 06, 07, and 08) indicate movement in both the horizontal plane and three-dimensional space between the different measurement periods (Fig. 8.3, Fig. 8.4, Fig. 8.5, and Table 8.1). An additional boulder OV-GPS-01 indicates movement in the three-dimensional space only since no horizontal movement can be distinguished from the uncertainty (Table 8.1). Not surprisingly, the most movement was determined between 2010-2017, and 2011-2017, which are the two longest time intervals. The only movement between 2010-2011 occurs for boulder OV-GPS-03 and recorded in the horizontal plane only.

The young drift appears dynamic and exhibits surface movement (Fig. 8.3, Fig. 8.4, Fig. 8.5, and Table 8.1). The two boulders OV-GPS-06 and OV-GPS-07, located on the young drift, show distinct movement of 5.78 +/- 0.91 cm and 4.85 +/- 2.91 cm between the longest time interval 2010-2017. The direction of movement is generally NNW, towards down valley (Fig. 8.3). In three-dimensional space, the uncertainty has increased >3 cm, resulting in a greater but less distinct movement for OV-GPS-07 (2010-2017; 7.73 +/- 7.20 cm and 2011-2017; 5.63 ± 7.89 cm), caused by the increased uncertainty in the vertical direction when measuring GNSS positioning.

The middle drift shows a less definite movement in the surface boulders. Boulder OV-GPS-02 is located on the highest area of the middle drift and displays no movement to a position accuracy of < 1 cm. Boulder OV-GPS-01 and OV-GPS-03 are positioned on either side of the highpoint (up- and down valley, respectively), and both indicate movement (Fig. 8.3 and Table 8.1). Further, these two boulders are the only ones that display a vertical movement greater than the combined vertical uncertainty from 2011-2017 (Fig. 8.5). The vertical movement for boulder OV-GPS-01 and OV-GPS-03 is 1.94 +/- 1.38 cm and 2.57 + 1.86 cm, respectively, in an upward direction. In addition, OV-GPS-03 shows horizontal movement in the NW direction and a maximum distance of 2.69 ± 1.86 cm in three-dimensional space (Table 8.1).

None of the boulders on the old drift surface (OV-GPS-04 and OV-GPS-05) show movement. However, boulder OV-GPS-08 located at the boundary between the middle and old drift indicates a movement of 0.96 ± 0.78 cm and 1.68 ± 1.50 cm in the horizontal and three-dimensional space, respectively. The direction of movement is towards WNW (Fig. 8.3 and Fig. 8.4). It should be noted that no GNSS data was available for 2010, and therefore only movement analysis from the period 2011-2017 exists.

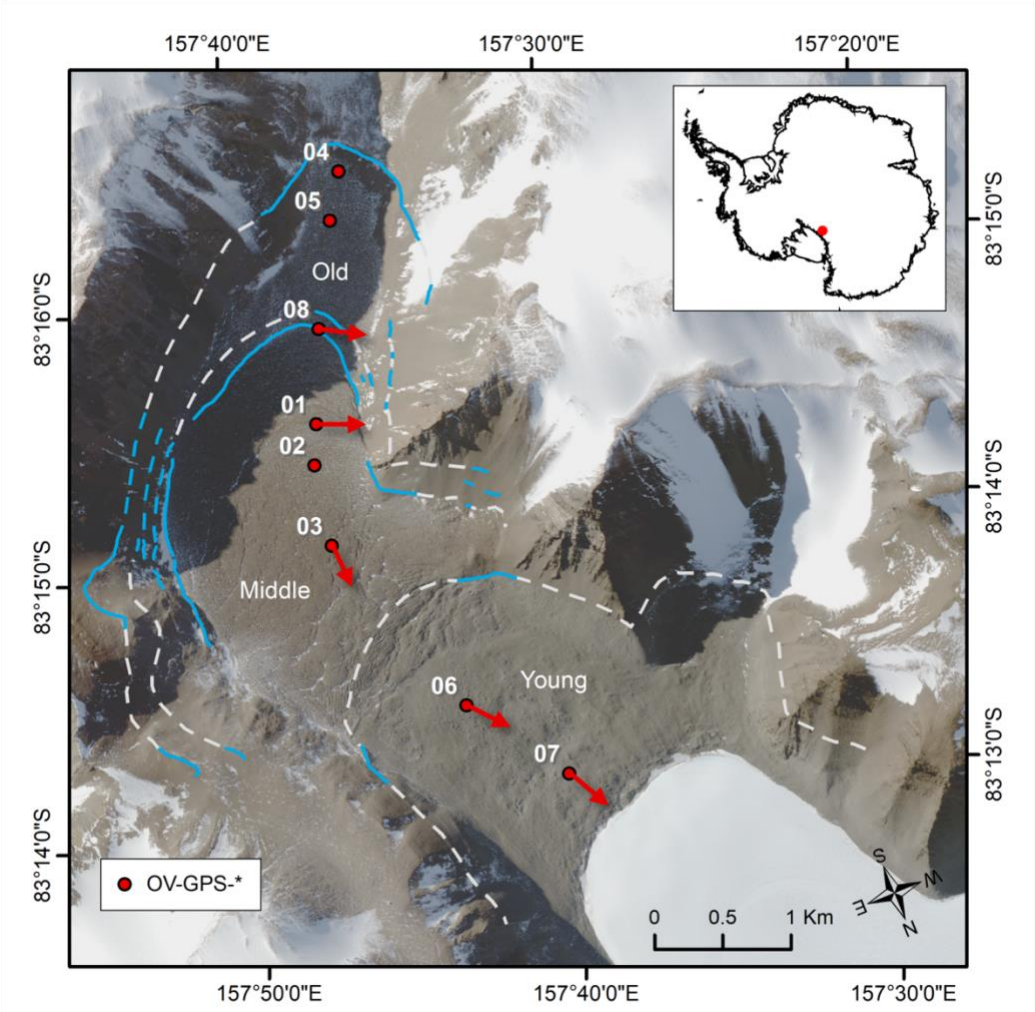

Figure 8.3 Directional movement of surface boulder in Ong Valley, Antarctica (WV2 satellite image © 2016 Maxar). Red arrows indicate the average direction of movement for the period 2010-2017 and 2011-2017. Note: the arrows only show the direction but not the magnitude of movement. Lines indicate lateral and end moraines mapped from traverses (blue solid line), elevation laser measurements (blue dashed line), and inferred from continuously tracing the moraines (white dashed line).

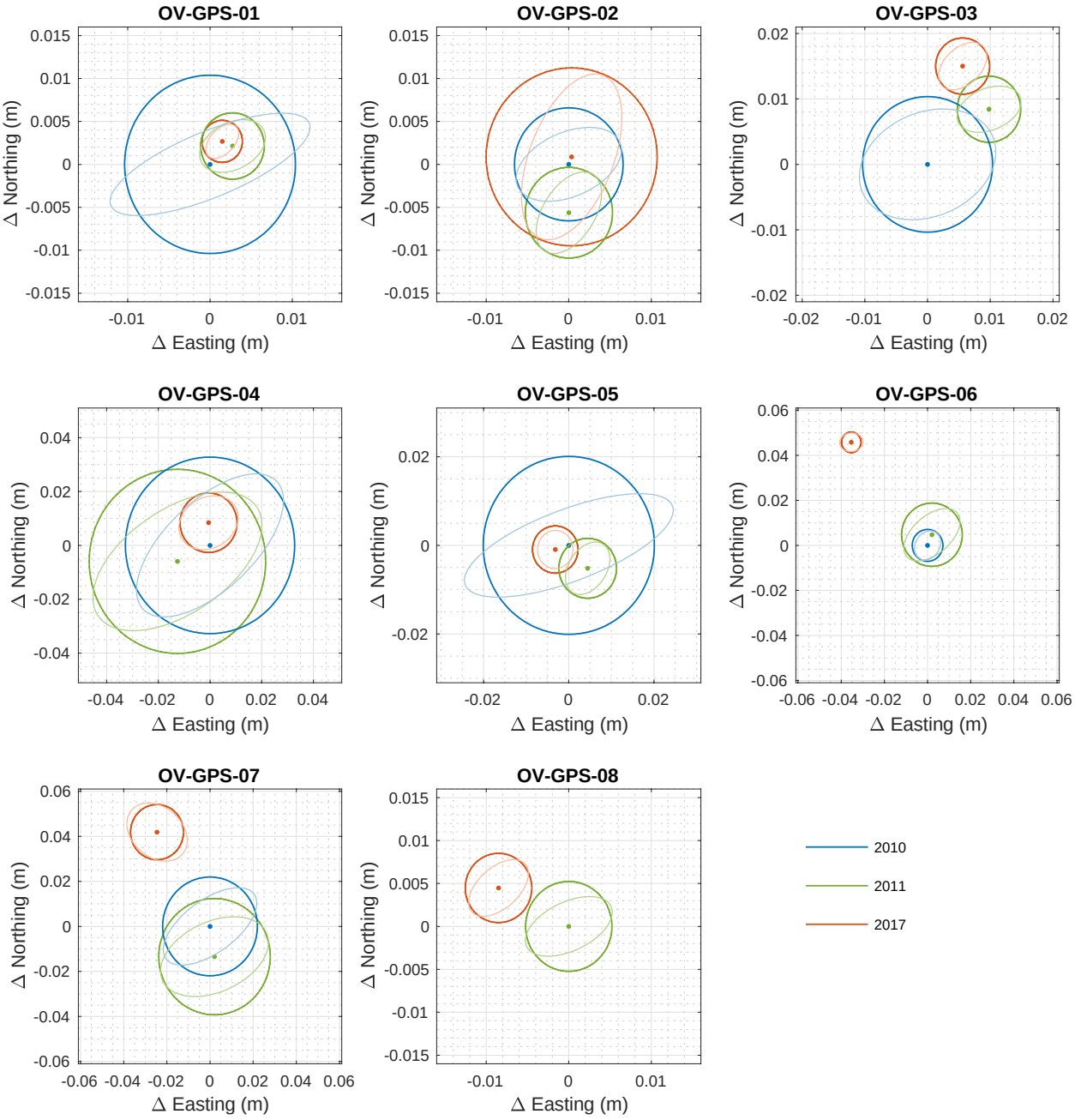

Figure 8.4 Horizontal boulder GNSS positions. An initial zero position is assigned to the 2010 boulder location, with 2011 and 2017 being the position relative to the initial point. Thick line represents the 95% error circle with a radius being the horizontal precision. Thin line represents the 95% error ellipse.

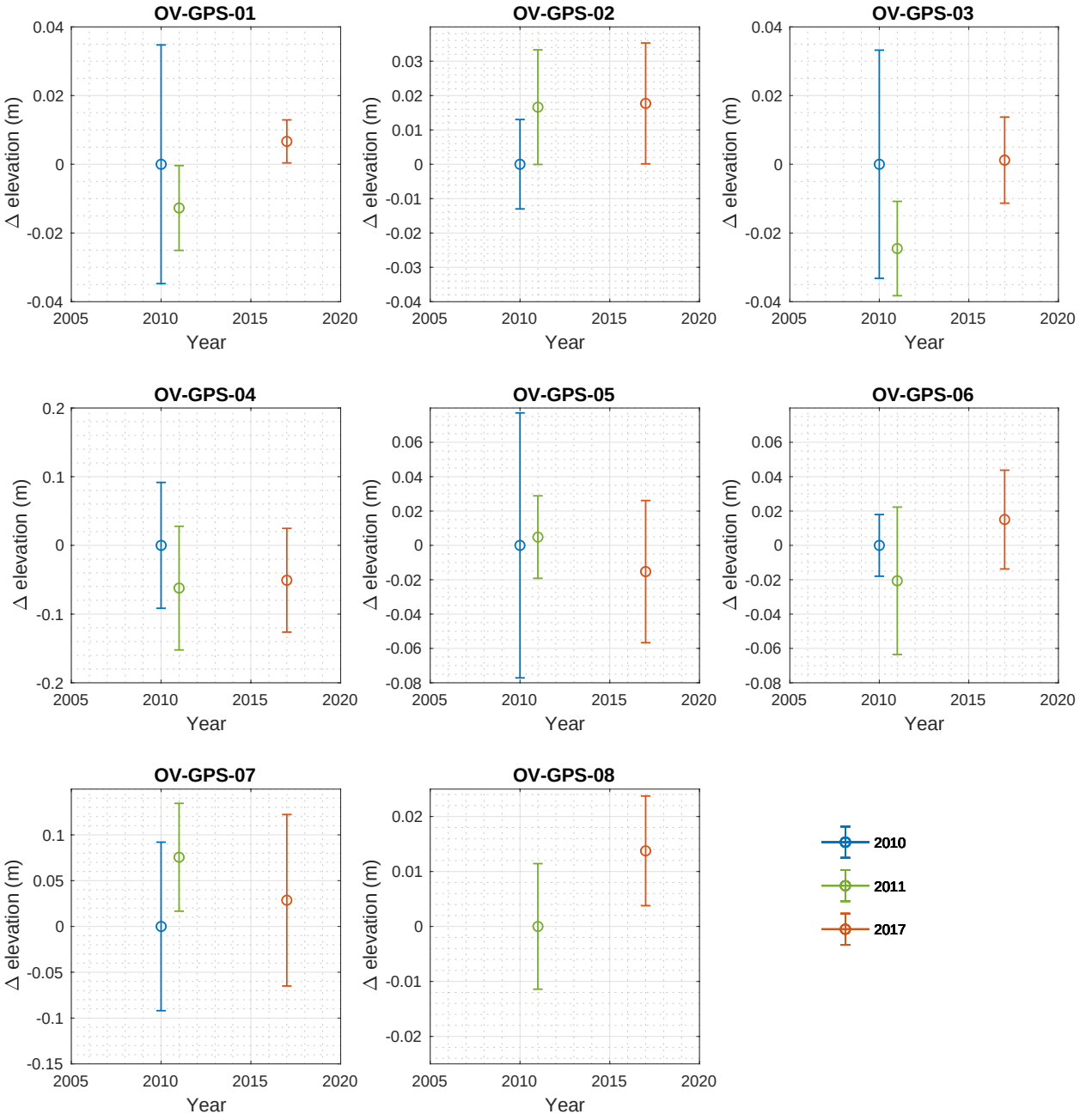

Figure 8.5 Vertical Boulder GNSS positions. An initial zero position is assigned to the 2010 boulder location, with 2011 and 2017 being the elevation relative to the initial point.

Table 8.1 Boulder movement results. The distances are reported for both horizontal and three-dimensional space, including the azimuth direction (Az.) and degrees from horizontal (From h.) representing the degree move in either upward (positive) or downward (negative) direction, where zero indicate only horizontal movement. Bold values indicate distance that are greater than the 95% uncertainty and where movement is considered.

		2010 - 2011				**2011 - 2017**				**2010 - 2017**			
Drift	Boulder OV-GPS-*	Horizontal distance (cm)	3D distance (cm)	Az. (deg.)	From h. (deg.)	Horizontal distance (cm)	3D distance (cm)	Az. (deg.)	From h. (deg.)	Horizontal distance (cm)	3D distance (cm)	Az. (deg.)	From h. (deg.)
Old	04	1.39 ± 5.68	6.37 ± 13.18	245	-77	1.87 ± 4.38	2.2 ± 8.27	40	31	0.84 ± 3.59	5.15 ± 11.95	356	-81
	05	0.68 ± 2.71	0.83 ± 6.58	139	35	0.87 ± 0.94	2.19 ± 4.49	299	-67	0.33 ± 2.41	1.56 ± 8.96	254	-78
	08	-	-	-	-	**0.96 ± 0.78**	**1.68 ± 1.50**	**298**	**55**	-	-	-	-
Middle	01	0.35 ± 1.43	1.32 ± 3.87	52	-75	0.14 ± 0.51	**1.94 ± 1.39**	**293**	**86**	0.31 ± 1.35	0.73 ± 3.67	29	65
	02	0.56 ± 0.84	1.76 ± 2.11	180	71	0.65 ± 1.19	0.66 ± 1.41	3	9	0.09 ± 1.4	1.77 ± 2.22	22	87
	03	**1.29 ± 1.28**	2.77 ± 3.46	**49**	-62	**0.78 ± 0.77**	**2.69 ± 1.86**	**327**	**73**	**1.6 ± 1.21**	**1.61 ± 1.32**	**20**	**4**
Young	06	0.51 ± 1.81	2.13 ± 4.71	23	-76	**5.55 ± 1.78**	**6.6 ± 3.75**	**318**	**33**	**5.78 ± 0.91**	**5.97 ± 1.25**	**322**	**15**
	07	1.36 ± 3.62	7.67 ± 11.04	171	80	**6.14 ± 3.12**	**7.73 ± 7.20**	**334**	**-37**	**4.85 ± 2.91**	5.63 ± 7.89	**330**	31

8.3 Cosmogenic Nuclide Results

We measured concentrations of cosmogenic nuclides in i) pit samples from unconsolidated supraglacial debris, ii) ice core taken directly underlying the pit samples, and iii) erratic boulders from the middle drift surface and moraines. Here we report the measured nuclide concentrations and in subsequent sections we apply a forward model aimed to explain the nuclide data set.

8.3.1 Ice Core Visual Observations

Visual inspection of the ice core indicate that it is primarily composed of debris-rich ice containing poorly sorted sediment ranging from clay to clasts exceeding the diameter of the borehole (Fig. 7.8). Bands of clean ice (lacking debris) were observed with a thickness < 0.5 m. Sections of the debris-rich ice show distinct debris bands with a thickness of a few centimeters. The orientation of these debris bands is variable but commonly steeply dipping.

8.3.2 Measured Ice Core Nuclide Concentrations

We measured cosmogenic nuclide ^{10}Be, ^{21}Ne, and ^{26}Al in 6 supraglacial debris pit samples (17-OD1-PIT2*) and 12 ice core samples (17-OD1-C1*). In addition, ^{21}Ne was measured for the surface sample (17-OD1-surf). The results show that cosmogenic nuclide concentrations in the englacial debris show large downcore variations (Table 8.2). The relative magnitude of the variation is larger for ^{10}Be and ^{21}Ne than for ^{26}Al, which indicates that the amount of time that has

elapsed since ice emplacement is most likely on the order of several half-lives of ^{26}Al (the ^{26}Al half-life is 0.7 Ma).

Table 8.2 Measured cosmogenic nuclide concentrations in quartz extracted from supraglacial debris (prefix 17-OD1-surf/PIT2*) and ice core (prefix 17-OD1-C1*).

Sample ID	Top depth (cm)	bottom depth (cm)	Top Mass Depth (g cm^{-2})	Bottom Mass Depth (g cm^{-2})	^{10}Be x 10^6 (atoms g$^{-1}_{qtz}$)	^{21}Ne x 10^6 (atoms g$^{-1}_{qtz}$)	^{26}Al x 10^6 (atoms g$^{-1}_{qtz}$)
17-OD1-surf	0	1				130.6 ± 7.3	
17-OD1-PIT2-6-14	6	14	11.4	25.8	13.431 ± 0.084	109.1 ± 6.2	67.8 ± 1.2
17-OD1-PIT2-14-17	14	17	25.8	31.1	13.512 ± 0.085	102.1 ± 4.6	67.3 ± 1.4
17-OD1-PIT2-23-29	23	29	41.8	52.5	12.866 ± 0.080	104.9 ± 5.8	63.4 ± 1.3
17-OD1-PIT2-37-43	37	43	66.7	77.4	11.593 ± 0.070	91.7 ± 4.3	58.2 ± 1.2
17-OD1-PIT2-43-50	43	50	77.4	89.6	6.639 ± 0.059	55.2 ± 2.8	35.59 ± 0.74
17-OD1-PIT2-56-62	56	62	99.9	110.2	4.246 ± 0.052	34.6 ± 2.5	23.32 ± 0.53
17-OD1-C1-5-36	67	98	114.7	145.4	0.709 ± 0.020	11.4 ± 1.5	4.43 ± 0.21
17-OD1-C1-36-48	98	110	145.4	158.2	0.573 ± 0.014	12.2 ± 1.1	3.44 ± 0.15
17-OD1-C1-48-70	110	132	158.2	180.5	0.573 ± 0.013	13.3 ± 2.9	2.97 ± 0.15
17-OD1-C1-70-100	132	162	180.5	216.9	1.459 ± 0.030	39.9 ± 1.1	4.22 ± 0.22
17-OD1-C1-107-125	169	187	223.3	248.3	1.096 ± 0.010	37.3 ± 5.8	3.331 ± 0.086
17-OD1-C1-125-145	187	207	248.3	269.9	0.871 ± 0.017	30.4 ± 2.5	2.83 ± 0.10
17-OD1-C1-185-235	247	297	306.6	354.7	0.288 ± 0.010	14.0 ± 2.8	1.48 ± 0.12
17-OD1-C1-235-310	297	372	354.7	426.9	0.1603 ± 0.0090	6.4 ± 1.4	1.17 ± 0.10
17-OD1-C1-310-350	372	412	426.9	468.7	0.1161 ± 0.0048	9.2 ± 5.7	0.831 ± 0.055
17-OD1-C1-500-582	562	644	607.0	694.5	0.1479 ± 0.0041	21.2 ± 1.0	0.450 ± 0.040
17-OD1-C1-582-649	644	711	694.5	774.6	0.1323 ± 0.0032	28.3 ± 7.4	0.409 ± 0.032
17-OD1-C1-781-819	843	881	895.8	938.1	0.4184 ± 0.0081	52.6 ± 4.1	0.489 ± 0.034
17-OD1-C1-819-879	881	941	938.1	1001.2	0.516 ± 0.010	64.5 ± 4.1	0.49 ± 0.031
17-OD1-C1-879-944	941	1006	1001.2	1071.7	0.4816 ± 0.0091	67.0 ± 2.4	0.471 ± 0.038

8.3.3 Boulder Surface Exposure Results

We measured cosmogenic nuclide ^{10}Be and ^{21}Ne in quartz from erratic boulders from the middle drift surface and east lateral moraine (Fig. 5.2). Apparent ^{10}Be and ^{21}Ne exposure ages for the middle drift surface boulder samples are 1.55-2.16 Myrs and 0.82-1.39 Myrs for the East lateral moraine boulders (Table 8.3). Further, the apparent ^{10}Be exposure ages reported for all boulder samples appear younger than of those from ^{21}Ne, and is an indication that some process (e.g., erosion, burial, etc.) must have occurred which decreases the ^{10}Be nuclide concentration relative to ^{21}Ne.

Table 8.3 Exposure-age data for boulders on the surface of Ong Valley middle drift and correlative lateral moraines.

Sample name	Latitude (DD)	Longitude (DD)	Elevation (m)	Sample thickness (cm)	Shielding factor	[^{10}Be] (Matoms g^{-1})	Apparent ^{10}Be exposure age (Ma)	Excess [^{21}Ne] (Matoms g^{-1})	Apparent ^{21}Ne exposure age (Ma)
Boulders on drift surface in valley center									
11-OV-ER-117	-83.25658	157.70622	1601	2	0.9916	25.15 ± 0.43	1.546 ± 0.039 (0.143)	206.2 ± 7.0	2.157 ± 0.082 (0.157)
11-OV-ER-118	-83.25478	157.71861	1610	3.5	0.9950	27.49 ± 0.46	1.778 ± 0.048 (0.176)	191.7 ± 5.8	2.002 ± 0.071 (0.143)
(Replicate ^{21}Ne measurement)								195.6 ± 5.8	2.044 ± 0.071 (0.145)
11-OV-ER-119	-83.25237	157.74124	1597	1.5	0.9929	28.28 ± 0.45	1.854 ± 0.049 (0.187)	181.4 ± 5.5	1.885 ± 0.068 (0.135)
Boulders on lateral moraine correlative with middle drift on east side of valley									
17-OV-212-ERR	-83.24582	157.7961	1715	1.5	0.9909	19.09 ± 0.14	0.9280 ± 0.0088 (0.070)	120.8 ± 5.3	1.093 ± 0.059 (0.090)
17-OV-213-ERR	-83.24529	157.79558	1718	2	0.9909	18.48 ± 0.23	0.892 ± 0.014 (0.068)	106.3 ± 4.6	0.955 ± 0.053 (0.080)
17-OV-214-ERR	-83.24472	157.79579	1714	6	0.9909	18.54 ± 0.23	0.936 ± 0.015 (0.072)	129.0 ± 6.7	1.215 ± 0.073 (0.105)
17-OV-215-ERR	-83.24336	157.79526	1733	2.5	0.9909	17.42 ± 0.14	0.8205 ± 0.0080 (0.060)	99.1 ± 3.9	0.873 ± 0.047 (0.071)
17-OV-217-ERR	-83.24301	157.79561	1715	3.5	0.9918	18.11 ± 0.19	0.885 ± 0.012 (0.067)	138.3 ± 5.2	1.271 ± 0.058 (0.098)
17-OV-218-ERR	-83.24453	157.79491	1722	1.5	0.9918	19.63 ± 0.18	0.954 ± 0.011 (0.073)	154.2 ± 5.8	1.394 ± 0.062 (0.106)

Notes:

1. Rock density is assumed to be 2.57 g cm^{-3} based on measurements on like lithologies in Ong Valley.

2. Exposure ages are calculated using default production rates and 'LSDn' scaling in version 3 of the online exposure age calculator described by Balco et al. (2008) and subsequently updated.

3. Both internal (including only measurement uncertainty) and external (in parentheses; also includes production rate uncertainty) uncertainties are shown for apparent exposure ages.

4. ^{21}Ne exposure age calculations include subtraction of 7 ± 3 Matoms/g non-cosmogenic ^{21}Ne (see text).

8.4 Model Fitting

In the following sections we first highlight several important features of the measured cosmogenic nuclide data from the ice core and supraglacial debris that we seek to explain using the forward model for nuclide accumulation described in previous sections. We then fit the forward model to the observations and thereby obtain estimates for the emplacement age and sublimation rate of the buried ice. Lastly, we calculate a minimum age for the middle drift in Ong Valley.

8.4.1 Qualitative Observations of the Ice Core Data

The forward model described in sect. 7.2.3 is an exposure model that is based on an assumption that the englacial debris is well mixed and therefore all the samples contain the same amount of inherited nuclides. The model calculates the postdepositional nuclide production during the exposure (Eq. 34 and 35). This is compatible with an ice mass that is emplaced during a single glacial advance. After a single event of exposure, where sublimation and erosion has occurred, the concentration for a given cosmogenic nuclide in the englacial debris must decrease monotonically with depth as the production rate decreases with increased shielding mass.

However, multiple sections of the ice core show increase in cosmogenic nuclide concentration at depth (Table 8.2) and is therefore not compatible with a single exposure history described above. The most likely explanation for the observed increases in cosmogenic nuclide concentrations with depth in OD1 samples, is that englacial debris in various sections of the core have variable exposure histories prior to entrainment in the ice, and therefore have different

inherited nuclide concentrations. Based on the measured nuclide concentrations we make the following two observations that guide our forward modeling.

The first observation is that the set of samples that display monotonically decreasing nuclide concentrations (Fig. 8.6. Sections S1, E1 and E2) are segments of the ice core with relatively low debris concentrations. These samples follow the expectation of having an exposure history as outlined in the forward model. We define these samples to be of a low-nuclide concentration that is largely composed of subglacially derived material sourced from upstream of the Argosy Glacier and have minimal surface exposure prior to entrainment. The debris from such samples is therefore identified to be of 'englacial debris' (samples denoted englacial E1 and E2 and highlighted in blue in Fig. 8.6) including the current surface debris layer (S1) that we assume has also originated from englacial debris.

The second observation is that the debris-rich sections of the ice core (Fig. 8.6a. Sections S2, S3, and S4) have much higher nuclide concentrations and do not conform to the assumptions of a well-mixed ice mass containing subglacially derived debris and only experiencing *in situ* englacial accumulation of cosmogenic nuclides. We consider the debris in these sections to be from one or more high-concentration sources that are likely composed of material that was exposed for an extended period of time on the surface and entrained as the glacier overrode previously ice-free areas as it advanced into Ong Valley. In fact, these samples have ^{21}Ne concentrations similar to modern surface material (S1), and therefore must have been exposed for millions of years at or near surface. Therefore, debris from these subsurface samples having higher nuclide concentrations are identified as 'paleo surfaces' and is observed in three distinct units. Although

these units must all contain some fraction of recycled surface debris, this may be of variable origin, so we identify these as S2, S3, and S4 (highlighted in shades of red in Fig. 8.6). In this paper we refer to this debris as recycled paleo surface.

Based on the above observations we can only explain a subset of the data with the forward model. However, the presence of significant and variable inheritance in the debris from different sources suggests that we can apply a burial constraint to the inherited nuclide inventory having prior exposure. When fitting the model to the postdepositional nuclide inventory, this allows for an additional constraint on the age of ice emplacement.

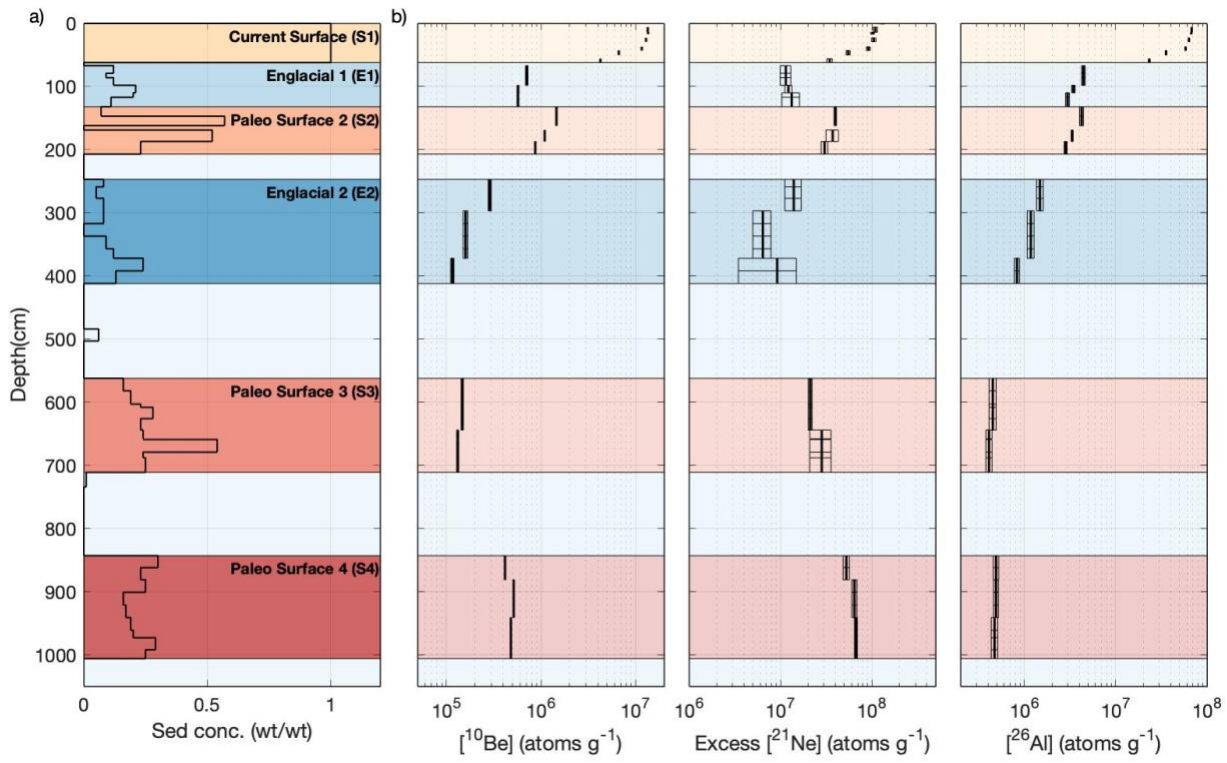

Figure 8.6 Depth plot of (a) sediment concentration (weight sediment/weight total sample) and (b) measured 10Be, 26Al, and 21Ne nuclide concentrations. Color shades highlight the source of the debris. Yellow are current supraglacial debris samples (S1) and has same origin as blue samples (E1 and E2) identified as 'englacial debris' having no prior surface exposure before being subglacially entrained. Samples in shades of red is identified as 'paleo surfaces' (S2, S3, and S4) and to be of recycled surface debris that was exposed on the surface and entrained as the glacier overrode previously ice-free areas as it advanced into Ong Valley.

8.4.2 Forward Modeling Used to Explain the Data Set

The forward model predicts the accumulation of cosmogenic nuclides ^{10}Be, ^{26}Al, and ^{21}Ne in the ice core and the overlaying supraglacial debris during a single event of exposure, constrained by following rates: sublimation of ice, surface erosion, and accumulation of supraglacial debris (Eq. 34 and Eq. 35). If we assume constant inheritance in the englacial debris, it is only possible to fit the model to the set of samples that show monotonically decreasing nuclide concentrations with depth. The model is therefore fitted to; i) surface sample in which only ^{21}Ne measurement is available, ii) all measured nuclide samples in the supraglacial debris, S1, and iii) samples of englacial debris, units E1 and E2.

While the recycled paleo surfaces S2, S3, and S4 are not included in the fitting of the forward model, they are utilized for burial-dating to further constrain the age of ice emplacement. The general idea for applying burial-dating to the recycled paleo surface samples is following. The high cosmogenic nuclide concentrations in the recycled paleo surfaces are the result of extended period of exposure of the debris prior to entrainment in the middle ice. The debris in these samples was part of a surface that was overridden during the latest advance of glacial ice into Ong Valley. Hence, this paleo surface debris must have been buried at the time the middle ice was deposited. The burial age obtained from burial-dating of the debris from these recycled paleo surface samples, should then reflect the timing of the middle ice emplacement. Further, the burial age of these samples cannot display ages that are younger than the event at which they got buried. Therefore, the minimum burial age for any of the recycled paleo surface sections (S2-4) serves as the maximum age for when the middle ice was emplaced in Ong Valley.

Burial-dating of the recycled paleo surfaces is applied to their inherited nuclide concentrations. The inherited nuclide concentration is calculated by subtracting the modeled post-emplacement nuclide concentrations from the total measured nuclide concentrations. The apparent burial age of the recycled paleo surface debris is then determined from the nuclide ratio of the calculated inherited nuclide concentrations. The apparent burial age is the duration of burial inferred from a pair of nuclide measurements under the assumption that a sample has experienced a single period of exposure followed by a single period of burial. In reality, the sample could have experienced multiple shorter periods of burial; however, the calculated apparent burial age is the maximum single period a sample has been buried for. The age of ice emplacement for the middle ice is then limited by the minimum apparent burial age for any of the recycled paleo surface samples S2-4. This constraint is incorporated into the model fitting such that when adding the nuclide concentrations lost by decay during burial, the nuclide ratio does not exceed that of the surface exposure production ratio. This burial constraint is applied only to the samples that are not used for forward model fitting, and that make up the recycled surface material S2, S3, and S4.

8.4.3 Model Results

By fitting the forward model prediction to measured nuclide concentrations from the englacial debris sample (S1, E1 and E2) and applying burial constraint to sections of recycled paleo surface debris (S2, S3 and S4), we are able to constrain the age of ice emplacement, sublimation rate, and surface erosion rate for Ong Valley middle ice. The results of a 10,000-iteration Monte Carlo simulation provide an ice emplacement age of 2.95 +0.18/-0.22 Myrs for the middle ice, with a best-fit, χ^2 of 3.75 +0.98/-0.45. The best-fitting sublimation rate since

emplacement is 22.86 +0.10/-0.09 m Myr^{-1}, with a surface erosion rate of 0.206 +0.013/-0.017 m Myr^{-1}. The results of the simulation are not normally distributed, and the best-fit values are therefore reported as the 50^{th} percentile with error bounds given by the 16^{th} and 84^{th} percentile (Fig. 8.7 and Fig. 8.8). The inherited nuclide concentration for ^{10}Be, ^{21}Ne, and ^{26}Al (the initial nuclide concentration present in the ice mass at the time of deposition 2.95 Ma ago) is 0.101 +0.018/-0.017 x 10^6 atoms g^{-1}, 9.2 +1.4/-4.4 x 10^6 atoms g^{-1}, and 0.8249 +0.0062/-0.0031 x 10^6 atoms g^{-1}, respectively.

The measured debris concentrations in the ice segments range between 0 for clean ice and 0.57 for debris-rich ice, with an average of 0.13 by weight for the core. The average debris concentration for the best fit in the sublimated ice which produced the supraglacial debris over a period of 2.95 Ma is 0.036-0.034 by weight, and therefore an average ice-debris density of 0.9313 g cm^{-3}. Further, the resulting sublimation rate of 22.86 m Myr^{-1} over the span of 2.95 Ma, results in a total ice surface lowering of 67.6 m.

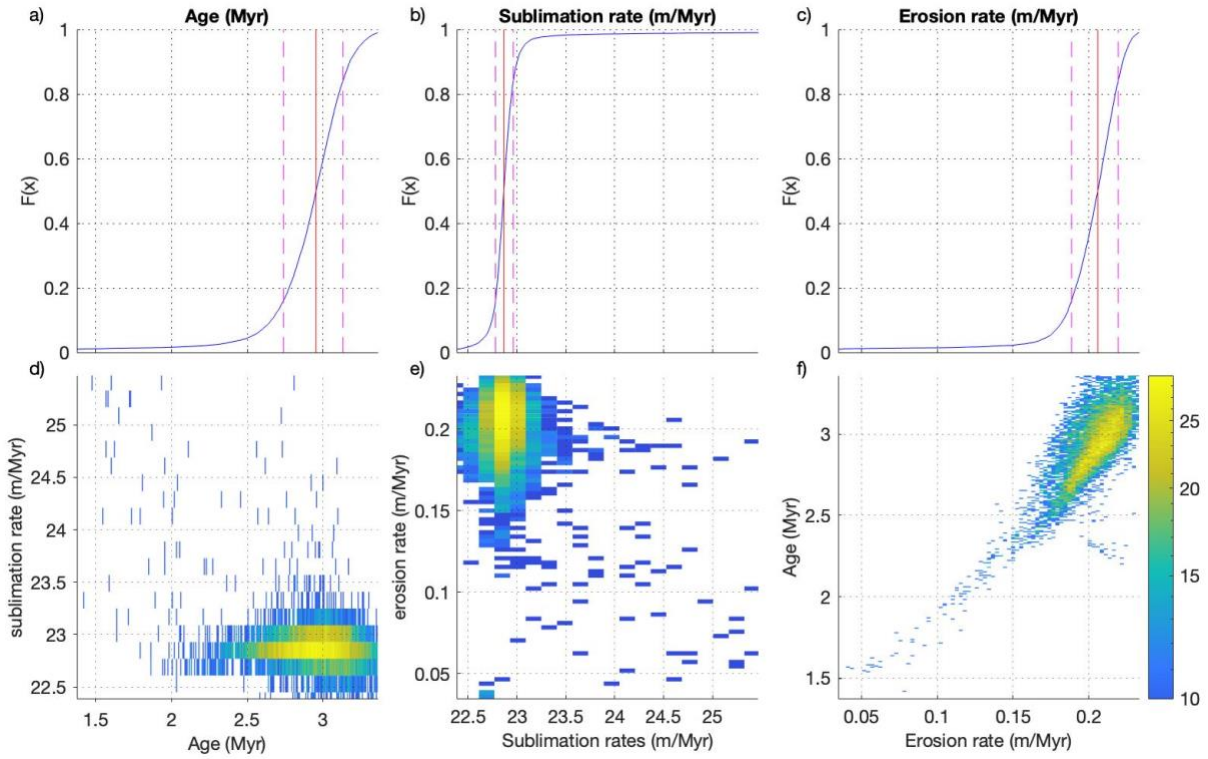

Figure 8.7 (a-c) Cumulative distribution of 10,000 fitted Monte Carlo simulation results showing the 50th percentile (red line) with error bounds given by the 16th and 84th (pink lines). (f-e) Density plot as paired distribution of Monte Carlo simulation results separated into 1000 bins with yellow being high density and blue low density. Both the vertical and horizontal axes (d-f) are truncated to the 98% (0.01 and 0.99) confidence interval.

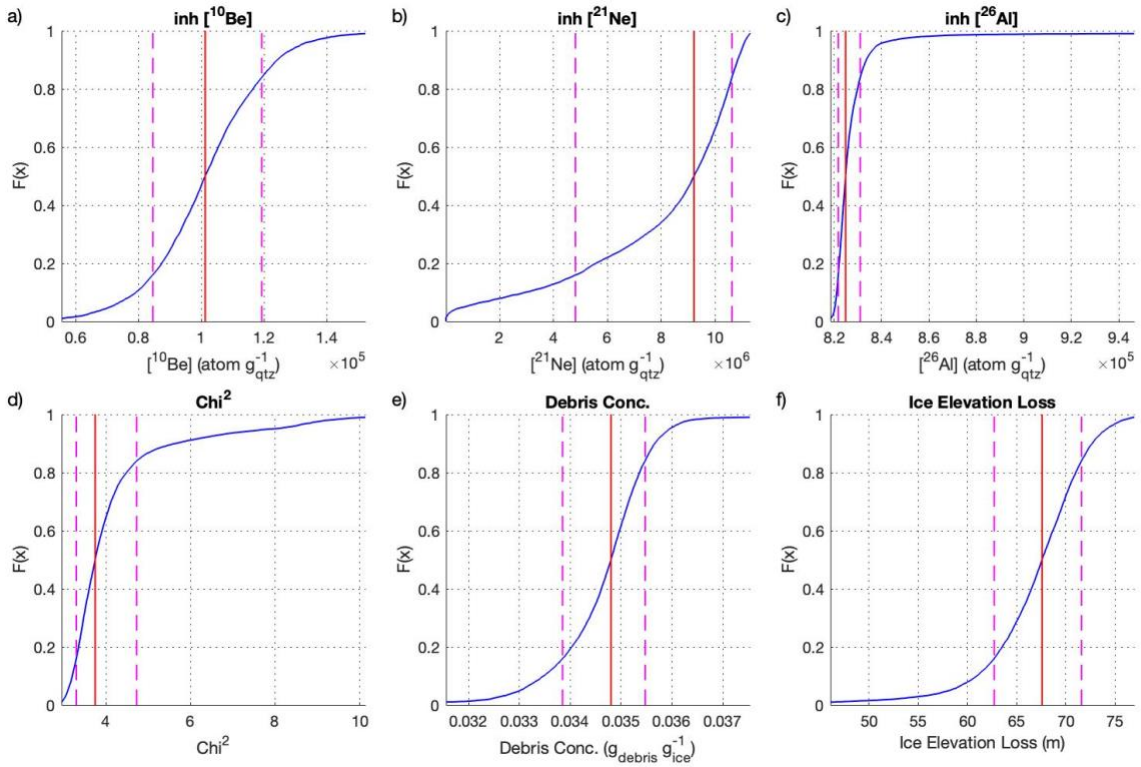

Figure 8.8 Cumulative distribution of 10,000 fitted Monte Carlo simulation results for the inherited nuclide concentration (a) ^{10}Be, (b) Ne, and (c) Al, (d) the fitted Chi^2 value for each Monte Carlo iteration, (e) debris concentration by weight in the sublimated ice mass, and (f) the ice mass elevation loss. Also showing is the 50th percentile (red line) with error bounds given by the 16th and 84th (pink lines), and the horizontal axes are truncated to the 98% (0.01 and 0.99) confidence interval.

The model predicts nuclide concentrations at depth similar to those measured in the supraglacial debris (S1) and englacial debris (E1-2) and it is therefore evident that these units can be explained with the exposure model (Fig. 8.9a-c). Further, the paired-nuclide plot (Fig. 8.9d-f) clearly shows the distinction between the englacial debris data set (S1, E1-2) explainable by the model and the paleo surface samples (S2-4) having high nuclide concentrations and low paired-nuclide ratio, hence, different origin which require the addition of a complex burial and exposure history.

Conceptually, higher nuclide concentrations require long surface exposure and any disequilibrium in the paired-nuclide ratio (ratio below the steady-state-erosion zone) is the effect of burial after exposure (Lal, 1991). However, the presence of a significant inherited nuclide inventory could result in surface and subsurface samples having ratios below the production ratio and therefore indicating an apparent burial age. In Fig. 8.9d-f this is observed as both the predicted and all measured nuclide concentration ratios fall within the burial zone, and not near the steady-state-erosion zone.

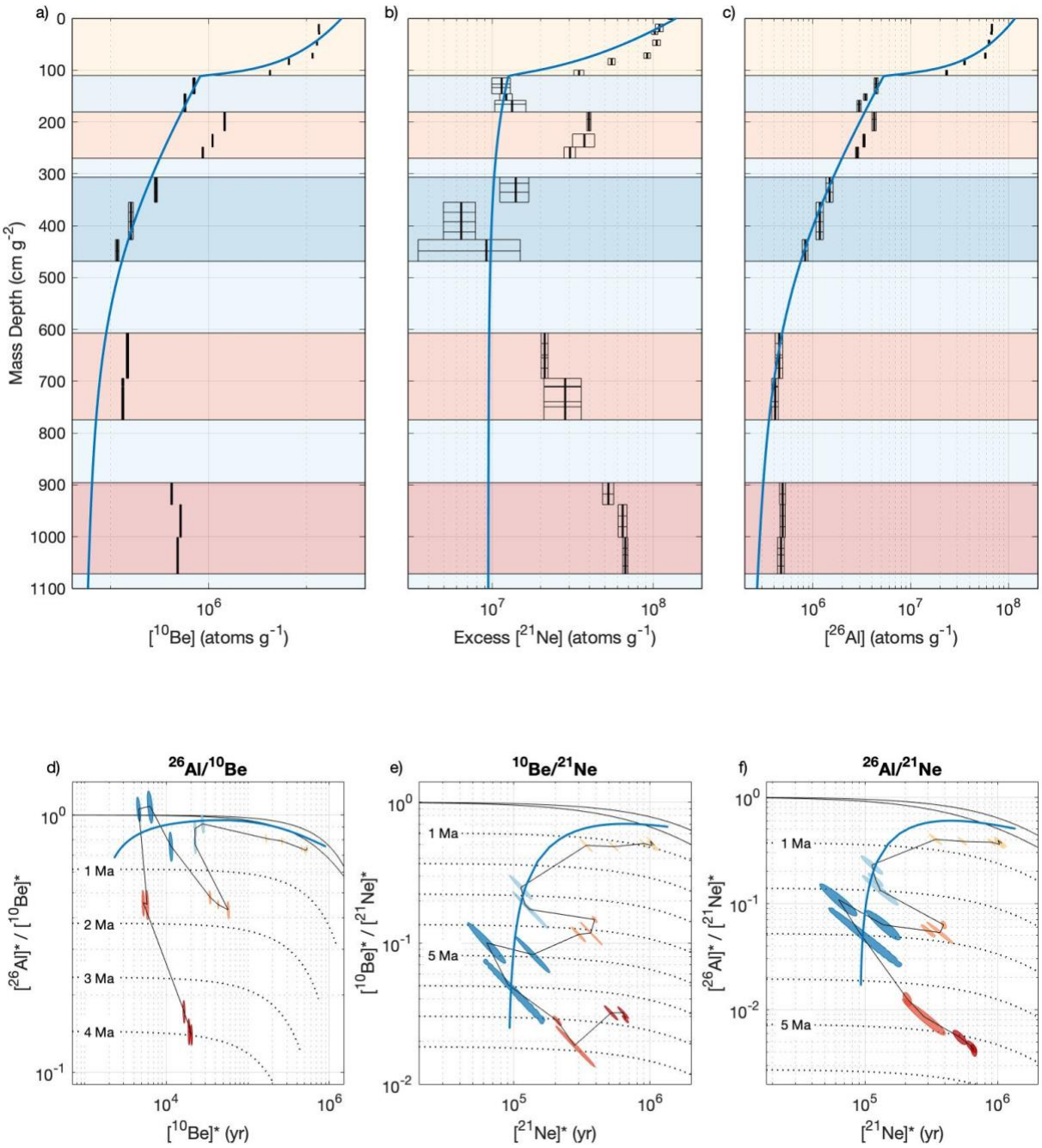

Figure 8.9 Measured and modeled cosmogenic nuclide concentrations as (a-c) mass depth below the surface for (a) ^{10}Be, (b) ^{21}Ne, and (c) ^{26}Al, and (d-f) paired-nuclide exposure-burial diagram for (d) ^{26}Al-^{10}Be, (e) ^{10}Be-^{21}Ne, and (f) ^{26}Al-^{21}Ne pairs. Blue lines indicate the model predicted cosmogenic nuclide concentration from the pit surface to the bottom of the ice core. Colored boxes (a-c) and sample colors (d-f) indicate debris source as detailed in Fig. 8.6. In (d-f), solid black lines show the steady-state erosion zone, and dashed lines show the burial lines as Million-year decay isochrons (See section 6.5 and Fig. 6.1 for more details). The measured nuclide concentration for each sample is represented by a shaded ellipse of its 1-sigma uncertainty. The black line connects the sample ellipses from the surface of the pit down to the bottom of the ice core. *Nuclide concentrations normalized to respective surface production rate.

8.4.4 Minimum Exposure Age

We find the absolute minimum exposure age of the middle ice to be 1.331 +0.020/-0.024 Ma, with a sublimation rate of 24.70 +0.71/-0.56 m Myr^{-1}. This age is derived from the minimum possible number of assumptions about the geologic history of the samples. For a surface sample, the apparent age is the calculated age from the measured nuclide concentration assuming a sample has experienced a single event of exposure, zero surface erosion, and no burial during that time period. Under such assumptions, a surface sample's apparent exposure age serves as the minimum exposure age. Therefore, the minimum age for the ice emplacement is obtained using the assumption that the inherited nuclide concentration for ^{10}Be, ^{21}Ne, and ^{26}Al is equal to the minimum concentrations measured throughout the core (0.12×10^6 atoms g^{-1}, 6.42×10^6 atoms g^{-1}, and 0.41×10^6 atoms g^{-1}, respectively) with zero surface erosion.

8.4.5 Burial Dating of Paleo Surface Debris

As evident in Fig. 8.9, the paleo surface samples have elevated nuclide concentrations and do not fit our modeled predictions. There is no scenario in which these samples can be explained solely by our forward exposure model which includes only sublimation and erosion. Therefore, these samples must have experienced significant periods of surface exposure prior to subglacial entrainment. Further, in order to have a lower paired-nuclide ratio than predicted (Fig. 8.9d-f), the samples must have experienced at least one period of burial. Hence, these observations were the reasons for the inclusion of burial-dating in our model.

Similar to the burial-dating constraint added to the forward model (sect. 8.4.2), we can determine the burial age of these paleo surface samples by first subtracting modeled postdepositional nuclide concentrations at the sample depths from the measured concentrations. This yields an estimate of the nuclide concentrations present in the paleo surface samples (S2-4) at the time they were buried, less the effect of subsequent radioactive decay. The choice to only fit the model to a subset of samples is based on the assumption that the paleo surface samples have different geological history and thus different nuclide inheritance from that of the englacial debris (E1-2) samples. Therefore, the estimated inherited nuclide concentration for these paleo surfaces obtained from this subtraction is different from the inherited nuclide concentrations inferred from the model fitting. From these inherited nuclide concentrations in the paleo surface samples, we can then solve for the burial age which would cause a sample exposed at the surface (plotting on the simple exposure line) to have paired-nuclide ratios as shown in Fig. 8.9. Uncertainties on the burial ages are derived from the same Monte Carlo simulation used to generate uncertainty estimates for the model parameters.

The burial ages for the three paired-nuclide ratios, $^{26}Al/^{10}Be$, $^{10}Be/^{21}Ne$, and $^{26}Al/^{21}Ne$ for S2 are 3.21 ± 0.20 Myr, 4.20 ± 0.27 Myr, and 3.69 ± 0.21 Myr, respectively. The paleo surface S3 and S4 indicate longer periods of burial, with S3 have burial age of 4.33 ± 1.00 Myr, 7.58 ± 0.61 Myr, and 6.24 ± 1.35 Myr, and S4 has burial ages of 5.06 ± 0.25 Myr, 6.61 ± 0.12 Myr, and 5.78 ± 0.15 Myr, respectively for each of the three nuclide pairs. Figure 8.10 shows the paired nuclide ratios for each of the paleo surfaces as their apparent burial ages.

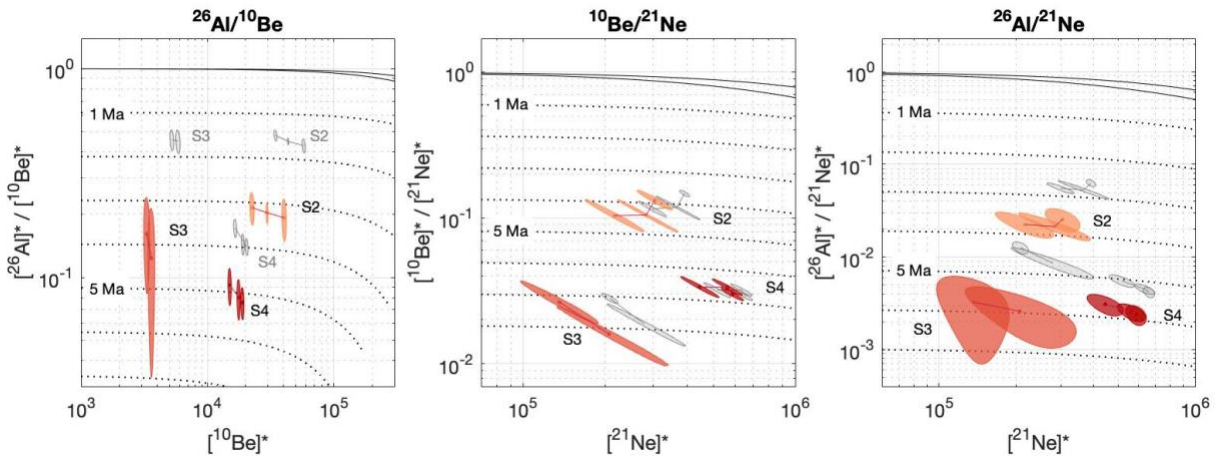

Figure 8.10 Paired-nuclide diagram for (a) ^{26}Al-^{10}Be, (b) ^{10}Be-^{21}Ne, and (c) ^{26}Al-^{21}Ne pairs. Solid black lines show the steady-state erosion zone, and dashed lines show the burial lines as Million-year decay isochrons. The nuclide concentration for each data point is represented by a shaded ellipse of its 1-sigma uncertainty. Grey data points show the measured nuclide concentrations for the paleo surface samples as described in Fig. 8.9. Shaded red data ellipses show the resulting nuclide concentrations when subtracting the modeled nuclide concentration from the measured. The burial age (dashed isochron lines) for which a sample lies represent the apparent burial age and is the maximum single period the sample has been buried since current time. Color shades refer to the different paleo surface units as described in Fig. 8.6. *Nuclide concentrations normalized to respective surface production rate.

CHAPTER 9
DISCUSSION

9.1 Current Stability of the Three Glacial Drifts in Ong Valley

Each of the three drifts in Ong Valley shows varying indications of boulder movements and, therefore, variation in their stability. Movement analysis of surface boulders indicates a dynamic young drift with an average movement of 4.9-7.8 cm between 2010 to 2017 for boulder OV-GPS-06 and OV-GPS-07. We measured a supraglacial debris thickness of 14-26 cm for the young drift near these boulders. From field observations (Fig. 7.3), this would suggest that both boulder OV-GPS-06 and OV-GPS-07 are partially embedded in the ice and frozen in place. Therefore, any movement of the boulders is assumed to be a direct reflection of ice movement. The cause of this movement is speculative. However, from field observations, we find two possible scenarios that could lead to this distinct movement of the young drift surface boulders.

One possible scenario would suggest a stagnant ice mass, in which cryoturbation causes active movement of the supraglacial debris and surface of the buried ice. Thermal contraction of the ice during a cooling phase cause cracks to form in the ice and filled with supraglacial debris. During a warming phase, thermal expansion of the ice causes compressive stresses and produces uplift along the crack. Over time these cracks deepen and expand by the in-filling of supraglacial debris (Sletten et al., 2003). Such cryoturbation leads to polygon formations on the surface with an upward force of the underlying ice. A boulder on the surface of an active polygon can therefore

experience movement caused by cryoturbation. However, the magnitude of movement for supraglacial debris on a polygon is dependent on its developmental stage and is unknown for the drifts in Ong Valley. Further, since the movement is caused by localized upward force of ice movement below the polygon, the direction of movement would be related to the boulder location relative to the polygon's center. However, both boulder OV-GPS-06 and OV-GPS-07 are centered within the polygon, and therefore the direction of movement could be considered coincidental.

A second possible scenario would suggest that the young ice mass below the young drift is retreating and, therefore, not stagnant. Advancement of the Argosy Glacier deposited the young drift during the LGM, 11-13 kyrs ago (Bibby et al., 2016). During deposition, the Argosy Glacier extended 2.3 km further into Ong Valley at an elevation of 120 m higher than current. Since then, retreat and sublimation of the glacier lobe have created a buried ice mass experiencing an elevation difference between the maximum extent of the young drift buried ice and the current exposed glacial ice at the valley mouth (Fig. 8.2). Boulders OV-GPS-06 and OV-GPS-07 both show movement in the NNW direction. This direction coincides with the direction of the pressure gradient towards down valley, cause by a downward surface slope of ~5%. Therefore, the movement of boulder OV-GPS-06 and OV-GPS-07 could be caused by a downward flow of this young, buried ice towards the valley mouth. However, the movement is not considered an average flow rate of the ice. If it were, this would suggest the ice to have moved several km since its deposition 11-13 kyrs ago and disagrees with observations in Ong Valley.

Whether or not the movement of boulders OV-GPS-06 and OV-GPS-07 was caused by flow of the young ice or a shift/tilt in the position of the boulders due to cryoturbation is unclear.

From the available field data, the cause of movement observed in boulders 10-OV-GPS-06 and OV-GPS-07 could be either one of the above scenarios or a combination of the two.

The middle ice is assumed to be stable and stagnant as we find it preserved for ~3 Ma. Such stability is observed in the measured cosmogenic nuclide depth profile and is the primary assumption for cosmogenic nuclide dating of the middle ice. With a supraglacial debris thickness of ~60 cm for the middle drift, all boulders found on the surface of the middle drift are assumed to be completely detached from the buried ice. Boulders OV-GPS-01 and OV-GPS-02 are located near the drill site and are considered the most stable part of the middle drift. The calculated distances between the measured boulder positions are < 1.94 cm. The distance between 2011-2017 for boulder OV-GPS-01 is the only distance greater than the uncertainty of 95% by ~0.55 cm, and therefore an indication of movement.

While the middle drift is considered stable, the presence of desert pavement on the surface of the middle drift polygon formations provides evidence for an active debris surface. In addition, an active surface can also be explained by the partial mixing of the supraglacial debris as observed in the cosmogenic nuclide inventory (see discussion in sect. 9.5). Therefore, it is not surprising that minimal movement could be observed for any boulder from the stable middle drift. From forward modeling of the measured cosmogenic nuclide concentrations, we find a surface erosion rate for the middle drift of ~0.0002 mm yr^{-1}. While such low erosion rates are not detectable within a decadal time scale, it still indicates surface activity. Whether or not a slowly eroding surface or active polygon formations caused this movement or shift in bolt positions is unclear.

In contrast, boulder OV-GPS-03 shows a maximum movement of 1.6 +/- 1.21 cm and 2.69 +/- 1.86 cm for horizontal and three-dimensional movement, respectively. Boulder OV-GPS-03 is located further down valley near a transition zone between the young and the middle drift. From field observations, this zone shows recent disturbance caused by the deposition of the young drift 11-13kyrs. Here, the polygon formations have increased high relief (Fig. 8.2). The surface exhibits larger-scale extensional crevasses perpendicular to the valley direction, with a down-sloping trend toward the Argosy Glacier (Fig. 9.1). During deposition of the young drift into Ong valley, the upwards pushing force of the advancing Argosy Glacier lobe would potentially cause the lower part of the middle drift, the transition zone, to be compressed. Since then, retreat of the Argosy Glacier would cause relaxation and extension of this zone. As discussed above, if the young ice below the young supraglacial debris is active and moving down valley, this could potentially influence the middle ice found in this zone as an elevation difference is created from a recently (11-13 kyrs) retreating glacial deposit, causing a downward gravitational pull.

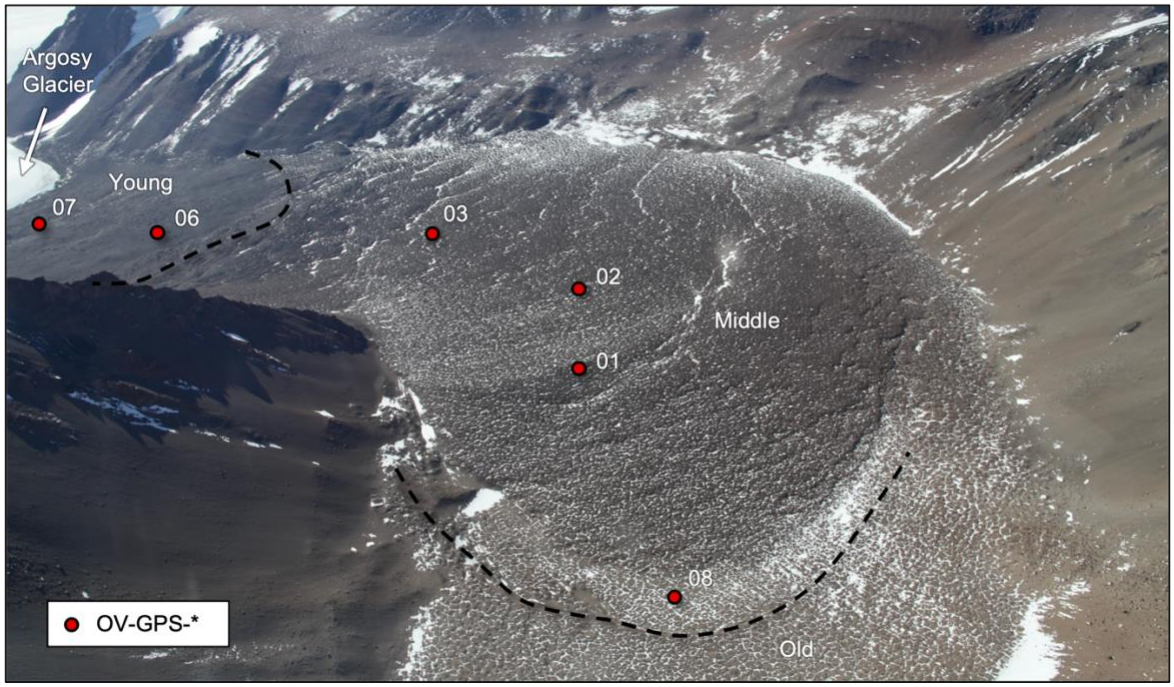

Figure 9.1 Aerial Photograph of Ong Valley with location of GNSS measured boulders. Red dots indicate the general boulder locations on the drift surface, with legend showing the prefix for boulder names. Black dashed line shows the boundary between the drifts. Boulders OV-GPS-06 and OV-GPS-07 is located on the surface of the young drift. Boulders OV-GPS-01, OV-GPS-02, OV-GPS-03 is located on the middle drift surface where buried ice is found below the supraglacial debris. Boulder OV-GPS-08 is located on the middle drift but in an area depleted of ice, and found near the boundary to the old drift. A transition zone between the young and middle drift can be observed between boulders OV-GPS-06 and OV-GPS-03.

Boulder OV-GPS-08 is located near the boundary between middle and old drift. More specifically, this boulder is positioned on middle drift but beyond the current extent of the middle ice. Therefore, boulder OV-GPS-08 is part of the middle drift surface that has been depleted of ice and considered to be relict. The stability of boulder OV-GPS-08 is questionable, as it is positioned on top of a debris mound and not partially embedded in the debris (Fig. 7.3). These debris mounds are left behind when the ice below polygon formations completely sublimates. On a million-year timescale, these debris mounds are expected to erode and flatten slowly, as observed on the surface of the old drift. Given the instability of boulder OV-GPS-08, such erosion could contribute to a

tilting in the bolt position and result in a general upward movement of 1.68 +/- 1.50 cm. However, again, this is speculative.

The old drift is completely depleted of buried ice based on the observations of the valley cross-sectional profiles. If the separate, older ice mass below the middle ice is that of the old drift deposit, then the oldest drift was deposited 4-5 Myrs ago and considered an ancient, relict surface. Boulder OV-GPS-04 and OV-GPS-05 agree with such, as no movement is detected.

We find the stability of the three drifts in Ong Valley increases with distance from the valley mouth and, therefore, age (Bibby et al., 2016; Scarrow et al., 2014). The youngest drift appears to be dynamic, indicating active movement of the ice below the supraglacial debris. The middle ice is considered to be stable with a potential boundary relaxation and adjustment because of the loss of buttressing by the now retreating Argosy Glacier since the LGM. The middle drift surface could still experience slow erosion and/or polygon formations. However, no ice movement is observed. As expected, the old drift is relict.

9.2 Sublimation Rate

The Monte Carlo simulation for the forward modeling results in a sublimation rate that is tightly constrained between 22.77 – 22.96 m Myr^{-1} (Fig. 8.7b) and independent of the age and erosion rate (Fig. 8.7d,e). With increasing sublimation rate, a sample having low nuclide concentration at deeper depth (caused by increased shielding mass) approaches the ice surface more rapidly. Having spent less time near the ice surface, a sample found in the top meter of the

ice will have a much lower total nuclide concentration than a sample at the lower part of the supraglacial debris. This difference in nuclide concentration between the uppermost ice sample and the bottom supraglacial debris sample allows for the sublimation rate to be well constrained.

Previous estimates of the sublimation rate in Ong Valley range between 19-22 m Myr^{-1} (Bibby et al., 2016), where sublimation rates of buried ice masses determined using cosmogenic nuclides elsewhere in TAM range between 0.7 - 37 m Myr^{-1} (Morgan et al., 2010a; Ng et al., 2005; Schäfer et al., 2000). These rates broadly agree with a sublimation rate of 22.86 m Myr^{-1} as reported here in Ong valley. Sublimation rates obtained from modeled water vapor diffusion are order of magnitude higher; 100-500 m Myr^{-1} (Hagedorn et al., 2007; Hindmarsh et al., 1998; Kowalewski et al., 2006; McKay et al., 1998; McKay, 2008; Schorghofer, 2009). Such orders of magnitude higher sublimation rates would suggest a total surface elevation lowering of ~ 300 – 1500 m as compared to our calculated total ice surface lowering of ~68 m and are inconsistent with glacial moraine elevations and field observations in Ong Valley.

From mapping the lateral moraines, we find that the middle drift experienced a surface lowering of >37 m. This minimum surface lowering assumes a flat ice surface between lateral moraines during deposition. However, glaciers generally have a convex cross-sectional profile where the center is elevated compared to the edge. Therefore, the surface lowering of the middle ice determined from the lateral moraines is expected to be a few tens of meters more and agrees with the calculated total ice surface lowering of ~68 m obtained from the forward model using cosmogenic nuclides.

The sublimation rate represents an average rate since the ice emplacement ~3 Myr ago. Most likely the sublimation has been decreasing over time as the supraglacial debris thickens (Mackay and Marchant, 2016). However, this relationship is uncertain, and therefore we do not account for it.

9.3 Erosion Rate

The erosion rate and age of the ice are well constrained within an erosion-age tradeoff (Fig. 8.7f). For an eroding surface, debris of low nuclide concentrations from below will approach the surface at a rate of erosion. With increased surface erosion rate, an older exposure age is required in order to account for the loss of high surficial nuclide concentrations, leading to an expected erosion-age tradeoff.

The majority of Antarctic studies of subaerial surface erosion rate using cosmogenic nuclides are obtained from boulders and bedrock of various lithologies (Marrero et al., 2018, and references therein). Only a few erosion rates have been determined from surficial regolith (Bibby et al., 2016; Morgan et al., 2010a; Putkonen et al., 2008). While Bibby et al. (2016) found a 0.89 m Myr^{-1} for the middle drift, a range between 0.2 - 2 m Myr^{-1} has been observed in McMurdo Dry Valleys (Morgan et al., 2010a; Putkonen et al., 2008). Therefore, an erosion rate of 0.206 m Myr^{-1} as reported here for the supraglacial debris is in agreement.

9.4 Englacial Debris Concentration

In Ong Valley, we measured an average debris concentration of 0.13 by weight in the ice (Eq. 1) which is in the same range as measurements made in Beacon Valley (0.085 by Marchant et al., 2002; and 0.12-0.45 by Morgan et al., 2010a). While the modeled debris concentration of 0.035 by weight in the sublimated ice over a span of 2.95 Ma is lower than measured debris concentration of buried ice in Antarctica, it is consistent with the expectation that the debris content increases towards the bottom of glacial ice, due to subglacial entrainment of the debris. Thus, it is expected that the modeled debris concentration for the sublimated ice here results in a lower concentration than measured in the remaining basal ice.

9.5 Mixing Layer

Predicted cosmogenic nuclide concentrations in the supraglacial debris decreases with depth at a higher rate than measured nuclide concentrations (Fig. 8.9). This leads to a systematic misfit between observations and model predictions. By either decreasing the sublimation rate, increasing the erosion rate, and/or decreasing the age of ice emplacement, a steeper predicted cosmogenic nuclide depth profile can be obtained for the supraglacial debris. However, neither of these scenarios will result in a better fit for the near-surface pit samples. The difficulty of fitting the forward model to the near-surface pit samples suggests that partial vertical mixing of the supraglacial debris may have occurred.

As the supraglacial debris is accumulating due to sublimation, debris having low cosmogenic nuclide concentrations from below will mix with debris of higher surficial cosmogenic nuclide concentrations. Therefore, any (partial or full) vertical mixing of the supraglacial debris would cause a decrease in the cosmogenic nuclides inventory in any above lying sample. Without accounting for any vertical mixing of the supraglacial debris, the model predictions result in an overestimation of the cosmogenic nuclide concentration for the near-surface pit samples and an underestimation of newly accumulating supraglacial debris from the ice surface as observed in Fig. 8.9a-c. Further, any vertical mixing would decrease the nuclide ratio, which would explain why all paired-nuclide ratios for the supraglacial debris samples plots below the steady state erosion zone (Fig. 8.9d-f).

It has previously been suggested that no vertical mixing occurs in the supraglacial debris layers in Ong valley (Bibby et al., 2016) and supraglacial debris layers studied in Beacon Valley (Morgan et al., 2010a, b). While the current measured nuclide profile may not reflect a fully mixed zone as seen elsewhere in temperate climate with bioturbation (Perg et al., 2002), a partially mixed supraglacial debris layer is likely the result of active polygon formation found at the surface of the middle drift.

9.6 Exposure Ages from Boulders

In general, a boulder having experienced a single period of exposure that is equal to the ice emplacement age of the middle drift should display concordant ^{10}Be and ^{21}Ne ages. However, all

measured boulders show apparent ^{10}Be exposure ages (Table 8.3) younger than that of ^{21}Ne ages and are therefore inconsistent with a simple exposure having negligible erosion.

From the ^{10}Be/^{21}Ne ratio (Fig.9.2) it is observed that the surface boulders have experienced erosion while exposed to cosmic-rays at the surface as the paired-nuclide ratio lays within the steady-state erosion zone (see details in sect. 6.5). Three outliers of the east lateral moraine boulders (214, 217, and 218; Fig. 9.2a) show neither age or erosion rates that agree with continuous exposure and lie below the steady erosion zone, in a region of intermittent exposure. Thus, these boulders show a complex exposure history having experienced at least one period of burial at some point in time.

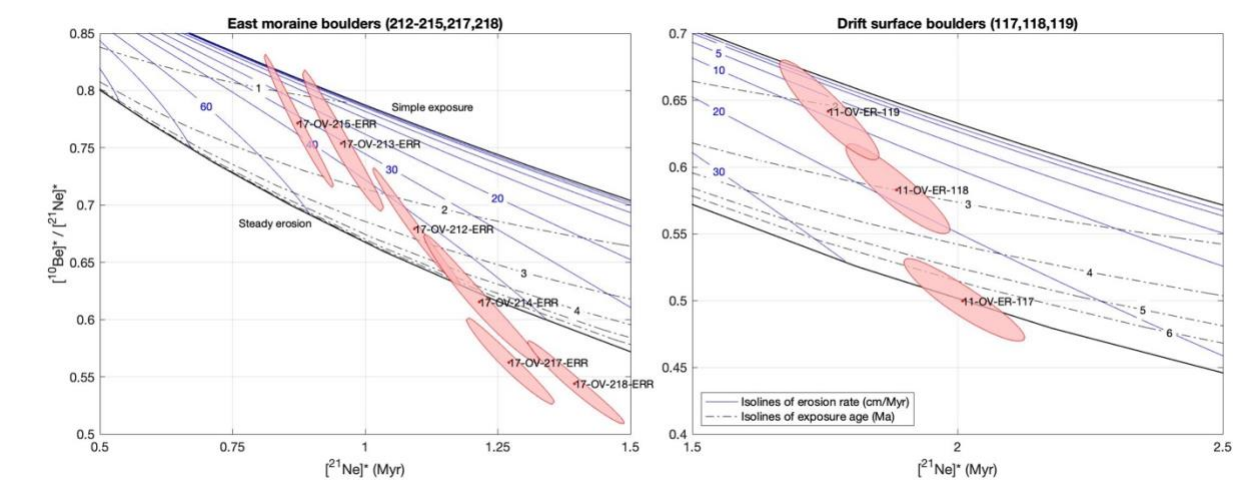

Figure 9.2 ^{10}Be - ^{21}Ne paired-nuclide diagram of the boulder samples. Black solid lines are the simple exposure line and steady state erosion line, which marks the zone of continuous exposure. Blue lines are isolines of constant steady erosion (cm Myr^{-1}), and black dashed lines are isoline of constant exposure age (Myr). The measured nuclide concentration for each sample is represented by a red dot with red shading of its 1-sigma uncertainty. *Nuclide concentrations normalized to respective surface production rate.

A more realistic exposure age and erosion rate can be determined for boulders having a nuclide ratio within the steady-state erosion zone. By assuming a single period of continuous

exposure at a steady state erosion, we can solve for both the exposure and erosion rate using Eq. (3) and detailed in Balco et al. (2014). The results of a 10,000-iteration Monte Carlo simulation using this procedure are shown in Fig. 9.3. Some samples permit infinite ages at a steady erosion rate if the $^{10}Be/^{21}Ne$ nuclide ratio lies outside of the continuous exposure zone. Therefore, only samples permitting finite age-erosion rate solutions are shown in Fig. 9.3.

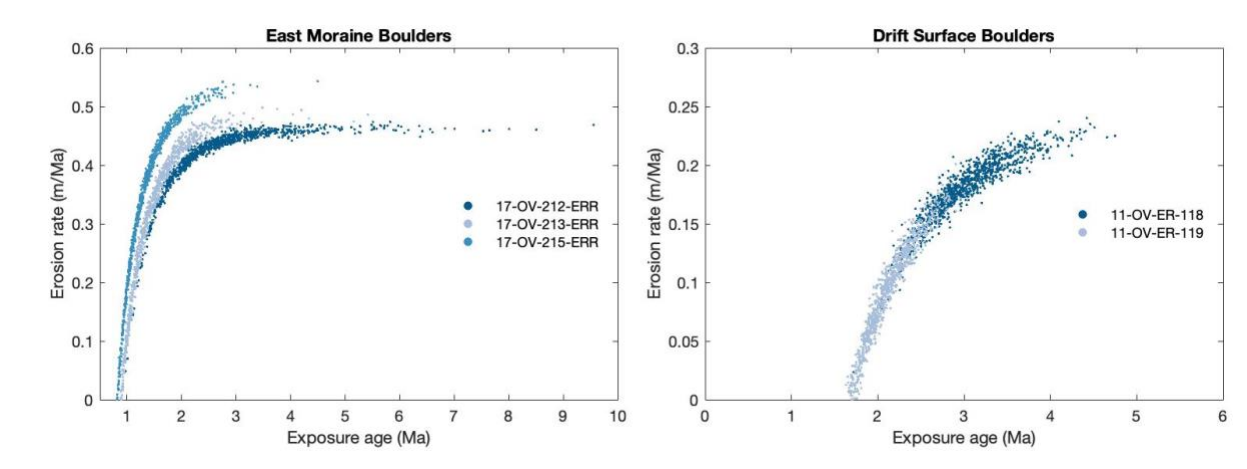

Figure 9.3 Exposure ages and erosion rates for the middle drift surface and moraine boulders.

The lateral moraine boulders having a finite age-erosion rate solution display a 68% confidence bound on the age of 1.0 – 3.9 Ma and erosion rates of 0.20 - 0.48 m Myr^{-1} (Fig. 9.3a). From field observations, the lateral moraine from which boulder measurements were sampled appears to be a younger recessional moraine and therefore not an indication of a maximum extent for the middle drift, which is observed at higher elevation. These observations would suggest that boulders from this lateral moraine have most likely been disturbed post ice emplacement. Thus, the ^{10}Be-^{21}Ne ratio age for the moraine is more likely to represent a minimum limiting age of ice emplacement (Hallet and Putkonen, 1994; Putkonen and Swanson, 2003).

The middle drift surface boulders have a 68% confidence bound on the age of 1.8 - 3.5 Ma with erosion rates ranging between 0.05 - 0.21 m Myr^{-1} and therefore agree with our modeled age of 2.96 Ma for the middle drift ice (Fig. 9.3b). One outlier (11-OV-ER-117) has steady state erosion for a period greater than several half-lives of Be-10 (> ~ 5 Ma), and therefore contains no age information. We attribute this increased nuclide concentrations to an extended period of exposure prior to deposition in Ong Valley.

9.7 Multiple Glacial Events

Samples having a burial age equal to that of the ice emplacement age are considered to have been derived from a paleo surface exposed in Ong Valley during ice advance of the middle ice. After entrainment into the advancing ice, the paleosurface material was immediately buried under a thick layer of ice and shielded from the cosmic-ray flux (Fig. 9.4).

As mentioned in sect. 8.4.2, the age of the ice determined from modeled nuclide predictions is constrained such that the ice cannot be older than the minimum burial age obtained from any sample across the three paired-nuclide ratios. We find that the minimum burial age of 3.21 ± 0.20 Ma for S2 agrees with the age of the middle ice (2.95 + 0.18/-0.21 Ma). Hence, S2 is likely to have been at the surface during the glacial advance leading to the deposition of the middle ice ~ 3 Ma. S2 is found at depths in between E1 and E2 (Fig. 8.6), which have no prior exposure history. This would suggest that S2 is not in stratigraphic order and has been mixed up into the ice during advance of the middle ice into Ong Valley.

Both S3 and S4 display older burial ages which are not uniform across the three paired-nuclide ratios (Fig. 9.3). This suggests that both S3 and S4 have experienced a complex exposure-burial history of prior entrainment which goes beyond the exposure history of the middle drift ice. The estimated burial ages represent the minimum total burial time a sample has experienced, but also the maximum burial time of a single burial event. For S3 and S4, additional burial time is needed beyond the age of the ice (> 2.95 Ma) and must have experienced multiple periods of burial. The simplest explanation is to assume that during advance of the middle ice, Ong Valley looked similar to today, such that the middle ice advanced over an already existing ice-cored drift unit. Perhaps this is now preserved as the older drift (Fig. 5.3 and Fig. 9.4). If this is the case, then S3 and S4 units presumably are debris that was buried for some time in the older ice, and then buried again in or under the middle ice. We use "in or under" because it is possible that (i) we cored through the middle ice into a stratigraphically underlying mass of older ice. However, it is also possible that (ii) sections of the older ice were entrained during advancement of the middle ice, and we then have a mixture of older and younger ice. The core did not display an obvious stratigraphic boundary. In fact, most of the observed grain in the ice-debris mass is at steep angles and disturbed (Sect. 8.3.1), which would tend to favor a mixing of the ice hypothesis. Regardless, either is possible and geochemical analysis of the ice could potentially help resolve this.

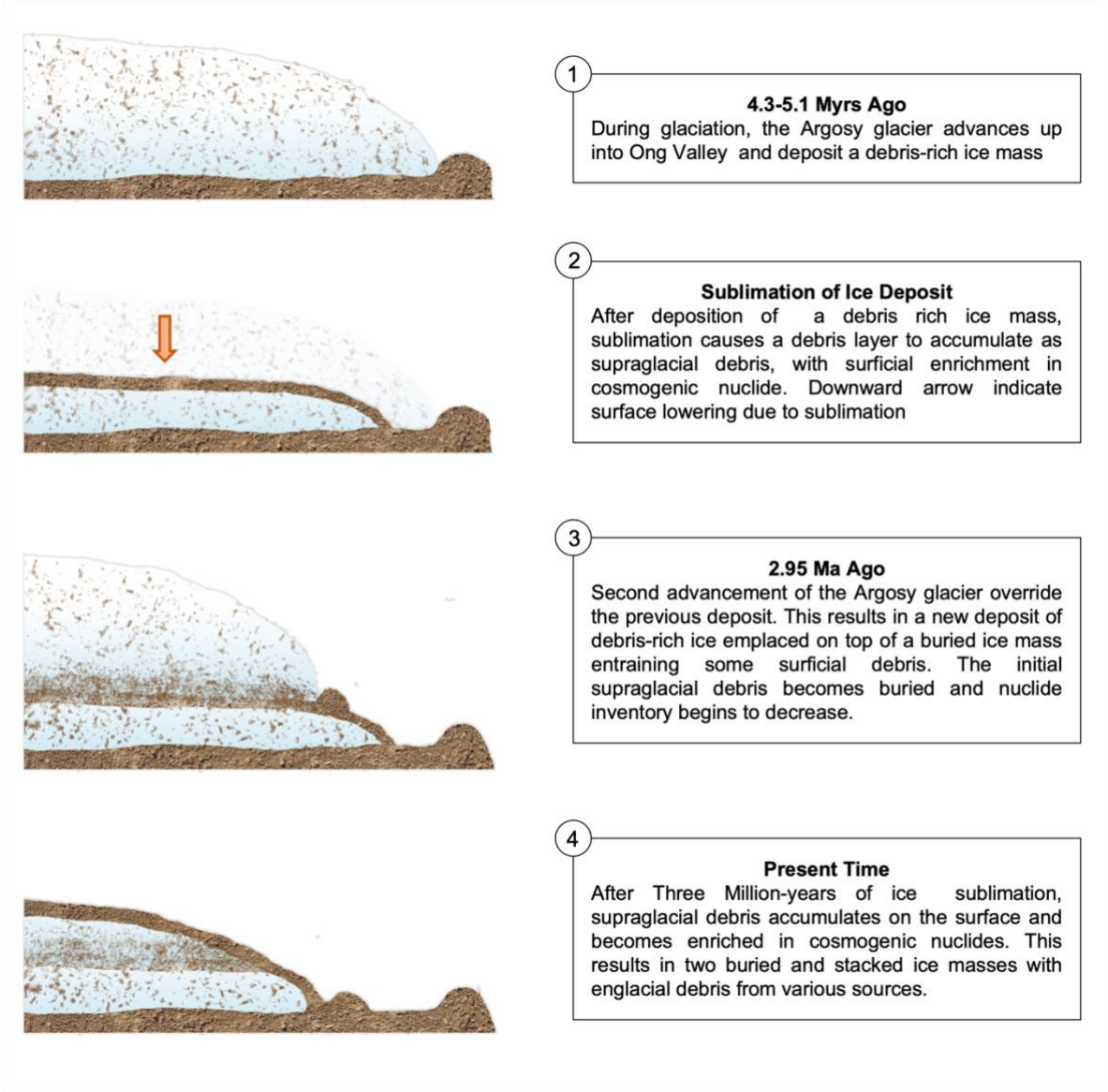

Figure 9.4 Schematic representation of the glacial history of Ong Valley and advancement of the Argosy Glacier.

The uncertainty associated with the age of this older, separate, underlying ice mass is greater compared to the middle ice due to the complexity associated with the exposure-burial dating. That is, the burial age obtained here is the apparent burial of a single event. However, a sample could have experienced multiple shorter periods of exposure-burial events which are not accounted for. We therefore only report an estimate with minimum and maximum constraints. A

sample that experiences a single period of exposure at the surface have nuclide concentration ratio dependent on the duration of exposure. When buried to a depth where nuclide production is significantly reduced, the change in ratio is primarily dependent on the radioactive decay associated with the duration of burial. Therefore, when solving for the burial age for each of these paleosurface units, we can also solve for the exposure age that has occurred prior to burial by the middle ice (Balco and Rovey, 2008).

With S2 representing a surface sample from a supraglacial debris prior to deposition of the middle ice, we find the surface exposure age of S2 to be 0.163 ± 0.058 Ma, 0.268 ± 0.046 Ma, and 0.268 ± 0.046 Ma for the paired-nuclide ratios, $^{26}Al/^{10}Be$, $^{10}Be/^{21}Ne$, and $^{26}Al/^{21}Ne$ respectively. This suggests that the age of an underlying ice mass is at least that of the minimum burial age plus the exposure age for S2. On the contrary, the age of the ice in which a sample is embedded cannot be older than the burial age of a given sample. Then, the maximum burial age across the three paleo surfaces S2-4 for any of the paired-nuclide ratios must serve as the upper bound for the age. Therefore, there is no scenario in which this separate, older underlying ice mass can be younger than 3.3 Myr or older than 7.6 Myr. However, a more likely age for this older deposit would be 4.3 – 5.1 Ma which is the burial age obtained from the $^{26}Al/^{10}Be$ ratio for S3 and S4, as it is unclear whether or not S3 and S4 are the same or different units.

It is difficult to determine whether or not there is any defined boundary between the older and younger ice masses. With an increase of nuclide concentrations downcore and, in addition, that samples from E2, S3, and S4 appear to form mixing arrays in the two-nuclide diagrams shown in Fig. 8.9, it appears likely that S3 is a mixture of a high-nuclide-concentration end member,

which may be represented by S4, and a low-nuclide-concentration end member represented by E2. However, a boundary or transition most likely exists between E2 and S4.

9.8 Ong Valley and Antarctica During the Pliocene Epoch

The ages reported here coincide with the Pliocene Epoch (5.3 – 2.6 Ma). Research on Pliocene climate and how it affected the AIS has gained much attention as a likely analog for modern anthropogenic warming (Dolan et al., 2018). During the Pliocene Epoch there is evidence of prominent glacial deposits, in which two are identified in the southern hemisphere as globally recognizable glaciations (summarized in De Schepper et al., 2014); one occurring during the early Pliocene (ca. 4.9-4.8 Ma), and another during the Late Pliocene (ca. 3.3 Ma). The latter is followed by a warmer-than present mPWP (~3.3-3.0 Ma) (De Schepper et al., 2014; Dowsett et al., 2016; Haywood et al., 2013). This warming period ends by a Late Pliocene cooling, post ~ 3 Ma, leading to a global glaciation around the Pliocene-Pleistocene boundary (De Schepper et al., 2014).

Because the uncertainty of the ice emplacement age (± 0.2 Ma) exceeds both the 40 kyr and 100 kyr climate cycles of the Pliocene Epoch (Caballero-Gill et al., 2019), we are not able to accurately relate the deposition of the middle ice to an individual glacial event. Furthermore, the age of 2.95 +0.18/-0.22 Ma for the middle ice emplacement, which requires an EAIS elevation greater than 200 m above present, cannot confidently be assigned to either the warmer period prior to 3 Ma or the cooler period post 3 Ma. Balter-Kennedy et al. (2020) concluded that glacial deposits recording a higher than present EAIS elevation at Roberts Massif, a nearby location in the TAM, most likely postdated the mPWP. Therefore, if the ice advance in Ong Valley were correlative

with that at Roberts Massif, it would also be associated with the 3 Ma cooling. However, this is speculative.

The oldest englacial debris that we have dated in Ong Valley is dated at ~4.3-5.1 Myrs old. Although the dated age range is rather wide due to complexities resulting from old age and exposure-burial dating, it is still direct evidence of an EAIS expansion and local ice expansion during that time. This dated age suggests that the ice sheet expansion predated the MIS M2 cooling event and possibly coincided with the Early Pliocene global glaciation (ca. 4.9 - 4.8 Ma). If in fact the older ice is still present below the middle ice mass, then it did not melt during a period of warming. Thus, additional evidence indicating whether or not two ice units are present would be important in understanding the climate during the Pliocene Epoch. Since ~3 Myrs ago, Ong Valley has not seen an ice sheet expansion comparable to those of the early/mid and late Pliocene. The only notable, but small, ice sheet advance or stagnation evident in Ong Valley is the youngest drift dated at 11-13 kyrs.

CHAPTER 10
CONCLUSIONS

Glacial ice is a well-known paleo climate archive. Great efforts have been made to find ice older than 1 Ma since the paucity of ice beyond million years of age creates uncertainties for future climate predictions. In Ong Valley, Antarctica, the middle drift harbors a large ice mass buried 62 cm below the surface of supraglacial debris. To understand its overall geologic history, and evaluate its potential use as a paleoclimate archive, we mapped the glacial moraines present in Ong Valley and measured any potential movement from surface boulder. We Then collected a 944 cm long ice core and measured concentrations of the cosmic-ray produced nuclides ^{10}Be, ^{26}Al, and ^{21}Ne from the englacial debris and samples from the supraglacial debris directly above it to determine the age of deposition. We developed a numerical forward model which predicts the accumulation of cosmogenic nuclides in the englacial debris and the above laying supraglacial debris during a single event of exposure, constrained by sublimation, surface erosion and accumulation of supraglacial debris. The modeled nuclide concentrations are then fitted to the measured nuclide concentrations in the ice core.

We find the stability of the three drifts to increase with distance from the valley mouth. The youngest drift shows a dynamic young ice mass, with boulder movement between 5.55 – 7.73 cm down valley. The middle drift is considered stable with minimal surface movement caused by

a slowly eroding supraglacial debris surface. As expected, the oldest drift which is depleted of ice is considered relict.

Downcore increase in measured nuclide concentrations suggest that sections of englacial debris consist of both subglacially entrained debris and recycled paleo surfaces having a complex exposure-burial history prior to entrainment. This allows us to apply a combination of exposure- and burial-dating to the forward model. We find the age of the middle drift ice mass to be 2.95 Ma, with a constant ice sublimation rate of 22.86 m Myr^{-1} and surface erosion rate of 0.206 m Myr^{-1}. Cosmogenic nuclide exposure dating of surface boulders belonging to the surface of the coring site are consistent with the modeled age of ~3 Ma for the ice emplacement.

Exposure-burial dating on the englacial paleo surface debris reveals that the lower section of the ice core belongs to a separate and older deposit, emplaced ~4.3 – 5.1 Myr ago. We interpret this lower section as a portion of an older ice mass either *in situ* or transported during emplacement of the younger ice. The ages of the two separate ice masses found below the middle drift can be directly related to glacial advances. These findings provide direct evidence of an Antarctic ice sheet that was larger than present during the early and late Pliocene Epoch.

Furthermore, we show that exposure-burial dating of cosmogenic nuclides measured *in situ* in basal ice debris layers can be used for age constraint of past ice advance. Specifically, we have debris layers in one ice core that suggest three different burial ages, where at least two of them are dated to be older than the age of the ice itself. This is important for understanding *in situ* cosmogenic-nuclide data from out of context subglacial sediment.

Collectively our results show that the continental ice sheet advanced into Ong Valley repeatedly and evidence of at least two of such advances at 2.95 Ma, and 4.3-5.1 Ma are still preserved in lateral moraines, drifts, and stacked ice masses. Since 2.95 Myrs ago the only evidence of ice advance or stagnation in the Ong Valley was ~10 kyrs ago.

While buried ice masses have been found in both Beacon Valley and Ong Valley, their frequencies throughout the Transantarctic mountains are unknown. Therefore, it is not unlikely that similar ancient ice masses such as that of the middle ice in Ong Valley exist. Furthermore, given the sparsity of direct evidence on Pliocene glacial dynamics, such buried ice masses may provide critical limitations on the possible mPWP amplitude, as the ice would have melted if significant enough warming had occurred. Thus, the survival of ancient, buried ice can be used for numerical estimates of the limits of such warming.

Therefore, we see significant value in expanding this type of analysis described in this paper to other buried ice masses in the TAM that experience similar characteristics to Ong Valley and particularly that of the middle drift, where ancient ice is preserved by supraglacial debris. Such work could provide robust evidence of ice sheet high stands and aid more spatial and temporal constraints on East Antarctic Ice Sheet advance and climatic conditions during the late Pliocene Epoch and potentially aid in constraining models of future sea level rise during a warming climate.

REFERENCES

Ackert, R.P., Jr., Barclay, D.J., Borns, H.W., Jr., Calkin, P.E., Kurz, M.D., Fastook, J.L., Steig, E.J., 1999. Measurements of Past Ice Sheet Elevations in Interior West Antarctica. Science 286, 276-280.

Ackert, R.P., Kurz, M.D., 2004. Age and uplift rates of Sirius Group sediments in the Dominion Range, Antarctica, from surface exposure dating and geomorphology. Global Planet Change 42, 207-225.

Alley, R.B., Lawson, D.E., Evenson, E.B., Strasser, J.C., Larson, G.J., 1998. Glaciohydraulic supercooling: a freeze-on mechanism to create stratified, debris-rich basal ice: II. Theory. J Glaciol 44, 563-569.

Anderson, R.S., Repka, J.L., Dick, G.S., 1996. Explicit treatment of inheritance in dating depositional surfaces using in situ 10Be and 26Al. Geology 24.

Balco, G., 2011. Contributions and unrealized potential contributions of cosmogenic-nuclide exposure dating to glacier chronology, 1990–2010. Quaternary Science Reviews 30, 3-27.

Balco, G., 2015. The absence of evidence of absence of the East Antarctic Ice Sheet. Geology 43, 943-944.

Balco, G., 2016. Saturated surfaces in Antarctica. The bleeding edge of cosmogenic-nuclide geochemistry. https://cosmognosis.wordpress.com/2016/09/09/saturated-surfaces-in-antarctica/.

Balco, G., 2017. Production rate calculations for cosmic-ray-muon-produced 10Be and 26Al benchmarked against geological calibration data. Quat Geochronol 39, 150-173.

Balco, G., Blard, P.-H., Shuster, D.L., Stone, J.O.H., Zimmermann, L., 2019. Cosmogenic and nucleogenic 21Ne in quartz in a 28-meter sandstone core from the McMurdo Dry Valleys, Antarctica. Quat Geochronol 52, 63-76.

Balco, G., Rovey, C.W., 2008. An isochron method for cosmogenic-nuclide dating of buried soils and sediments. American Journal of Science 308, 1083-1114.

Balco, G., Shuster, D.L., 2009. Production rate of cosmogenic 21Ne in quartz estimated from 10Be, 26Al, and 21Ne concentrations in slowly eroding Antarctic bedrock surfaces. Earth and Planetary Science Letters 281, 48-58.

Balco, G., Stone, J.O., Lifton, N.A., Dunai, T.J., 2008. A complete and easily accessible means of calculating surface exposure ages or erosion rates from 10Be and 26Al measurements. Quat Geochronol 3, 174-195.

Balco, G., Stone, J.O.H., Sliwinski, M.G., Todd, C., 2014. Features of the glacial history of the Transantarctic Mountains inferred from cosmogenic 26Al, 10Be and 21Ne concentrations in bedrock surfaces. Antarctic Science 26, 708-723.

Balter-Kennedy, A., Bromley, G., Balco, G., Thomas, H., Jackson, M.S., 2020. A 14.5-million-year record of East Antarctic Ice Sheet fluctuations from the central Transantarctic Mountains, constrained with cosmogenic 3He, 10Be, 21Ne, and 26Al. The Cryosphere 14, 2647-2672.

Barrett, P.J., Lindsay, J.F., Gunner, J., 1970. Reconnaissance geologic map of the Mount Rabot quadrangle, Transantarctic Mountains, Antarctica., Antarctic Map.

Behrendt, J.C., 2013. The aeromagnetic method as a tool to identify Cenozoic magmatism in the West Antarctic Rift System beneath the West Antarctic Ice Sheet — A review; Thiel subglacial volcano as possible source of the ash layer in the WAISCORE. Tectonophysics 585, 124-136.

Behrendt, J.C., LeMasurier, W.E., Cooper, A.K., Tessensohn, F., Tréhu, A., Damaske, D., 1991. Geophysical studies of the West Antarctic Rift System. Tectonics 10, 1257-1273.

Bentley, M.J., Fogwill, C.J., Le Brocq, A.M., Hubbard, A.L., Sugden, D.E., Dunai, T.J., Freeman, S.P.H.T., 2010. Deglacial history of the West Antarctic Ice Sheet in the Weddell Sea embayment: Constraints on past ice volume change. Geology 38, 411-414.

Bibby, T., 2014. Landscape evolution and preservation of ice over one million years old quantified with cosmogenic nuclides 26Al, 10Be, and 21Ne, Ong Valley, Antarctica.

Bibby, T., Putkonen, J., Morgan, D., Balco, G., Shuster, D.L., 2016. Million year old ice found under meter thick debris layer in Antarctica. Geophysical Research Letters 43, 6995-7001.

Bo, S., Siegert, M.J., Mudd, S.M., Sugden, D., Fujita, S., Xiangbin, C., Yunyun, J., Xueyuan, T., Yuansheng, L., 2009. The Gamburtsev mountains and the origin and early evolution of the Antarctic Ice Sheet. Nature 459, 690-693.

Bockheim, J.G., Wilson, S.C., Denton, G.H., Andersen, B.G., Stuiver, M., 1989. Late Quaternary Ice-Surface Fluctuations of Hatherton Glacier, Transantarctic Mountains. Quaternary Research 31, 229-254.

Boeckmann, G.V., Gibson, C.J., Kuhl, T.W., Moravec, E., Johnson, J.A., Meulemans, Z., Slawny, K., 2020. Adaptation of the Winkie Drill for subglacial bedrock sampling. Ann Glaciol 62, 109-117.

Borchers, B., Marrero, S., Balco, G., Caffee, M., Goehring, B., Lifton, N., Nishiizumi, K., Phillips, F., Schaefer, J., Stone, J., 2016. Geological calibration of spallation production rates in the CRONUS-Earth project. Quat Geochronol 31, 188-198.

Braucher, R., Del Castillo, P., Siame, L., Hidy, A.J., Bourlés, D.L., 2009. Determination of both exposure time and denudation rate from an in situ-produced 10Be depth profile: A mathematical proof of uniqueness. Model sensitivity and applications to natural cases. Quat Geochronol 4, 56-67.

Bromley, G.R.M., Hall, B.L., Stone, J.O., Conway, H., Todd, C.E., 2010. Late Cenozoic deposits at Reedy Glacier, Transantarctic Mountains: implications for former thickness of the West Antarctic Ice Sheet. Quaternary Science Reviews 29, 384-398.

Brook, E.J., Brown, E.T., Kurz, M.D., Ackert, R.P., Raisbeck, G.M., Yiou, F., 1995. Constraints on age, erosion, and uplift of Neogene glacial deposits in the Transantarctic Mountains determined from in situ cosmogenic 10Be and 26Al. Geology 23, 1063–1066.

Brook, E.J., Kurz, M.D., Ackert, R.P., Denton, G.H., Brown, E.T., Raisbeck, G.M., Yiou, F., 1993. Chronology of Taylor Glacier Advances in Arena Valley, Antarctica, Using in Situ Cosmogenic 3He and 10Be. Quaternary Research 39, 11-23.

Brown, E.T., Edmond, J.M., Raisbeck, G.M., Yiou, F., Kurz, M.D., Brook, E.J., 1991. Examination of surface exposure ages of Antarctic moraines using in situ produced 10Be and 26Al. Geochimica et Cosmochimica Acta 55, 2269-2283.

Brown, L., 1984. Applications of Accelerator Mass Spectrometry. Annual Review of Earth and Planetary Sciences 12, 39-59.

Bruno, L.A., Baur, H., Graf, T., Schlu, C., Signer, P., Wieler, R., 1997. Dating of Sirius Group tillites in the Antarctic Dry Valleys with cosmogenic 3He and 21Ne. Earth and Planetary Science Letters 147, 37-54.

Bulthuis, K., Arnst, M., Sun, S., Pattyn, F., 2019. Uncertainty quantification of the multi-centennial response of the Antarctic ice sheet to climate change. The Cryosphere 13, 1349-1380.

Caballero-Gill, R.P., Herbert, T.D., Dowsett, H.J., 2019. 100-kyr Paced Climate Change in the Pliocene Warm Period, Southwest Pacific. Paleoceanography and Paleoclimatology 34, 524-545.

Cao, W., Zahirovic, S., Flament, N., Williams, S., Golonka, J., Müller, R.D., 2017. Improving global paleogeography since the late Paleozoic using paleobiology. Biogeosciences 14, 5425-5439.

Castellano, E., Becagli, S., Jouzel, J., Migliori, A., Severi, M., Steffensen, J.P., Traversi, R., Udisti, R., 2004. Volcanic eruption frequency over the last 45 ky as recorded in Epica-Dome C ice core (East Antarctica) and its relationship with climatic changes. Global Planet Change 42, 195-205.

Cogley, G.J., 1984. Deglacial hypsometry of Antarctica. Earth and Planetary Science Letters 67, 284-296.

Cogley, J.G., Arendt, A., Bauder, A., Braithwaite, R., Hock, R., Jansson, P., Kaser, G., Moller, M., Nicholson, L., Rasmussen, L., 2010. Glossary of glacier mass balance and related terms. (IHP-VII Technical Documents in Hydrology). International Hydrological Programme.

Colleoni, F., De Santis, L., R. Naish, T., DeConto, R.M., Escutia, C., Stocchi, P., Uenzelmann-Neben, G., Hochmuth, K., Hillenbrand, C.-D., van de Flierdt, T., Pérez, L.F., Leitchenkov, G., Sangiorgi, F., Jamieson, S., Bentley, M.J., Wilson, D.J., 2022. Chapter 12 - Past Antarctic ice sheet dynamics (PAIS) and implications for future sea-level change, in: Florindo, F., Siegert, M., Santis,

L.D., Naish, T. (Eds.), Antarctic Climate Evolution (Second Edition). Elsevier, Amsterdam, pp. 689-768.

Corbett, L.B., Bierman, P.R., Rood, D.H., 2016. An approach for optimizing in situ cosmogenic 10Be sample preparation. Quat Geochronol 33, 24-34.

Cuffey, K.M., Conway, H., Gades, A.M., Hallet, B., Lorrain, R., Severinghaus, J.P., Steig, E.J., Vaughn, B., White, J.W.C., 2000. Entrainment at cold glacier beds. Geology 28, 351–354.

Dansgaard, W., Johnsen, S.J., Moller, J., Langway, C.C., Jr., 1969. One thousand centuries of climatic record from camp century on the greenland ice sheet. Science 166, 377-380.

Davis, R., Schaeffer, O.A., 1955. Chlorine-36 in nature. Annals of the New York Academy of Sciences 62, 107-121.

De Schepper, S., Gibbard, P.L., Salzmann, U., Ehlers, J., 2014. A global synthesis of the marine and terrestrial evidence for glaciation during the Pliocene Epoch. Earth-Science Reviews 135, 83-102.

Deconto, R.M., Pollard, D., 2003. Rapid Cenozoic glaciation of Antarctica induced by declining atmospheric CO2. Nature 421, 245-249.

Deconto, R.M., Pollard, D., 2016. Contribution of Antarctica to past and future sea-level rise. Nature 531, 591-597.

DeConto, R.M., Pollard, D., Alley, R.B., Velicogna, I., Gasson, E., Gomez, N., Sadai, S., Condron, A., Gilford, D.M., Ashe, E.L., Kopp, R.E., Li, D., Dutton, A., 2021. The Paris Climate Agreement and future sea-level rise from Antarctica. Nature 593, 83-89.

Denton, G.H., Bockheim, J.G., Wilson, S.C., Leide, J.E., Andersen, B.G., 1989. Late Quaternary Ice-Surface Fluctuations of Beardmore Glacier, Transantarctic Mountains. Quaternary Research 31, 183-209.

Denton, G.H., Sugden, D.E., 2005. Meltwater features that suggest miocene ice-sheet overriding of the transantarctic mountains in victoria land, antarctica. Geografiska Annaler: Series A, Physical Geography 87, 67-85.

Denton, G.H., Sugden, D.E., Marchant, D.R., Hall, B.L., Wilch, T.I., 1993. East Antarctic Ice Sheet Sensitivity to Pliocene Climatic Change from a Dry Valleys Perspective. Geografiska Annaler. Series A, Physical Geography 75, 155.

Dingle, R.V., Lavelle, M., 1998. Late Cretaceous–Cenozoic climatic variations of the northern Antarctic Peninsula: new geochemical evidence and review. Palaeogeography, Palaeoclimatology, Palaeoecology 141, 215-232.

Dolan, A.M., de Boer, B., Bernales, J., Hill, D.J., Haywood, A.M., 2018. High climate model dependency of Pliocene Antarctic ice-sheet predictions. Nat Commun 9, 2799.

Dowsett, H., Dolan, A., Rowley, D., Moucha, R., Forte, A.M., Mitrovica, J.X., Pound, M., Salzmann, U., Robinson, M., Chandler, M., Foley, K., Haywood, A., 2016. The PRISM4 (mid-Piacenzian) paleoenvironmental reconstruction. Climate of the Past 12, 1519-1538.

Dunai, T.J., 2010. Cosmogenic Nuclides: Principles, Concepts and Applications in the Earth Surface Sciences. Cambridge University Press, Cambridge.

Edwards, K.L., Padilla, A.J., Evans, A., Morgan, D., Balco, G., Putkonen, J., Bibby, T., 2014. Provenance of glacial tills in Ong Valley, Antarctica, inferred from quartz cathodoluminescence

imaging, zircon U/Pb dating, and trace element geochemistry, American Geophysical Union, Fall Meeting 2014, San Francisco, Calif.

Edwards, T.L., Nowicki, S., Marzeion, B., Hock, R., Goelzer, H., Seroussi, H., Jourdain, N.C., Slater, D.A., Turner, F.E., Smith, C.J., McKenna, C.M., Simon, E., Abe-Ouchi, A., Gregory, J.M., Larour, E., Lipscomb, W.H., Payne, A.J., Shepherd, A., Agosta, C., Alexander, P., Albrecht, T., Anderson, B., Asay-Davis, X., Aschwanden, A., Barthel, A., Bliss, A., Calov, R., Chambers, C., Champollion, N., Choi, Y., Cullather, R., Cuzzone, J., Dumas, C., Felikson, D., Fettweis, X., Fujita, K., Galton-Fenzi, B.K., Gladstone, R., Golledge, N.R., Greve, R., Hattermann, T., Hoffman, M.J., Humbert, A., Huss, M., Huybrechts, P., Immerzeel, W., Kleiner, T., Kraaijenbrink, P., Le Clec'h, S., Lee, V., Leguy, G.R., Little, C.M., Lowry, D.P., Malles, J.H., Martin, D.F., Maussion, F., Morlighem, M., O'Neill, J.F., Nias, I., Pattyn, F., Pelle, T., Price, S.F., Quiquet, A., Radic, V., Reese, R., Rounce, D.R., Ruckamp, M., Sakai, A., Shafer, C., Schlegel, N.J., Shannon, S., Smith, R.S., Straneo, F., Sun, S., Tarasov, L., Trusel, L.D., Van Breedam, J., van de Wal, R., van den Broeke, M., Winkelmann, R., Zekollari, H., Zhao, C., Zhang, T., Zwinger, T., 2021. Projected land ice contributions to twenty-first-century sea level rise. Nature 593, 74-82.

Ensminger, S.L., Alley, R.B., Evenson, E.B., Lawson, D.E., Larson, G.J., 2001. Basal-crevasse-fill origin of laminated debris bands at Matanuska Glacier, Alaska, U.S.A. J Glaciol 47, 412-422.

Evatt, G.W., Abrahams, I.D., Heil, M., Mayer, C., Kingslake, J., Mitchell, S.L., Fowler, A.C., Clark, C.D., 2015. Glacial melt under a porous debris layer. J Glaciol 61, 825-836.

Ferraccioli, F., Finn, C.A., Jordan, T.A., Bell, R.E., Anderson, L.M., Damaske, D., 2011. East Antarctic rifting triggers uplift of the Gamburtsev Mountains. Nature 479, 388-392.

Fischer, H., Severinghaus, J., Brook, E., Wolff, E., Albert, M., Alemany, O., Arthern, R., Bentley, C., Blankenship, D., Chappellaz, J., Creyts, T., Dahl-Jensen, D., Dinn, M., Frezzotti, M., Fujita, S., Gallee, H., Hindmarsh, R., Hudspeth, D., Jugie, G., Kawamura, K., Lipenkov, V., Miller, H.,

Mulvaney, R., Parrenin, F., Pattyn, F., Ritz, C., Schwander, J., Steinhage, D., Van Ommen, T., Wilhelms, F., 2013. Where to find 1.5 million yr old ice for the IPICS "Oldest-Ice" ice core. Climate of the Past 9, 2489-2505.

Francis, J.E., Ashworth, A., Cantrill, D.J., Crame, J.A., Howe, J., Stephens, R., Tosolini, A.-M., Thorn, V., 2007. 100 Million Years of Antarctic Climate Evolution: Evidence from Fossil Plants, in: Cooper, A.K., P. J. Barrett, H. Stagg, B. Storey, E. Stump, W. Wise, and the 10th ISAES editorial team, eds. (Ed.).

Fredskild, B., Wagner, P., 1974. Pollen and fragments of plant tissue in core samples from the Greenland Ice Cap. Boreas 3, 105-108.

Fretwell, P., Pritchard, H.D., Vaughan, D.G., Bamber, J.L., Barrand, N.E., Bell, R., Bianchi, C., Bingham, R.G., Blankenship, D.D., Casassa, G., Catania, G., Callens, D., Conway, H., Cook, A.J., Corr, H.F.J., Damaske, D., Damm, V., Ferraccioli, F., Forsberg, R., Fujita, S., Gim, Y., Gogineni, P., Griggs, J.A., Hindmarsh, R.C.A., Holmlund, P., Holt, J.W., Jacobel, R.W., Jenkins, A., Jokat, W., Jordan, T., King, E.C., Kohler, J., Krabill, W., Riger-Kusk, M., Langley, K.A., Leitchenkov, G., Leuschen, C., Luyendyk, B.P., Matsuoka, K., Mouginot, J., Nitsche, F.O., Nogi, Y., Nost, O.A., Popov, S.V., Rignot, E., Rippin, D.M., Rivera, A., Roberts, J., Ross, N., Siegert, M.J., Smith, A.M., Steinhage, D., Studinger, M., Sun, B., Tinto, B.K., Welch, B.C., Wilson, D., Young, D.A., Xiangbin, C., Zirizzotti, A., 2013. Bedmap2: improved ice bed, surface and thickness datasets for Antarctica. The Cryosphere 7, 375-393.

Frieler, K., Clark, P.U., He, F., Buizert, C., Reese, R., Ligtenberg, S.R.M., Van Den Broeke, M.R., Winkelmann, R., Levermann, A., 2015. Consistent evidence of increasing Antarctic accumulation with warming. Nature Climate Change 5, 348-352.

Gillespie, A.R., Bierman, P.R., 1995. Precision of terrestrial exposure ages and erosion rates estimated from analysis of cosmogenic isotopes produced in situ. Journal of Geophysical Research: Solid Earth 100, 24637-24649.

Gohl, K., Uenzelmann-Neben, G., Gille-Petzoldt, J., Hillenbrand, C.D., Klages, J.P., Bohaty, S.M., Passchier, S., Frederichs, T., Wellner, J.S., Lamb, R., Leitchenkov, G., 2021. Evidence for a Highly Dynamic West Antarctic Ice Sheet During the Pliocene. Geophysical Research Letters 48.

Golledge, N.R., Thomas, Z.A., Levy, R.H., Gasson, E.G.W., Naish, T.R., McKay, R.M., Kowalewski, D.E., Fogwill, C.J., 2017. Antarctic climate and ice-sheet configuration during the early Pliocene interglacial at 4.23 Ma. Climate of the Past 13, 959-975.

Goodge, J.W., 2020. Geological and tectonic evolution of the Transantarctic Mountains, from ancient craton to recent enigma. Gondwana Research 80, 50-122.

Gosse, J.C., Phillips, F.M., 2001. Terrestrial in situ cosmogenic nuclides: theory and application. Quaternary Science Reviews 20, 1475-1560.

Graf, T., Kohl, C.P., Marti, K., Nishiizumi, K., 1991. Cosmic-Ray Produced Neon in Antarctic Rocks. Geophysical Research Letters 18, 203-206.

Granger, D.E., Smith, A.L., 2000. Dating buried sediments using radioactive decay and muogenic production of 26Al and 10Be. Nuclear Instruments and Methods in Physics Research Section B: Beam Interactions with Materials and Atoms 172, 822-826.

Grindley, G.W., 1967. The Geomorphology of the Miller Range, Transantarctic Mountains with notes on the glacial history and neotectonics of East Antarctica. New Zealand Journal of Geology and Geophysics 10, 557-598.

Hagedorn, B., Sletten, R.S., Hallet, B., 2007. Sublimation and ice condensation in hyperarid soils: Modeling results using field data from Victoria Valley, Antarctica. Journal of Geophysical Research 112.

Hallet, B., Putkonen, J., 1994. Surface dating of dynamic landforms: young boulders on aging moraines. Science 265, 937-940.

Haug, G.H., Tiedemann, R., 1998. Effect of the formation of the Isthmus of Panama on Atlantic Ocean thermohaline circulation. Nature 393, 673-676.

Haywood, A.M., Chandler, M.A., Valdes, P.J., Salzmann, U., Lunt, D.J., Dowsett, H.J., 2009. Comparison of mid-Pliocene climate predictions produced by the HadAM3 and GCMAM3 General Circulation Models. Global Planet Change 66, 208-224.

Haywood, A.M., Dowsett, H.J., Dolan, A.M., 2016. Integrating geological archives and climate models for the mid-Pliocene warm period. Nature Communications 7, 10646.

Haywood, A.M., Hill, D.J., Dolan, A.M., Otto-Bliesner, B.L., Bragg, F., Chan, W.L., Chandler, M.A., Contoux, C., Dowsett, H.J., Jost, A., Kamae, Y., Lohmann, G., Lunt, D.J., Abe-Ouchi, A., Pickering, S.J., Ramstein, G., Rosenbloom, N.A., Salzmann, U., Sohl, L., Stepanek, C., Ueda, H., Yan, Q., Zhang, Z., 2013. Large-scale features of Pliocene climate: results from the Pliocene Model Intercomparison Project. Climate of the Past 9, 191-209.

Heisinger, B., Lal, D., Jull, A.J.T., Kubik, P., Ivy-Ochs, S., Knie, K., Nolte, E., 2002a. Production of selected cosmogenic radionuclides by muons: 2. Capture of negative muons. Earth and Planetary Science Letters 200, 357-369.

Heisinger, B., Lal, D., Jull, A.J.T., Kubik, P., Ivy-Ochs, S., Neumaier, S., Knie, K., Lazarev, V., Nolte, E., 2002b. Production of selected cosmogenic radionuclides by muons 1. Fast muons. Earth and Planetary Science Letters 200, 345-355.

Heisinger, B., Niedermayer, M., Hartmann, F.J., Korschinek, G., Nolte, E., Morteani, G., Neumaier, S., Petitjean, C., Kubik, P., Synal, A., Ivy-Ochs, S., 1997. In-situ production of radionuclides at great depths. Nuclear Instruments and Methods in Physics Research Section B: Beam Interactions with Materials and Atoms 123, 341-346.

Herreid, S., Pellicciotti, F., 2020. The state of rock debris covering Earth's glaciers. Nature Geoscience 13, 621-627.

Hidy, A.J., Gosse, J.C., Pederson, J.L., Mattern, J.P., Finkel, R.C., 2010. A geologically constrained Monte Carlo approach to modeling exposure ages from profiles of cosmogenic nuclides: An example from Lees Ferry, Arizona. Geochemistry Geophysics Geosystems 11.

Hindmarsh, R.C.A., Van der Wateren, F.M., Verbers, A.L.L.M., 1998. Sublimation of ice through sediment in Beacon Valley, Antarctica. Geogr Ann A 80a, 209-219.

Howat, I.M., Porter, C., Smith, B.E., Noh, M.-J., Morin, P., 2019. The Reference Elevation Model of Antarctica. The Cryosphere 13, 665-674.

Hubbard, B., Sharp, M., 1993. Weertman regelation, multiple refreezing events and the isotopic evolution of the basal ice layer. J Glaciol 39, 275-291.

IPCC, 2022. Summary for Policymakers, in: Intergovernmental Panel on Climate, C. (Ed.), The Ocean and Cryosphere in a Changing Climate: Special Report of the Intergovernmental Panel on Climate Change. Cambridge University Press, Cambridge, pp. 3-36.

Ivy-ochs, S., Kober, F., 2008. Surface exposure dating with cosmogenic nuclides. Eiszeitalter und Gegenwart Quaternary Science Journal 57, 179-209.

Ivy-Ochs, s., Schlüchter, C., Kubik, P., Dittrich-Hannen, B., Beer, J., 1995. Minimum 10Be exposure ages of early Pliocene for the Table Mountain plateau and the Sirius Group at Mount Fleming, Dry Valleys, Antarctica. Geology 23, 1007-1010.

Jennings, S.J.A., Hambrey, M.J., Glasser, N.F., 2014. Ice flow-unit influence on glacier structure, debris entrainment and transport. Earth Surface Processes and Landforms 39, 1279-1292.

Johnson, J.S., Bentley, M.J., Gohl, K., 2008. First exposure ages from the Amundsen Sea Embayment, West Antarctica: The Late Quaternary context for recent thinning of Pine Island, Smith, and Pope Glaciers. Geology 36, 223.

Jordan, T.A., Riley, T.R., Siddoway, C.S., 2020. The geological history and evolution of West Antarctica. Nature Reviews Earth & Environment 1, 117-133.

Jouzel, J., Masson-Delmotte, V., Cattani, O., Dreyfus, G., Falourd, S., Hoffmann, G., Minster, B., Nouet, J., Barnola, J.M., Chappellaz, J., Fischer, H., Gallet, J.C., Johnsen, S., Leuenberger, M., Loulergue, L., Luethi, D., Oerter, H., Parrenin, F., Raisbeck, G., Raynaud, D., Schilt, A., Schwander, J., Selmo, E., Souchez, R., Spahni, R., Stauffer, B., Steffensen, J.P., Stenni, B., Stocker, T.F., Tison, J.L., Werner, M., Wolff, E.W., 2007. Orbital and millennial Antarctic climate variability over the past 800,000 years. Science 317, 793-796.

Kaplan, M.R., Licht, K.J., Winckler, G., Schaefer, J.M., Bader, N., Mathieson, C., Roberts, M., Kassab, C.M., Schwartz, R., Graly, J.A., 2017. Middle to Late Pleistocene stability of the central East Antarctic Ice Sheet at the head of Law Glacier. Geology 45, 963-966.

Kennett, J., Houtz, R., Andrews, P., Edwards, A., Gostin, V., Hajós, M., Hampton, M., Jenkins, D., Margolis, S., Ovenshine, A., Perch-Nielsen, K., 1975. Cenozoic Paleoceanography in the Southwest Pacific Ocean, Antarctic Glaciation, and the Development of the Circumantarctic Current. Initial Reports of the Deep Sea Drilling Project 29.

Kerr, A., Huybrechts, P., 1999. The response of the East Antarctic ice-sheet to the evolving tectonic configuration of the Transantarctic Mountains. Global Planet Change 23, 213-229.

Kirkbride, M.P., Deline, P., 2013. The formation of supraglacial debris covers by primary dispersal from transverse englacial debris bands. Earth Surface Processes and Landforms 38, 1779-1792.

Klein, J., Giegengack, R., Middleton, R., Sharma, P., Underwood, J.R., Weeks, R.A., 1986. Revealing Histories of Exposure Using In Situ Produced 26Al and 10Be in Libyan Desert Glass. Radiocarbon 28, 547-555.

Kopp, R.E., Horton, R.M., Little, C.M., Mitrovica, J.X., Oppenheimer, M., Rasmussen, D.J., Strauss, B.H., Tebaldi, C., 2014. Probabilistic 21st and 22nd century sea-level projections at a global network of tide-gauge sites. Earth's Future 2, 383-406.

Kowalewski, D.E., Marchant, D.R., Levy, J.S., Head, J.W., 2006. Quantifying low rates of summertime sublimation for buried glacier ice in Beacon Valley, Antarctica. Antarctic Science 18, 421-428.

Kowalewski, D.E., Marchant, D.R., Swanger, K.M., Head, J.W., 2011. Modeling vapor diffusion within cold and dry supraglacial tills of Antarctica: Implications for the preservation of ancient ice. Geomorphology 126, 159-173.

Lal, D., 1991. Cosmic ray labeling of erosion surfaces in situ nuclide production rates and erosion models. Earth and Planetary Science Letters 104, 424-439.

Lal, D., Arnold, J.R., 1985. Tracing quartz through the environment. Journal of Earth System Science 94, 1-5.

Lal, D., Chen, J., 2005. Cosmic ray labeling of erosion surfaces II: Special cases of exposure histories of boulders, soils and beach terraces. Earth and Planetary Science Letters 236, 797-813.

Lal, D., Peters, B., 1967. Cosmic Ray Produced Radioactivity on the Earth. Springer, Berlin, Heidelberg.

LaPrade, K.E., 1984. Climate, geomorphology, and glaciology of the Shackleton Glacier area, Queen Maud Mountains, Transantarctic Mountains, Antarctica, Geology of the Central Transantarctic Mountains, pp. 163-196.

Lavé, J., Avouac, J.P., 2001. Fluvial incision and tectonic uplift across the Himalayas of central Nepal. Journal of Geophysical Research: Solid Earth 106, 26561-26591.

Lawson, D.E., Strasser, J.C., Evenson, E.B., Alley, R.B., Larson, G.J., Arcone, S.A., 1998. Glaciohydraulic supercooling: a freeze-on mechanism to create stratified, debris-rich basal ice: I. Field evidence. J Glaciol 44, 547-562.

Lawver, L.A., Gahagan, L.M., Coffin, M.F., 1992. The Development of Paleoseaways Around Antarctica, in: Kennett, J.P., Warkne, D.A. (Eds.), The Antarctic Paleoenvironment: A Perspective on Global Change: Part One. American Geophysical Union, pp. 7-30.

Lewis, A.R., Marchant, D.R., Ashworth, A.C., Hemming, S.R., Machlus, M.L., 2007. Major middle Miocene global climate change: Evidence from East Antarctica and the Transantarctic Mountains. Geological Society of America Bulletin 119, 1449-1461.

Lifton, N., Sato, T., Dunai, T.J., 2014. Scaling in situ cosmogenic nuclide production rates using analytical approximations to atmospheric cosmic-ray fluxes. Earth and Planetary Science Letters 386, 149-160.

Luckman, B.H., 2007. Periglacial landforms, rock forms/Talus slopes. Encyclopedia of Quaternary Science, 2242-2249.

Mackay, S.L., Marchant, D.R., 2016. Dating buried glacier ice using cosmogenic 3He in surface clasts: Theory and application to Mullins Glacier, Antarctica. Quaternary Science Reviews 140, 75-100.

Marchant, D.R., Denton, G.H., Swisher, C.C., Potter, N., 1996. Late Cenozoic Antarctic paleoclimate reconstructed from volcanic ashes in the Dry Valleys region of southern Victoria Land. Geological Society of America Bulletin 108, 181-194.

Marchant, D.R., Lewis, A.R., Phillips, W.M., Moore, E.J., Souchez, R.A., Denton, G.H., Sugden, D.E., Potter Jr, N., Landis, G.P., 2002. Formation of patterned ground and sublimation till over Miocene glacier ice in Beacon Valley, southern Victoria Land, Antarctica. Geological Society of America Bulletin 114, 718-730.

Marrero, S.M., Hein, A.S., Naylor, M., Attal, M., Shanks, R., Winter, K., Woodward, J., Dunning, S., Westoby, M., Sugden, D., 2018. Controls on subaerial erosion rates in Antarctica. Earth and Planetary Science Letters 501, 56-66.

Mayewski, P.A., 1975. Glacial geology and late Cenozoic history of the Transantarctic Mountains, Antarctica. Institute of Polar Studies, The Ohio State University, 168.

Mayewski, P.A., Goldthwait, R.P., 1986. Glacial events in the Transantarctic Mountains: A record of the East Antarctic ice sheet, Geology of the Central Transantarctic Mountains, pp. 275-324.

McKay, C., Mellon, M.T., Friedmann, E.I., 1998. Soil temperatures and stability of ice-cemented ground in the McMurdo Dry Valleys, Antarctica. Antarct Sci 10, 31-38.

McKay, C.P., 2008. Snow recurrence sets the depth of dry permafrost at high elevations in the McMurdo Dry Valleys of Antarctica. Antarctic Science 21, 89-94.

McKay, R., Naish, T., Carter, L., Riesselman, C., Dunbar, R., Sjunneskog, C., Winter, D., Sangiorgi, F., Warren, C., Pagani, M., Schouten, S., Willmott, V., Levy, R., DeConto, R., Powell, R.D., 2012. Antarctic and Southern Ocean influences on Late Pliocene global cooling. Proc Natl Acad Sci U S A 109, 6423-6428.

McKay, R.M., Barrett, P.J., Levy, R.S., Naish, T.R., Golledge, N.R., Pyne, A., 2016. Antarctic Cenozoic climate history from sedimentary records: ANDRILL and beyond. Philosophical Transactions of the Royal Society A: Mathematical, Physical and Engineering Sciences 374, 20140301.

Mercer, J.H., 1968. Glacial Geology of the Reedy Glacier Area, Antarctica. Geological Society of America Bulletin 79, 471-486.

Mercer, J.H., 1972. Some observations on the glacial geology of the Beardmore Glacier area, in: Adie, R.J. (Ed.), Antarctic Geology and Geophysics. Universitetsforlaget, pp. 427-433.

Mihalcea, C., Mayer, C., Diolaiuti, G., Lambrecht, A., Smiraglia, C., Tartari, G., 2006. Ice ablation and meteorological conditions on the debris-covered area of Baltoro glacier, Karakoram, Pakistan. Ann Glaciol 43, 292-300.

Morgan, D., Miller, E.M., Miranda, E.J., Edwards, K.L., Liu, J.D., Cribb, W., Bergelin, M., Putkonen, J., Balco, G., 2020. Consistent flow patterns of the Argosy glacier determined from the

provenance of glacial till in Ong Valley, Antarctica., GSA 2020 Connect Online. Geological Society of America, Online.

Morgan, D., Putkonen, J., Balco, G., Stone, J., 2010a. Degradation of glacial deposits quantified with cosmogenic nuclides, Quartermain Mountains, Antarctica. Earth Surface Processes and Landforms 36, 217-228.

Morgan, D., Putkonen, J., Balco, G., Stone, J., 2010b. Quantifying regolith erosion rates with cosmogenic nuclides 10Be and 26Al in the McMurdo Dry Valleys, Antarctica. Journal of Geophysical Research 115.

Naish, T.R., Wilson, G.S., 2009. Constraints on the amplitude of Mid-Pliocene (3.6-2.4Ma) eustatic sea-level fluctuations from the New Zealand shallow-marine sediment record. Philos Trans A Math Phys Eng Sci 367, 169-187.

Naish, T.R., Woolfe, K.J., Barrett, P.J., Wilson, G.S., Atkins, C., Bohaty, S.M., Bücker, C.J., Claps, M., Davey, F.J., Dunbar, G.B., Dunn, A.G., Fielding, C.R., Florindo, F., Hannah, M.J., Harwood, D.M., Henrys, S.A., Krissek, L.A., Lavelle, M., Van Der Meer, J., McIntosh, W.C., Niessen, F., Passchier, S., Powell, R.D., Roberts, A.P., Sagnotti, L., Scherer, R.P., Strong, C.P., Talarico, F., Verosub, K.L., Villa, G., Watkins, D.K., Webb, P.-N., Wonik, T., 2001. Orbitally induced oscillations in the East Antarctic ice sheet at the Oligocene/Miocene boundary. Nature 413, 719-723.

Ng, F., Hallet, B., Sletten, R.S., Stone, J.O., 2005. Fast-growing till over ancient ice in Beacon Valley, Antarctica. Geology 33.

Niedermann, S., 2002. Cosmic-Ray-Produced Noble Gases in Terrestrial Rocks: Dating Tools for Surface Processes. Reviews in Mineralogy and Geochemistry 47, 731-784.

Niedermann, S., Graf, T., Marti, K., 1993. Mass Spectrometric Identification of Cosmic-Ray-Produced Neon in Terrestrial Rocks with Multiple Neon Components. Earth and Planetary Science Letters 118, 65-73.

Nishiizumi, K., 2004. Preparation of 26Al AMS standards. Nuclear Instruments and Methods in Physics Research Section B: Beam Interactions with Materials and Atoms 223-224, 388-392.

Nishiizumi, K., Imamura, M., Caffee, M.W., Southon, J.R., Finkel, R.C., McAninch, J., 2007. Absolute calibration of 10Be AMS standards. Nuclear Instruments and Methods in Physics Research Section B: Beam Interactions with Materials and Atoms 258, 403-413.

Nishiizumi, K., Kohl, C.P., Arnold, J.R., Dorn, R., Klein, I., Fink, D., Middleton, R., Lal, D., 1993. Role of in situ cosmogenic nuclides 10Be and 26Al in the study of diverse geomorphic processes. Earth Surface Processes and Landforms 18, 407-425.

Nishiizumi, K., Lal, D., Klein, J., Middleton, R., Arnold, J.R., 1986. Production of 10Be and 26Al by cosmic rays in terrestrial quartz in situ and implications for erosion rates. Nature 319, 134-136.

Noble, T.L., Rohling, E.J., Aitken, A.R.A., Bostock, H.C., Chase, Z., Gomez, N., Jong, L.M., King, M.A., Mackintosh, A.N., McCormack, F.S., McKay, R.M., Menviel, L., Phipps, S.J., Weber, M.E., Fogwill, C.J., Gayen, B., Golledge, N.R., Gwyther, D.E., Hogg, A.M., Martos, Y.M., Pena-Molino, B., Roberts, J., Flierdt, T., Williams, T., 2020. The Sensitivity of the Antarctic Ice Sheet to a Changing Climate: Past, Present, and Future. Reviews of Geophysics 58.

östrem, G., 1959. Ice Melting under a Thin Layer of Moraine, and the Existence of Ice Cores in Moraine Ridges. Geografiska Annaler 41, 228-230.

Pagani, M., Liu, Z., Lariviere, J., Ravelo, A.C., 2010. High Earth-system climate sensitivity determined from Pliocene carbon dioxide concentrations. Nature Geoscience 3, 27-30.

Passchier, S., 2011. Linkages between East Antarctic Ice Sheet extent and Southern Ocean temperatures based on a Pliocene high-resolution record of ice-rafted debris off Prydz Bay, East Antarctica. Paleoceanography 26, n/a-n/a.

Paxman, G.J.G., Jamieson, S.S.R., Hochmuth, K., Gohl, K., Bentley, M.J., Leitchenkov, G., Ferraccioli, F., 2019. Reconstructions of Antarctic topography since the Eocene–Oligocene boundary. Palaeogeography, Palaeoclimatology, Palaeoecology 535, 109346.

Perg, L.A., Anderson, R.S., Finkel, R.C., 2002. Use of a new 10.Be and 26 Al inventory method to date marine terraces, Santa Cruz, California, USA Comme. Geology 30, 1147-1148.

Phillips, W.M., McDonald, E.V., Reneau, S.L., Jane, P., 1998. Dating soils and alluvium with cosmogenic 21Ne depth profiles: case studies from the Pajarito Plateau, New Mexico, USA. Earth and Planetary Science Letters 160, 209-223.

Placzek, C., Granger, D.E., Matmon, A., Quade, J., Ryb, U., 2014. Geomorphic process rates in the central Atacama Desert, Chile: Insights from cosmogenic nuclides and implications for the onset of hyperaridity. American Journal of Science 314, 1462-1512.

Pollard, D., Deconto, R.M., 2009. Modelling West Antarctic ice sheet growth and collapse through the past five million years. Nature 458, 329-332.

Portenga, E.W., Bierman, P.R., 2011. Understanding Earth's eroding surface with 10Be. GSA Today 21, 4-10.

Putkonen, J., Balco, G., Morgan, D., 2008. Slow regolith degradation without creep determined by cosmogenic nuclide measurements in Arena Valley, Antarctica. Quaternary Research 69, 242-249.

Putkonen, J., Swanson, T., 2003. Accuracy of cosmogenic ages for moraines. Quaternary Research 59, 255-261.

Ragettli, S., Bolch, T., Pellicciotti, F., 2016. Heterogeneous glacier thinning patterns over the last 40 years in Langtang Himal, Nepal. The Cryosphere 10, 2075-2097.

Rose, K.C., Ferraccioli, F., Jamieson, S.S.R., Bell, R.E., Corr, H., Creyts, T.T., Braaten, D., Jordan, T.A., Fretwell, P.T., Damaske, D., 2013. Early East Antarctic Ice Sheet growth recorded in the landscape of the Gamburtsev Subglacial Mountains. Earth and Planetary Science Letters 375, 1-12.

Sams, S.E., 2016. Applications of Cosmogenic 21Ne Dating to Glacial Deposits in Antarctica and California. Vanderbilt University.

Scarrow, J.W., Balks, M.R., Almond, P.C., 2014. Three soil chronosequences in recessional glacial deposits near the polar plateau, in the Central Transantarctic Mountains, Antarctica. Antarctic Science 26, 573-583.

Schäfer, J.M., Baur, H., Denton, G.H., Ivy-Ochs, S., Marchant, D.R., Schlüchter, C., Wieler, R., 2000. The oldest ice on Earth in Beacon Valley, Antarctica: new evidence from surface exposure dating. Earth and Planetary Science Letters 179, 91-99.

Schäfer, J.M., Ivy-Ochs, S., Wieler, R., Leya, I., Baur, H., Denton, G.H., Schlüchter, C., 1999. Cosmogenic noble gas studies in the oldest landscape on earth: surface exposure ages of the Dry Valleys, Antarctica. Earth and Planetary Science Letters 167, 215-226.

Schaller, M., Ehlers, T.A., Blum, J.D., Kallenberg, M.A., 2009. Quantifying glacial moraine age, denudation, and soil mixing with cosmogenic nuclide depth profiles. Journal of Geophysical Research 114.

Scherer, R.P., Deconto, R.M., Pollard, D., Alley, R.B., 2016. Windblown Pliocene diatoms and East Antarctic Ice Sheet retreat. Nature Communications 7, 12957.

Schorghofer, N., 2009. Buffering of sublimation loss of subsurface ice by percolating snowmelt: a theoretical analysis. Permafrost and Periglacial Processes 20, 309-313.

Scotese, C.R., Wright, N., 2018. PALEOMAP Paleodigital Elevation Models, (PaleoDEMS) for the Phanerozoic PALEOMAP Project, 2018. PALEOMAP Paleodigital Elevation Models

(PaleoDEMS) for the Phanerozoic PALEOMAP Project.

Seki, O., Foster, G.L., Schmidt, D.N., Mackensen, A., Kawamura, K., Pancost, R.D., 2010. Alkenone and boron-based Pliocene pCO2 records. Earth and Planetary Science Letters 292, 201-211.

Shevenell, A.E., Kennett, J.P., Lea, D.W., 2004. Middle Miocene Southern Ocean cooling and Antarctic cryosphere expansion. Science 305, 1766-1770.

Siame, L., Bellier, O., Braucher, R., Sébrier, M., Cushing, M., Bourlès, D., Hamelin, B., Baroux, E., de Voogd, B., Raisbeck, G., Yiou, F., 2004. Local erosion rates versus active tectonics: cosmic ray exposure modelling in Provence (south-east France). Earth and Planetary Science Letters 220, 345-364.

Sletten, R.S., Hallet, B., Fletcher, R.C., 2003. Resurfacing time of terrestrial surfaces by the formation and maturation of polygonal patterned ground. Journal of Geophysical Research 108.

Spector, P., Balco, G., 2020. Exposure-age data from across Antarctica reveal mid-Miocene establishment of polar desert climate. Geology 49, 91-95.

Spector, P., Stone, J., Balco, G., Hillebrand, T., Thompson, M., Black, T., 2020. Miocene to Pleistocene glacial history of West Antarctica inferred from Nunatak geomorphology and cosmogenic-nuclide measurements on bedrock surfaces. American Journal of Science 320, 637-676.

Spector, P., Stone, J., Cowdery, S.G., Hall, B., Conway, H., Bromley, G., 2017. Rapid early-Holocene deglaciation in the Ross Sea, Antarctica. Geophysical Research Letters 44, 7817-7825.

Spector, P., Stone, J., Pollard, D., Hillebrand, T., Lewis, C., Gombiner, J., 2018. West Antarctic sites for subglacial drilling to test for past ice-sheet collapse. The Cryosphere 12, 2741-2757.

Stone, J., 2004. Extraction of Al and Be from quartz for isotopic analysis. UW Cosmogenic Nuclide Lab Methods and Procedures, 1-8.

Stone, J., Sletten, R.S., Hallet, B., 2000. Old ice, going fast: Cosmogenic isotope measurements on ice beneath the floor of Beacon Valley, Antarctica. Eos Transactions AGU Fall meeting supplement 81.

Stone, J.O., 2000. Air pressure and cosmogenic isotope production. J Geophys Res-Sol Ea 105, 23753-23759.

Stone, J.O., Balco, G.A., Sugden, D.E., Caffee, M.W., Sass, L.C., 3rd, Cowdery, S.G., Siddoway, C., 2003. Holocene deglaciation of Marie Byrd Land, West Antarctica. Science 299, 99-102.

Stone, J.O.H., Evans, J.M., Fifield, L.K., Allan, G.L., Cresswell, R.G., 1998. Cosmogenic Chlorine-36 Production in Calcite by Muons. Geochimica et Cosmochimica Acta 62, 433-454.

Strasky, S., Di Nicola, L., Baroni, C., Salvatore, M.C., Baur, H., Kubik, P.W., Schlüchter, C., Wieler, R., 2008. Surface exposure ages imply multiple low-amplitude Pleistocene variations in East Antarctic Ice Sheet, Ricker Hills, Victoria Land. Antarctic Science 21, 59-69.

Stroeven, A.P., Prentice, M.L., 1997. A case for Sirius Group alpine glaciation at Mount Fleming, South Victoria Land, Antarctica: A case against Pliocene East Antarctic Ice Sheet reduction. Geological Society of America Bulletin 109, 825-840.

Sugden, D.E., Marchant, D.R., Denton, G.H., 1993. The Case for a Stable East Antarctic Ice Sheet: The Background. Geografiska Annaler. Series A, Physical Geography 75, 151.

Sugden, D.E., Marchant, D.R., Potter, N., Souchez, R.A., Denton, G.H., Swisher, C.C., Tison, J.L., 1995. Preservation of Miocene Glacier Ice in East Antarctica. Nature 376, 412-414.

Talarico, F., Ghezzo, C., Kleinschmidt, G., 2022. Chapter 6 - The Antarctic Continent in Gondwana: a perspective from the Ross Embayment and Potential Research Targets for Future Investigations, in: Florindo, F., Siegert, M., Santis, L.D., Naish, T. (Eds.), Antarctic Climate Evolution (Second Edition). Elsevier, Amsterdam, pp. 219-296.

Todd, C., Stone, J., Conway, H., Hall, B., Bromley, G., 2010. Late Quaternary evolution of Reedy Glacier, Antarctica. Quaternary Science Reviews 29, 1328-1341.

Trimble, 2019. Trimble Business Center v5.0 – Processing and Adjusting GNSS Survey Control Networks. Sunnyvale, CA: Author.

USGS, 2016. Divisions of geologic time (ver. 2.0, March 2020), in: Survey, U.S.G. (Ed.), General Information Product, Version 2.0: March 2020; Version 1.0: May 2012 ed, Reston, VA.

Van der Wateren, D., Hindmarsh, R., 1995. Stabilists strike again. Nature 376.

Vermeesch, P., Balco, G., Blard, P.-H., Dunai, T.J., Kober, F., Niedermann, S., Shuster, D.L., Strasky, S., Stuart, F.M., Wieler, R., Zimmermann, L., 2015. Interlaboratory comparison of cosmogenic 21Ne in quartz. Quat Geochronol 26, 20-28.

Webb, P.N., Harwood, D.M., McKelvey, B.C., Mercer, J.H., Stott, L.D., 1984. Cenozoic marine sedimentation and ice-volume variation on the East Antarctic craton. Geology 12.

Willerslev, E., Cappellini, E., Boomsma, W., Nielsen, R., Hebsgaard, M.B., Brand, T.B., Hofreiter, M., Bunce, M., Poinar, H.N., Dahl-Jensen, D., Johnsen, S., Steffensen, J.P., Bennike, O., Schwenninger, J.L., Nathan, R., Armitage, S., de Hoog, C.J., Alfimov, V., Christl, M., Beer, J., Muscheler, R., Barker, J., Sharp, M., Penkman, K.E., Haile, J., Taberlet, P., Gilbert, M.T., Casoli, A., Campani, E., Collins, M.J., 2007. Ancient biomolecules from deep ice cores reveal a forested southern Greenland. Science 317, 111-114.

Wilson, D.S., Pollard, D., Deconto, R.M., Jamieson, S.S.R., Luyendyk, B.P., 2013. Initiation of the West Antarctic Ice Sheet and estimates of total Antarctic ice volume in the earliest Oligocene. Geophysical Research Letters 40, 4305-4309.

Winnick, M.J., Caves, J.K., 2015. Oxygen isotope mass-balance constraints on Pliocene sea level and East Antarctic Ice Sheet stability. Geology 43, 879-882.

Wolkowinsky, A.J., Granger, D.E., 2004. Early Pleistocene incision of the San Juan River, Utah, dated with 26Al and 10Be. Geology 32, 749.

Yamane, M., Yokoyama, Y., Abe-Ouchi, A., Obrochta, S., Saito, F., Moriwaki, K., Matsuzaki, H., 2015. Exposure age and ice-sheet model constraints on Pliocene East Antarctic ice sheet dynamics. Nat Commun 6, 7016.

Yan, Y., Bender, M.L., Brook, E.J., Clifford, H.M., Kemeny, P.C., Kurbatov, A.V., Mackay, S., Mayewski, P.A., Ng, J., Severinghaus, J.P., Higgins, J.A., 2019. Two-million-year-old snapshots of atmospheric gases from Antarctic ice. Nature 574, 663-666.

Yiou, F., Raisbeck, G.M., Klein, J., Middleton, R., 1984. 26Al/10Be in terrestrial impact glasses. Journal of Non-Crystalline Solids 67, 503-509.

Zachos, J.C., Breza, J.R., Wise, S.W., 1992. Early Oligocene ice-sheet expansion on Antarctica: Stable isotope and sedimentological evidence from Kerguelen Plateau, southern Indian Ocean. Geology 20.

Zachos, J.C., Dickens, G.R., Zeebe, R.E., 2008. An early Cenozoic perspective on greenhouse warming and carbon-cycle dynamics. Nature 451, 279-283.

Zachos, J.C., Shackleton, N.J., Revenaugh, J.S., Palike, H., Flower, B.P., 2001. Climate response to orbital forcing across the Oligocene-Miocene boundary. Science 292, 274-278.

APPENDIX A

PROCEDURE FOR DIFFERENTIAL GPS PROCESSING (TRIMBLE)

Processing of all GPS data from 17-OV-GPS is completed using Trimble Business Center (TBC) v5.20 software package provided by UNAVCO.

1. Open new default project and adjust project settings as followed
    a. General Information – provide user information
    b. Coordinate System – UTM 57 S, WGS 1984, EGM96 (Global)
    c. Units – Coordinates – increase decimal precision
    d. Units – GPS Time – Set to UTC
    e. Baseline processing – Quality – adjust acceptance criteria if needed
    f. Leave all other as default setting
2. Import Base station Data
    a. Import all base files, either daily or hourly depending on data available. Hourly data files should provide a slightly higher accuracy than daily when doing high accuracy data processing.
    b. Because only daily base data is available for 2010 and 2011, all boulder data were processed using daily. All 2017 moraine GPS data should be processed using 1Hz1Hr base data.
    c. Before import is complete a Receiver Raw Data Check is necessary
        i. Antenna – Type – Trimble Zephyr Geodetic 2 RoHS
        ii. Antenna – Method – Bottom of antenna mount
        iii. Antenna – Height – 0.07655 m
        iv. Leave the rest as default

d. To merge all imported base file into a single point, go to -> merge point -> then select all base station point to merge and rename point as “BASE”.

e. To add a quality control point -> click on BASE in project explore panel -> Add Coordinate. For Ong Valley Base, insert the following, and click the box to make each a control quality.

    i. Coordinate type: Local

    ii. Latitude: S 83°14’58.80050

    iii. Longitude: E 157°40’17.68870

    iv. Height: 1672.433 m

f. This results in an office entered (Global) point

g. At this point, all base station files have been corrected to a controlled solution and now can be used for baseline processing of all other files from the valley.

3. Import Rover data, similar to steps for base data.

    a. Before import is complete a Receiver Raw Data Check in is necessary

        i. Point – Make following corrections

            1. Delete all data before Dec 9, 2017

            2. Delete: 17OVGPSCAMPB0

            3. Rename: 17OVGPSCAMPB1 -> B0

            4. Delete: 17-OV-GPS-OD3

            5. Rename: ? -> 10OVGPS052017

            6. Rename: 3949348A -> 10OVGPS022017

        ii. Antenna – Type – Zephyr Geodetic (1)

        iii. Antenna – Method – Bottom of antenna mount

        iv. Antenna – Height – use 0.07840 m for boulder data and 2.0 m for pole collected data

        v. Leave the rest as default

4. Process baseline

    a. To process the data, click -> Survey -> Process Baseline

    b. Processing will start automatic

        i. Most moraine data will be flagged or failed, adjust acceptance criteria in project settings to adjust the threshold.

        ii. To generate a processing report, highlight data such that they appear grey to access the report option.

        iii. Examine the report for trouble shooting the processed results.

            1. RMS and DOP values (should be low)

            2. Residuals plot – any obvious outliers or bad satellites?

            3. Tracking Summary – blue and green lines indicate base and rover satellites

        iv. Click “save” if everything looks ok. Individual changes and reprocessing can always be made to a point after completing the Baseline Processing

5. Optimize accuracy for higher precision. Each of these are potential solutions to increase accuracy, but be careful before resulting to these options as it can lower the accuracy as well.

    a. Select processed session -> select Session Editor -> Deselect certain satellites or part of satellite signal, based on the Rinex QC data file obtained by TEQC.

    b. Deselect GLONASS satellites and/or SV satellite if needed

    c. Any other options suggested in the TBCManual.pdf for lowering RMS.

    d. QC of the satellite. The "o" means anti-spoofing is on for L1 C1|P1 L2 P2, which is what you want to see. When the SVs get near the horizon, which is the beginning and end of the tracking of a particular SV, you get "_" and "L", which is "no SV data and below elevation mask" and loss lock. The Ong Valley base have lots of "-" (no data) and some "I" (ionospheric phase slip).

6. Export data as

    a. Excel file, resulting in a table for analysis

    b. GIS Geodatabase file, resulting in a point feature shapefile for ArcGIS.

APPENDIX B

PROCEDURE FOR MORAINE POSITION ANALYSIS (ARCGIS)

Analysis of all processed moraine GPS data from 17-OV-GPS is completed using ArcGIS software package, with license provided by Department of Geography, University of North Dakota.

1. Start ArcGIS ArcMap 10.7.1, and open a new Blank Map.
2. Load Data from OV_G192_GIS.gdb
    a. Geodatabase point feature of GPS points exported from Trimble Business Center.
    b. Satellite raster (WV2_20161228165131_10300100639DA500…)
        i. Obtained from PGC
    c. DEM raster (OngValley_DEM_1m.tif)
        i. Obtained from REMA, by downloading 0.912 m resolution DEM raster and stitched together using ArcMap.
3. Hillshade
    a. Use the Hillshade tool in 3D analysis to create a hillshade model of Ong Valley
4. Georeferencing
    a. Since the underlaying DEM raster contains the elevation data needed for analyzing the GPS data, it is necessary to georeferencing the WV2 satellite image such that they correlate. Some areas experience large offset, and therefore need to be corrected.
    b. Use the *Georeferencing* toolbar.
    c. Create and link recognizable satellite point with that of the DEM, such that the satellite point now matches the DEM.
    d. Resulting file: OngValley_2016DEC_2_Project_Georect
5. Create moraine line feature

a. Create new attribute field “PointToLine” and assign start to end values to each moraine point (1, 2, 3, …)

b. Create new attribute field “Name” and assign moraine and travers names for each point (ex. Moraine1 or Traverse1)

c. Use the *Point to Line* tool to create moraine line features. Use “Name” as Line Field and “PointToLine” as Sort field

d. Resulting file: Ong Valley Moraines

6. 2D Profile model

    a. Create new line feature “Profile_Ong_curve” with Z and M values

    b. Draw a curved line through the center of the valley starting from ice margin and use *Advanced editing* to smooth the line feature. This eliminates edges and error when projecting moraine points onto profile line.

    c. Assign rout direction to profile line

        i. Start editing -> Route editing -> Define line portion -> right click on the line -> click such that the line start is set to 0 m with direction M

    d. Create points of 1 m interval along the profile line “PointToLine” using *Generate Points Along Lines*

    e. Assign elevation value to “PointsToLine” points using *Extract Values to Point* tool.

        i. Be aware that the ID and order might have changed if merged with other tables

    f. Use *Locate Feature Along Route* to assign profile distance.

        i. OBS: set radius to 1m

        ii. Double check data is ok

    g. Resulting file: ProfilePoint_Ong

        i. This point feature now has points with a distance and elevation value ready to be plotted in MatLab.

7. Manually add the laser measured moraine data points onto map.

    a. This is done based on elevation change of the known locations and the moraines, as well as using the DEM and satellite imagery.

8. Projection of Moraines

    a. To find position of moraine points on profile line use *Near* tool in analysis. This adds Near data (distance, X, and Y) to the attribute table.

    b. Export table using *Table to dBASE (Conversion)* and add table to the project

    c. Right click table and select Display Data XY. Assign X, Y and Z fields to the Near_X, Near_Y and elevation data.

    d. This creates a new point feature of all the moraine points projected onto the profile line feature, called "MoraineToProfile"

    e. To find the distance of the of MoraineToProfile points along the profile line us *Locate Feature Along Route*

9. Export data to be used for Matlab plotting

    a. Export data using *Table to Excel* tool

    b. Reorganize data such that table only contains data for plotting

10. Plotting and inferring

    a. Each of the *MoraineToProfile* points are plotted on a 2D profile of Ong Valley

    b. Based on elevation, location, and slope of the moraines, inferred connections between the lateral and end moraines are drawn.

    c. Based on this, new inferred moraine line features were drawn in ArcMap.

APPENDIX C

SUPPLEMENTARY TABLES

Table C. 1 Baseline processing results for all GNSS boulder positions.

Point ID	Year	Processing start time	Processing duration (mm:ss)	Easting (m)	Northing (m)	Elevation (m)	Horizontal precision (m)	Vertical precision (m)
Base				482008.781	758125.094	1490.739		
OV-GPS-01	2010	12/19/2010 9:44:00 PM	0:19:55	482837.646	754995.884	1691.013	0.010	0.035
	2011	12/18/2011 4:23:00 AM	0:41:20	482837.648	754995.886	1691.000	0.004	0.012
	2017	12/14/2017 9:39:00 PM	1:04:00	482837.647	754995.887	1691.020	0.002	0.006
OV-GPS-02	2010	12/20/2010 12:00:00 AM	0:12:45	482962.101	755280.715	1676.501	0.007	0.013
	2011	12/18/2011 3:33:00 AM	0:21:50	482962.101	755280.709	1676.518	0.005	0.017
	2017	12/14/2017 11:47:00 PM	0:12:00	482962.101	755280.716	1676.519	0.010	0.018
OV-GPS-03	2010	12/20/2010 2:24:00 AM	0:15:50	483057.129	755890.786	1643.140	0.010	0.033
	2011	12/18/2011 2:24:00 AM	0:28:40	483057.139	755890.795	1643.115	0.005	0.014
	2017	12/17/2017 10:22:00 PM	0:40:45	483057.135	755890.801	1643.141	0.004	0.013
OV-GPS-04	2010	12/21/2010 1:17:00 AM	0:20:55	482001.071	753283.012	1712.924	0.033	0.092
	2011	12/21/2011 4:35:00 AM	0:24:50	482001.058	753283.006	1712.862	0.034	0.090
	2017	12/12/2017 11:02:00 PM	0:50:00	482001.070	753283.020	1712.873	0.011	0.075
OV-GPS-05	2010	12/22/2010 9:34:00 PM	0:20:05	482194.946	753603.532	1686.092	0.020	0.077
	2011	12/21/2011 3:09:00 AM	0:33:05	482194.951	753603.527	1686.097	0.007	0.024

Table C. 1 Continued

Point ID	Year	Processing start time	Processing duration (mm:ss)	Easting (m)	Northing (m)	Elevation (m)	Horizontal precision (m)	Vertical precision (m)
	2017	12/13/2017 1:44:00 AM	1:02:30	482194.943	753603.531	1686.077	0.005	0.041
OV-GPS-06	2010	12/24/2010 10:45:00 PM	0:18:55	482543.358	757372.984	1558.869	0.007	0.018
	2011	12/18/2011 12:13:00 AM	0:30:30	482543.360	757372.989	1558.849	0.014	0.043
	2017	12/23/2017 3:15:00 AM	0:51:00	482543.323	757373.030	1558.884	0.005	0.029
OV-GPS-07	2010	12/25/2010 12:47:00 AM	0:14:05	482008.806	758125.052	1490.710	0.022	0.092
	2011	12/17/2011 10:56:00 PM	0:24:00	482008.808	758125.038	1490.786	0.026	0.059
	2017	12/23/2017 12:00:00 AM	0:48:00	482008.781	758125.094	1490.739	0.012	0.094
OV-GPS-08	2010	-	-	-	-	-	-	-
	2011	12/21/2011 1:41:00 AM	0:33:40	482565.618	754334.477	1630.146	0.005	0.011
	2017	12/13/2017 3:37:00 AM	0:37:30	482565.610	754334.481	1630.160	0.004	0.010

Table C. 2 Baseline processing covariance matrix results for all GNSS boulder positions.

Point ID	Year	Covariance Matrix					
		σ(xx)	**σ**(xy)	**σ**(yy)	**σ**(xz)	**σ**(yz)	**σ**(zz)
OV-GPS-01	2010	0.0000246315	0.0000087433	0.0000059127	0.0000731356	0.0000312394	0.0003051864
	2011	0.0000026582	0.0000006590	0.0000015680	0.0000042146	0.0000018509	0.0000394395
	2017	0.0000006607	0.0000003088	0.0000006593	0.0000001932	-0.0000003261	0.0000102498
OV-GPS-02	2010	0.0000067744	0.0000017804	0.0000030857	0.0000022649	0.0000027485	0.0000444341
	2011	0.0000026061	0.0000014530	0.0000037686	0.0000003198	0.0000075424	0.0000741768
	2017	0.0000061640	0.0000046111	0.0000155654	0.0000088257	0.0000191932	0.0000815296
OV-GPS-03	2010	0.0000197327	0.0000034350	0.0000119445	0.0000253520	0.0000167773	0.0002868958
	2011	0.0000043395	0.0000009610	0.0000020766	0.0000034664	0.0000034072	0.0000492615
	2017	0.0000024667	0.0000009711	0.0000021858	0.0000032051	0.0000013054	0.0000409267
OV-GPS-04	2010	0.0001351362	0.0000790033	0.0001176150	0.0002472433	0.0002906781	0.0021823510
	2011	0.0001786672	0.0000735460	0.0001103286	0.0002565650	0.0001700138	0.0020952665
	2017	0.0000219830	0.0000035740	0.0000166494	0.0001123201	-0.0000227500	0.0014745537
OV-GPS-05	2010	0.0001002938	0.0000323125	0.0000227381	0.0003287757	0.0001326732	0.0015089159
	2011	0.0000045217	0.0000018303	0.0000058503	0.0000027086	0.0000154144	0.0001528761
	2017	0.0000028894	0.0000000370	0.0000030866	0.0000157297	-0.0000130141	0.0004467727
OV-GPS-06	2010	0.0000061323	0.0000014229	0.0000070327	0.0000019103	-0.0000052597	0.0000842408
	2011	0.0000282290	0.0000127402	0.0000225874	0.0000625667	0.0000432303	0.0004764645
	2017	0.0000049017	0.0000001357	0.0000028528	0.0000217646	-0.0000061346	0.0002124623
OV-GPS-07	2010	0.0000782409	0.0000374822	0.0000492267	0.0002693668	0.0001786899	0.0021900968
	2011	0.0001041985	0.0000267663	0.0000523180	0.0000411073	0.0000560438	0.0009092484
	2017	0.0000325577	-0.0000085403	0.0000278394	0.0001992557	-0.0001803713	0.0022495768
OV-GPS-08	2010	-	-	-	-	-	-
	2011	0.0000046359	0.0000014562	0.0000020128	0.0000048165	0.0000031349	0.0000336287
	2017	0.0000021856	0.0000010116	0.0000018187	0.0000030657	0.0000026031	0.0000258067

Table C. 3 Be isotope measurements for samples from Ong Valley "OD1" core site.

Sample Name	Quartz Mass (g)	Mass of ^{9}Be Added (μg)*	Uncorrected ^{10}Be/^{9}Be Ratio**	Uncorrected ^{10}Be/^{9}Be Ratio Uncertainty**	Background-Corrected ^{10}Be Atoms	Background-Corrected ^{10}Be Atoms Uncertainty	^{10}Be Concentration (atoms g^{-1})	^{10}Be Concentration Uncertainty (atoms g^{-1})
Pit2-6-14	20.6733	241.9	1.718E-11	1.077E-13	2.78E+08	1.74E+06	1.343E+07	8.42E+04
Pit2-14-17	21.9411	241.9	1.834E-11	1.153E-13	2.96E+08	1.86E+06	1.351E+07	8.50E+04
Pit2-23-29	21.8446	241.7	1.740E-11	1.087E-13	2.81E+08	1.76E+06	1.287E+07	8.04E+04
Pit2-37-43	12.7551	241.7	9.157E-12	5.539E-14	1.48E+08	8.95E+05	1.159E+07	7.01E+04
Pit2-43-50	18.8236	241.5	7.746E-12	6.924E-14	1.25E+08	1.12E+06	6.639E+06	5.94E+04
Pit2-56-62	12.6866	241.0	3.346E-12	4.113E-14	5.39E+07	6.63E+05	4.246E+06	5.22E+04
C1-5-36	1.8134	241.7	8.049E-14	2.014E-15	1.29E+06	3.70E+04	7.087E+05	2.04E+04
C1-36-48	2.2931	241.7	8.221E-14	1.603E-15	1.31E+06	3.13E+04	5.726E+05	1.37E+04
C1-48-70	2.5156	240.5	9.058E-14	1.772E-15	1.44E+06	3.34E+04	5.726E+05	1.33E+04
C1-70-100	1.5451	240.5	1.412E-13	2.623E-15	2.25E+06	4.56E+04	1.459E+06	2.95E+04
C1-107-125	11.1057	241.6	7.567E-13	6.720E-15	1.22E+07	1.10E+05	1.096E+06	9.90E+03
C1-125-145	5.7661	242.1	3.130E-13	5.806E-15	5.02E+06	9.55E+04	8.711E+05	1.66E+04
C1-185-235	2.6553	241.0	5.004E-14	1.265E-15	7.66E+05	2.69E+04	2.885E+05	1.01E+04
C1-235-310	2.5860	240.6	2.826E-14	9.519E-16	4.15E+05	2.33E+04	1.603E+05	9.00E+03
C1-310-350	5.2484	241.1	4.029E-14	1.128E-15	6.09E+05	2.53E+04	1.161E+05	4.82E+03
C1-500-582	7.8121	240.9	7.423E-14	1.658E-15	1.16E+06	3.19E+04	1.479E+05	4.09E+03
C1-582-649	10.4209	241.1	8.806E-14	1.771E-15	1.38E+06	3.35E+04	1.323E+05	3.22E+03
C1-781-819	10.4503	241.3	2.736E-13	5.136E-15	4.37E+06	8.47E+04	4.184E+05	8.10E+03
C1-819-879	20.0278	240.2	6.463E-13	1.206E-14	1.03E+07	1.94E+05	5.160E+05	9.70E+03
C1-879-944	16.5967	239.7	5.015E-13	9.392E-15	7.99E+06	1.51E+05	4.816E+05	9.12E+03

*^{9}Be was added through a beryl carrier made at University of Vermont with a concentration of 291 μg mL^{-1}.

**Isotopic analysis was conducted at Lawrence Livermore National Laboratory; ratios were normalized against standard 07KNSTD3110 with an assumed ratio of 2850 x 10^{-15} (Nishiizumi et al., 2007).

Table C. 4 Al isotope measurements for samples from Ong Valley "OD1" core site.

Sample Name	Quartz Mass (g)	Total ^{27}Al Quantified by ICP-OES (μg)*	Uncorrected ^{26}Al/^{27}Al Ratio**	Uncorrected ^{26}Al/^{27}Al Ratio Uncertainty**	Background-Corrected ^{26}Al Atoms	Background-Corrected ^{26}Al Atoms Uncertainty	^{26}Al Concentration (atoms g^{-1})	^{26}Al Concentration Uncertainty (atoms g^{-1})
Pit2-6-14	20.6733	1809	3.474E-11	6.190E-13	1.403E+09	2.500E+07	6.784E+07	1.209E+06
Pit2-14-17	21.9411	1925	3.439E-11	7.185E-13	1.477E+09	3.087E+07	6.732E+07	1.407E+06
Pit2-23-29	21.8446	1724	3.602E-11	7.572E-13	1.386E+09	2.914E+07	6.343E+07	1.334E+06
Pit2-37-43	12.7551	1764	1.886E-11	3.857E-13	7.422E+08	1.518E+07	5.819E+07	1.190E+06
Pit2-43-50	18.8236	1473	2.038E-11	4.213E-13	6.699E+08	1.385E+07	3.559E+07	7.360E+05
Pit2-56-62	12.6866	1634	8.118E-12	1.842E-13	2.959E+08	6.720E+06	2.332E+07	5.297E+05
C1-5-36	1.8134	1587	2.343E-13	9.654E-15	8.040E+06	3.796E+05	4.434E+06	2.094E+05
C1-36-48	2.2931	1617	2.257E-13	8.082E-15	7.884E+06	3.367E+05	3.438E+06	1.468E+05
C1-48-70	2.5156	1683	2.057E-13	8.721E-15	7.469E+06	3.715E+05	2.969E+06	1.477E+05
C1-70-100	1.5451	1594	1.908E-13	8.114E-15	6.528E+06	3.329E+05	4.225E+06	2.154E+05
C1-107-125	11.1057	2116	7.839E-13	1.972E-14	3.699E+07	9.573E+05	3.331E+06	8.620E+04
C1-125-145	5.7661	1856	3.946E-13	1.355E-14	1.631E+07	5.937E+05	2.828E+06	1.030E+05
C1-185-235	2.6553	1644	1.082E-13	7.706E-15	3.933E+06	3.305E+05	1.481E+06	1.245E+05
C1-235-310	2.5860	1619	8.500E-14	5.489E-15	3.035E+06	2.603E+05	1.174E+06	1.006E+05
C1-310-350	5.2484	1689	1.166E-13	6.087E-15	4.359E+06	2.890E+05	8.306E+05	5.506E+04
C1-500-582	7.8121	1816	8.764E-14	6.059E-15	3.517E+06	3.099E+05	4.501E+05	3.967E+04
C1-582-649	10.4209	1978	9.747E-14	5.866E-15	4.267E+06	3.308E+05	4.095E+05	3.175E+04
C1-781-819	10.4503	1887	1.222E-13	6.979E-15	5.110E+06	3.534E+05	4.890E+05	3.382E+04
C1-819-879	20.0278	2493	1.769E-13	9.947E-15	9.808E+06	6.112E+05	4.897E+05	3.052E+04
C1-879-944	16.5967	2144	1.640E-13	1.231E-14	7.812E+06	6.299E+05	4.707E+05	3.795E+04

*^{27}Al was added only to samples with insufficient total Al through commercial SPEX ICP standard with a concentration of 1000 μg mL^{-1}. The total here reflects the sum of Al added through carrier and native Al in quartz.

**Isotopic analysis was conducted at PRIME Laboratory; ratios were normalized against standard KNSTD with an assumed ratio of 1.818 x 10^{-12} (Nishiizumi et al., 2004).

Table C. 5 Step-degassing Ne isotope measurements for samples from Ong Valley surface of supraglacial debris at OD1 drill site. Run on BGC "Ohio" system, September 2019.

Sample name	Aliquot	Aliquot weight (g)	Heating temp. (deg C)	Heating time (hr)	Total ^{20}Ne released[1] (10^9 atoms)	Total ^{21}Ne released[2] (10^6 atoms)	Total ^{22}Ne released[3] (10^6 atoms)	^{21}Ne/^{20}Ne[4] (10^{-3})	^{22}Ne/^{20}Ne[4] (10^{-3})	Excess ^{21}Ne This heating step (10^6 atoms g^{-1})	Excess ^{21}Ne as % of ^{21}Ne released in this heating step	Percent of total excess ^{21}Ne released in this step	Total excess ^{21}Ne (10^6 atoms g^{-1})
17-OD1-SURF1	a	0.1745	850	0.25	0.61 ± 0.027	23.58 ± 0.77	86.8 ± 3.3	38.4 ± 1.1	141.8 ± 4.5	124.8 ± 4.5	92	99	125.4 ± 4.5
			1100	0.25	0.046 ± 0.011	0.25 ± 0.039	4.2 ± 1.1	5.4 ± 1.5	91 ± 31	0.65 ± 0.29	46	1	
17-OD1-SURF2	a	0.1621	850	0.25	0.848 ± 0.031	22.93 ± 0.74	109.6 ± 3.9	26.82 ± 0.44	128.7 ± 2.3	125.9 ± 4.6	89	99	127.3 ± 4.6
			1100	0.25	0.083 ± 0.01	0.456 ± 0.043	8.8 ± 1.1	5.49 ± 0.77	106.0 ± 17.6	1.30 ± 0.32	46	1	
17-OD1-SURF3	a	0.1719	850	0.25	0.537 ± 0.021	25.73 ± 0.8	81.9 ± 3.0	47.6 ± 0.96	152.0 ± 3.7	140.5 ± 4.7	94	99	141.4 ± 4.7
			1100	0.25	0.0378 ± 0.0093	0.273 ± 0.037	4.0 ± 1.1	7.2 ± 1.9	105 ± 38	0.94 ± 0.27	59	1	
17-OD1-SURF4	a	0.1737	850	0.25	0.651 ± 0.025	24.18 ± 0.75	92.0 ± 3.4	36.9 ± 0.6	140.8 ± 3.0	128.1 ± 4.4	92	100	128.5 ± 4.4
			1100	0.25	0.0519 ± 0.0089	0.225 ± 0.038	5.6 ± 1.2	4.3 ± 1.0	108 ± 28	0.41 ± 0.26	32	0	

[1] Computed by comparison to ^{20}Ne signal in air standards. 1-sigma uncertainty includes measurement uncertainty of ^{20}Ne signal in this analysis and the reproducibility of the air standards

[2] Computed by comparison to ^{21}Ne signal in air standards. 1-sigma uncertainty includes measurement uncertainty of ^{21}Ne signal in this analysis and the reproducibility of the air standards

[3] Computed by comparison to ^{22}Ne signal in air standards. 1-sigma uncertainty includes measurement uncertainty of ^{22}Ne signal in this analysis and the reproducibility of the air standards

[4] Isotope ratio measured internally during each analysis and corrected for mass discrimination based on an air standard. Does not involve normalization to the Ne isotope signals in the standards, so the ratio computed from absolute Ne isotope amounts in previous columns may differ within uncertainty.

Table C. 6 Step-degassing Ne isotope measurements for samples from Ong Valley "OD1" core site. Run on BGC "Ohio" system, October-November 2018. Note: "n.d" = not detected.

Sample name	Aliquot	Aliquot weight (g)	Heating temp. (deg C)	Heating time (hr)	Total ^{20}Ne released[1] (10^9 atoms)	Total ^{21}Ne released[2] (10^6 atoms)	Total ^{22}Ne released[3] (10^6 atoms)	^{21}Ne / ^{20}Ne[4] (10^{-3})	^{22}Ne / ^{20}Ne[4] (10^{-3})	Excess ^{21}Ne this heating step (10^6 atoms g^{-1})	Excess ^{21}Ne as % of ^{21}Ne released in this heating step	Percent of total excess ^{21}Ne released in this step	Total excess ^{21}Ne (10^6 atoms g^{-1})
1. Aliquots of CRONUS-A quartz standard run together with samples													
CRONUS A 201810	a	0.1454	850	0.25	1.799 ± 0.028	50.50 ± 0.99	234.2 ± 5.3	27.54 ± 0.27	130.3 ± 2.4	304.9 ± 5.0	88	98	310.1 ± 5.0
			1100	0.25	0.193 ± 0.010	1.346 ± 0.096	20.3 ± 3.7	6.87 ± 0.58	106 ± 20	5.19 ± 0.66	56	2	
	b	0.0968	850	0.25	1.277 ± 0.021	33.75 ± 0.70	168.9 ± 4.9	25.95 ± 0.34	132.4 ± 3.4	303.9 ± 5.5	87	98	310.6 ± 5.6
			1100	0.25	0.1520 ± 0.0094	1.12 ± 0.11	16.9 ± 3.8	7.21 ± 0.79	111 ± 25	6.7 ± 1.1	58	2	
	c	0.0394	850	0.25	0.548 ± 0.014	13.99 ± 0.34	71.8 ± 3.9	25.08 ± 0.66	131.3 ± 7.2	308.2 ± 7.1	87	91	336.9 ± 7.8
			1100	0.25	0.124 ± 0.010	1.52 ± 0.13	13.9 ± 3.9	12.1 ± 1.4	113 ± 32	28.7 ± 3.1	74	9	
	d	0.1395	850	0.25	1.976 ± 0.047	48.61 ± 1.65	249.6 ± 8.9	24.36 ± 0.25	125.8 ± 3.4	303.8 ± 7.5	87	98	310.7 ± 7.5
			1100	0.25	0.1320 ± 0.0093	1.37 ± 0.12	14.3 ± 6.8	10.2 ± 1.1	108 ± 51	6.90 ± 0.81	70	2	
	e	0.122	850	0.25	1.616 ± 0.022	42.71 ± 0.62	210.2 ± 5.6	25.99 ± 0.40	129.9 ± 3.6	305.8 ± 4.0	87	98	310.5 ± 4.1
			1100	0.25	0.127 ± 0.010	0.95 ± 0.11	14.2 ± 5.4	7.41 ± 0.99	112 ± 42	4.66 ± 0.89	60	2	
	f	0.1597	850	0.25	2.071 ± 0.036	55.80 ± 0.94	269.9 ± 6.3	26.53 ± 0.27	129.4 ± 2.8	306.4 ± 5.3	88	97	314.5 ± 5.4

Table C. 6 Continued

Sample name	Aliquot	Aliquot weight (g)	Heating temp. (deg C)	Heating time (hr)	Total ^{20}Ne released[1] (10^9 atoms)	Total ^{21}Ne released[2] (10^6 atoms)	Total ^{22}Ne released[3] (10^6 atoms)	^{21}Ne / ^{20}Ne[4] (10^{-3})	^{22}Ne / ^{20}Ne[4] (10^{-3})	Excess ^{21}Ne this heating step (10^6 atoms g^{-1})	Excess ^{21}Ne as % of ^{21}Ne released in this heating step	Percent of total excess ^{21}Ne released in this step	Total excess ^{21}Ne (10^6 atoms g^{-1})
			1100	0.25	0.159 ± 0.010	1.78 ± 0.12	19.8 ± 5.8	11.03 ± 0.97	125 ± 36	8.03 ± 0.72	72	3	
	g	0.147	850	0.25	2.263 ± 0.035	52.06 ± 0.85	282.4 ± 6.4	22.85 ± 0.22	124.5 ± 2.3	306.9 ± 5.3	87	98	313.5 ± 5.3
			1100	0.25	0.1591 ± 0.0063	1.46 ± 0.11	20.3 ± 5.2	9.06 ± 0.75	127 ± 32	6.62 ± 0.75	67	2	
	h	0.1668	850	0.25	2.414 ± 0.036	57.01 ± 0.80	308.2 ± 6.8	23.39 ± 0.20	127.5 ± 2.2	296.5 ± 4.9	87	96	307.3 ± 5.0
			1100	0.25	0.2485 ± 0.0072	2.57 ± 0.13	28.3 ± 5.3	10.20 ± 0.57	114 ± 21	10.81 ± 0.79	70	4	
2. Samples of unconsolidated supraglacial debris overlying ice													
17-OD1-PIT2-6-14	a	0.1525	850	0.25	0.668 ± 0.014	19.47 ± 0.53	89.5 ± 6.4	28.44 ± 0.59	132.5 ± 9.3	111.9 ± 2.0	88	99	113.5 ± 2.1
			1100	0.25	0.074 ± 0.010	0.471 ± 0.090	8.3 ± 5.8	6.2 ± 1.4	111 ± 77	1.58 ± 0.60	51	1	
	b	0.1573	850	0.25	0.698 ± 0.011	18.60 ± 0.33	89.9 ± 5.4	26.48 ± 0.51	128.0 ± 7.7	104.7 ± 1.6	89	100	104.7 ± 1.6
			1100	0.25	0.0558 ± 0.0093	0.105 ± 0.084	7.9 ± 5.4	1.9 ± 1.5	139 ± 96	n.d	0	0	
17-OD1-PIT2-14-17	a	0.1427	850	0.25	0.698 ± 0.013	17.49 ± 0.46	91.0 ± 6.3	24.43 ± 0.42	129.0 ± 8.7	105.3 ± 1.8	86	100	105.3 ± 1.8
			1100	0.25	0.053 ± 0.011	0.231 ± 0.088	6.2 ± 5.8	4.3 ± 1.8	118 ± 109	n.d	0	0	
	b	0.1584	850	0.25	0.747 ± 0.013	17.93 ± 0.33	93.9 ± 5.4	23.87 ± 0.51	125.1 ± 7.3	98.8 ± 1.7	87	100	98.8 ± 1.7
			1100	0.25	0.030 ± 0.010	0.157 ± 0.080	3.8 ± 5.4	5.2 ± 3.1	126 ± 178	n.d	0	0	

Table C. 6 Continued

Sample name	Aliquot	Aliquot weight (g)	Heating temp. (deg C)	Heating time (hr)	Total ^{20}Ne released[1] (10^9 atoms)	Total ^{21}Ne released[2] (10^6 atoms)	Total ^{22}Ne released[3] (10^6 atoms)	^{21}Ne / ^{20}Ne[4] (10^{-3})	^{22}Ne / ^{20}Ne[4] (10^{-3})	Excess ^{21}Ne this heating step (10^6 atoms g^{-1})	Excess ^{21}Ne as % of ^{21}Ne released in this heating step	Percent of total excess ^{21}Ne released in this step	Total excess ^{21}Ne (10^6 atoms g^{-1})
17-OD1-PIT2-23-29	a	0.1542	850	0.25	0.823 ± 0.014	19.59 ± 0.51	105.2 ± 6.4	23.15 ± 0.40	126.3 ± 7.4	108.0 ± 2.0	85	99	109.1 ± 2.0
			1100	0.25	0.061 ± 0.010	0.354 ± 0.094	8.8 ± 5.7	5.6 ± 1.7	143 ± 93	1.06 ± 0.61	46	1	
	b	0.1696	850	0.25	0.922 ± 0.016	19.56 ± 0.34	112.2 ± 5.5	21.06 ± 0.43	120.9 ± 6.0	98.7 ± 1.6	86	98	100.8 ± 1.7
			1100	0.25	0.100 ± 0.010	0.67 ± 0.10	12.7 ± 5.4	6.6 ± 1.2	125 ± 53	2.15 ± 0.60	55	2	
17-OD1-PIT2-37-43	a	0.1527	850	0.25	0.415 ± 0.010	15.15 ± 0.43	61.6 ± 6.1	35.47 ± 0.96	147 ± 14	88.6 ± 1.9	89	100	88.6 ± 1.9
			1100	0.25	0.0282 ± 0.0092	0.171 ± 0.086	6.1 ± 5.7	5.9 ± 3.5	215 ± 208	n.d	0	0	
	b	0.1567	850	0.25	0.418 ± 0.011	15.98 ± 0.28	61.5 ± 5.6	37.95 ± 1.05	146 ± 13	93.6 ± 1.4	92	99	94.7 ± 1.5
			1100	0.25	0.042 ± 0.010	0.304 ± 0.091	4.4 ± 5.6	7.1 ± 2.6	103 ± 130	1.12 ± 0.59	58	1	
17-OD1-PIT2-43-50	a	0.1661	850	0.25	0.742 ± 0.014	11.32 ± 0.34	85.4 ± 6.2	14.84 ± 0.35	113.6 ± 8.0	53.2 ± 1.4	78	100	53.2 ± 1.4
			1100	0.25	0.0783 ± 0.0093	0.316 ± 0.084	7.6 ± 5.7	3.9 ± 1.1	97 ± 71	n.d	0	0	
	b	0.1623	850	0.25	0.723 ± 0.011	11.31 ± 0.25	83.4 ± 5.7	15.53 ± 0.37	114.6 ± 7.8	56.1 ± 1.4	81	98	57.1 ± 1.5
			1100	0.25	0.050 ± 0.010	0.312 ± 0.089	7.3 ± 5.4	6.2 ± 2.2	144 ± 108	0.99 ± 0.57	51	2	
17-OD1-PIT2-56-62	a	0.1621	850	0.25	0.532 ± 0.012	7.52 ± 0.23	60.9 ± 6.1	13.74 ± 0.37	113 ± 11	35.5 ± 1.0	76	98	36.3 ± 1.2
			1100	0.25	0.0506 ± 0.0092	0.300 ± 0.093	5.4 ± 5.6	5.8 ± 2.0	107 ± 109	0.87 ± 0.57	47	2	
	b	0.1581	850	0.25	0.489 ± 0.012	6.56 ± 0.21	55.6 ± 5.6	13.30 ± 0.48	113 ± 11	32.1 ± 1.2	77	98	32.8 ± 1.3

Table C. 6 Continued

Sample name	Aliquot	Aliquot weight (g)	Heating temp. (deg C)	Heating time (hr)	Total ^{20}Ne released[1] (10^9 atoms)	Total ^{21}Ne released[2] (10^6 atoms)	Total ^{22}Ne released[3] (10^6 atoms)	^{21}Ne / ^{20}Ne[4] (10^{-3})	^{22}Ne / ^{20}Ne[4] (10^{-3})	Excess ^{21}Ne this heating step (10^6 atoms g^{-1})	Excess ^{21}Ne as % of ^{21}Ne released in this heating step	Percent of total excess ^{21}Ne released in this step	Total excess ^{21}Ne (10^6 atoms g^{-1})
			1100	0.25	0.026 ± 0.010	0.201 ± 0.082	6.4 ± 5.3	7.6 ± 4.1	241 ± 213	0.76 ± 0.53	60	2	
3. Samples of sediment extracted from ice core													
17-OD1-C1-5-36	a	0.1304	850	0.25	1.058 ± 0.013	4.74 ± 0.15	110.5 ± 5.6	4.41 ± 0.14	104.3 ± 5.3	11.8 ± 1.1	32	94	12.5 ± 1.3
			1100	0.25	0.090 ± 0.010	0.362 ± 0.090	10.0 ± 5.4	4.0 ± 1.1	111 ± 60	0.72 ± 0.72	26	6	
	b	0.1643	850	0.25	1.109 ± 0.013	5.03 ± 0.16	115.4 ± 5.5	4.49 ± 0.14	103.2 ± 4.8	10.38 ± 0.90	34	100	10.38 ± 0.90
			1100	0.25	0.109 ± 0.010	0.383 ± 0.096	13.0 ± 5.5	3.44 ± 0.90	117 ± 49	n.d	0	0	
17-OD1-C1-36-48	a	0.1521	850	0.25	1.697 ± 0.018	6.50 ± 0.17	178.5 ± 5.8	3.768 ± 0.090	105.1 ± 3.4	9.04 ± 0.99	21	71	12.8 ± 1.2
			1100	0.25	0.165 ± 0.010	1.070 ± 0.091	17.1 ± 5.3	6.44 ± 0.65	103 ± 32	3.78 ± 0.62	54	29	
	b	0.1629	850	0.25	1.419 ± 0.011	5.69 ± 0.16	143.9 ± 5.2	4.03 ± 0.11	101.3 ± 3.5	9.36 ± 0.96	27	80	11.6 ± 1.1
			1100	0.25	0.1766 ± 0.0055	0.904 ± 0.081	17.6 ± 5.6	5.05 ± 0.47	100 ± 31	2.27 ± 0.49	41	20	
17-OD1-C1-48-70	a	0.1615	850	0.25	1.303 ± 0.014	5.81 ± 0.21	137.0 ± 5.8	4.39 ± 0.15	105.0 ± 4.4	11.5 ± 1.2	32	92	12.5 ± 1.4
			1100	0.25	0.102 ± 0.010	0.46 ± 0.10	11.3 ± 5.4	4.5 ± 1.1	112 ± 53	0.95 ± 0.64	34	8	
	b	0.1458	850	0.25	1.320 ± 0.013	5.90 ± 0.17	137.0 ± 5.3	4.49 ± 0.13	103.7 ± 3.9	13.9 ± 1.2	34	84	16.5 ± 1.3
			1100	0.25	0.1311 ± 0.0054	0.771 ± 0.097	15.0 ± 5.1	5.81 ± 0.76	114 ± 38	2.56 ± 0.66	48	16	

Table C. 6 Continued

Sample name	Aliquot	Aliquot weight (g)	Heating temp. (deg C)	Heating time (hr)	Total ^{20}Ne released[1] (10^9 atoms)	Total ^{21}Ne released[2] (10^6 atoms)	Total ^{22}Ne released[3] (10^6 atoms)	^{21}Ne / ^{20}Ne[4] (10^{-3})	^{22}Ne / ^{20}Ne[4] (10^{-3})	Excess ^{21}Ne this heating step (10^6 atoms g^{-1})	Excess ^{21}Ne as % of ^{21}Ne released in this heating step	Percent of total excess ^{21}Ne released in this step	Total excess ^{21}Ne (10^6 atoms g^{-1})
	c	0.1347	850	0.25	1.181 ± 0.014	4.99 ± 0.15	122.3 ± 5.0	4.08 ± 0.12	100.4 ± 4.1	9.8 ± 1.0	27	91	10.8 ± 1.2
			1100	0.25	0.0660 ± 0.0051	0.339 ± 0.077	5.9 ± 4.6	5.0 ± 1.2	87 ± 69	0.99 ± 0.57	39	9	
17-OD1-C1-70-100	a	0.1433	850	0.25	0.991 ± 0.013	8.62 ± 0.22	109.6 ± 5.7	8.57 ± 0.22	110.6 ± 5.7	38.9 ± 1.4	65	98	39.8 ± 1.5
			1100	0.25	0.078 ± 0.011	0.364 ± 0.088	11.8 ± 5.4	4.7 ± 1.3	153 ± 71	0.93 ± 0.65	37	2	
	b	0.1598	850	0.25	0.9952 ± 0.0072	8.97 ± 0.18	107.7 ± 5.1	9.07 ± 0.17	108.1 ± 5.0	38.1 ± 1.0	68	96	39.9 ± 1.1
			1100	0.25	0.0892 ± 0.0071	0.551 ± 0.073	8.0 ± 5.3	6.11 ± 0.93	89 ± 57	1.76 ± 0.47	51	4	
17-OD1-C1-107-125	a	0.1606	850	0.25	1.174 ± 0.018	9.02 ± 0.20	123.8 ± 5.8	7.57 ± 0.18	105.5 ± 5.0	33.8 ± 1.1	60	100	33.8 ± 1.1
			1100	0.25	0.101 ± 0.011	0.272 ± 0.087	11.2 ± 5.6	2.68 ± 0.89	112 ± 55	n.d	0	0	
	b	0.148	850	0.25	1.279 ± 0.010	9.76 ± 0.21	136.6 ± 5.2	7.67 ± 0.16	106.7 ± 3.9	40.8 ± 1.3	62	93	44.1 ± 1.4
			1100	0.25	0.1076 ± 0.0054	0.804 ± 0.085	13.5 ± 5.1	7.40 ± 0.85	125 ± 46	3.24 ± 0.57	60	7	
	c	0.1625	850	0.25	1.185 ± 0.013	9.38 ± 0.23	129.7 ± 5.0	7.63 ± 0.16	106.0 ± 4.1	34.1 ± 1.2	59	100	34.1 ± 1.2
			1100	0.25	0.1268 ± 0.0055	0.348 ± 0.076	12.8 ± 4.7	2.66 ± 0.59	99 ± 36	n.d	0	0	
17-OD1-C1-125-145	a	0.164	850	0.25	1.148 ± 0.014	8.13 ± 0.20	121.1 ± 6.0	6.98 ± 0.16	105.5 ± 5.2	28.2 ± 1.1	57	96	29.5 ± 1.2
			1100	0.25	0.1117 ± 0.0094	0.546 ± 0.096	13.8 ± 5.4	4.86 ± 0.93	123 ± 48	1.30 ± 0.60	39	4	
	b	0.1471	850	0.25	0.9372 ± 0.0092	7.33 ± 0.19	103.1 ± 5.1	7.87 ± 0.20	109.9 ± 5.3	31.4 ± 1.2	63	94	33.2 ± 1.3

Table C. 6 Continued

Sample name	Aliquot	Aliquot weight (g)	Heating temp. (deg C)	Heating time (hr)	Total ^{20}Ne released[1] (10^9 atoms)	Total ^{21}Ne released[2] (10^6 atoms)	Total ^{22}Ne released[3] (10^6 atoms)	^{21}Ne / ^{20}Ne[4] (10^{-3})	^{22}Ne / ^{20}Ne[4] (10^{-3})	Excess ^{21}Ne this heating step (10^6 atoms g^{-1})	Excess ^{21}Ne as % of ^{21}Ne released in this heating step	Percent of total excess ^{21}Ne released in this step	Total excess ^{21}Ne (10^6 atoms g^{-1})
			1100	0.25	0.0782 ± 0.0050	0.51 ± 0.08	9.4 ± 5.1	6.4 ± 1.1	120 ± 64	1.85 ± 0.54	54	6	
	c	0.1539	850	0.25	0.900 ± 0.014	7.17 ± 0.19	100.8 ± 4.9	7.68 ± 0.20	108.6 ± 5.4	27.7 ± 1.1	59	97	28.4 ± 1.2
			1100	0.25	0.0929 ± 0.0058	0.399 ± 0.081	10.2 ± 4.8	4.16 ± 0.89	107 ± 51	0.73 ± 0.52	28	3	
17-OD1-C1-185-235	a	0.1532	850	0.25	0.765 ± 0.012	4.34 ± 0.15	79.5 ± 5.6	5.59 ± 0.19	103.9 ± 7.3	13.19 ± 0.91	47	100	13.19 ± 0.91
			1100	0.25	0.0579 ± 0.0093	0.073 ± 0.091	5.8 ± 5.4	1.3 ± 1.6	100 ± 92	n.d	0	0	
	b	0.1503	850	0.25	0.810 ± 0.007	4.70 ± 0.14	85.4 ± 4.9	5.84 ± 0.17	105.4 ± 5.9	15.55 ± 0.91	50	91	17.2 ± 1.0
			1100	0.25	0.0628 ± 0.0057	0.430 ± 0.073	5.5 ± 5.2	6.8 ± 1.3	87 ± 80	1.61 ± 0.49	56	9	
	c	0.1457	850	0.25	0.738 ± 0.010	4.02 ± 0.15	76.1 ± 4.9	5.25 ± 0.19	99.8 ± 6.5	11.64 ± 0.93	42	100	11.64 ± 0.93
17-OD1-C1-235-310	a	0.1449	850	0.25	0.562 ± 0.013	2.53 ± 0.13	59.0 ± 5.6	4.44 ± 0.23	105 ± 10	5.77 ± 0.86	33	100	5.77 ± 0.86
			1100	0.25	0.040 ± 0.011	0.011 ± 0.085	5.7 ± 5.4	0.3 ± 2.1	143 ± 139	n.d	0	0	
	b	0.1564	850	0.25	0.5910 ± 0.0080	2.84 ± 0.13	59.2 ± 4.9	4.84 ± 0.22	100.2 ± 8.0	7.12 ± 0.80	39	88	8.07 ± 0.94
			1100	0.25	0.070 ± 0.005	0.356 ± 0.077	6.8 ± 5.2	5.1 ± 1.2	98 ± 72	0.95 ± 0.49	42	12	
	c	0.1654	850	0.25	0.6767 ± 0.0094	3.00 ± 0.14	68.1 ± 4.9	4.28 ± 0.20	97.7 ± 7.1	5.41 ± 0.80	30	100	5.41 ± 0.80
			1100	0.25	0.0585 ± 0.0046	0.260 ± 0.083	5.9 ± 4.8	4.3 ± 1.4	98 ± 80	n.d	0	0	

Table C. 6 Continued

Sample name	Aliquot	Aliquot weight (g)	Heating temp. (deg C)	Heating time (hr)	Total ^{20}Ne released[1] (10^9 atoms)	Total ^{21}Ne released[2] (10^6 atoms)	Total ^{22}Ne released[3] (10^6 atoms)	^{21}Ne / ^{20}Ne[4] (10^{-3})	^{22}Ne / ^{20}Ne[4] (10^{-3})	Excess ^{21}Ne this heating step (10^6 atoms g^{-1})	Excess ^{21}Ne as % of ^{21}Ne released in this heating step	Percent of total excess ^{21}Ne released in this step	Total excess ^{21}Ne (10^6 atoms g^{-1})
17-OD1-C1-310-350	a	0.1543	850	0.25	0.988 ± 0.014	3.82 ± 0.16	101.9 ± 5.7	3.81 ± 0.16	103.2 ± 5.7	5.5 ± 1.0	22	100	5.5 ± 1.0
			1100	0.25	0.097 ± 0.010	0.325 ± 0.085	8.9 ± 5.4	3.32 ± 0.92	91 ± 54	n.d	0	0	
	b	0.1435	850	0.25	1.2389 ± 0.0091	5.44 ± 0.14	127.6 ± 5.0	4.42 ± 0.11	103.0 ± 3.9	12.62 ± 0.96	33	80	15.8 ± 1.1
			1100	0.25	0.1260 ± 0.0051	0.831 ± 0.080	14.2 ± 5.0	6.57 ± 0.67	113 ± 39	3.18 ± 0.56	55	20	
	c	0.1547	850	0.25	0.9366 ± 0.0090	3.75 ± 0.15	95.2 ± 4.8	3.86 ± 0.14	98.7 ± 5.0	5.48 ± 0.85	23	87	6.3 ± 1.0
			1100	0.25	0.0731 ± 0.0085	0.356 ± 0.073	6.2 ± 4.9	4.7 ± 1.1	82 ± 66	0.82 ± 0.48	36	13	
17-OD1-C1-500-582	a	0.1461	850	0.25	0.503 ± 0.011	4.54 ± 0.15	55.1 ± 5.6	8.93 ± 0.34	110 ± 11	20.6 ± 1.0	66	100	20.6 ± 1.0
			1100	0.25	0.029 ± 0.010	0.079 ± 0.083	2.8 ± 5.7	2.7 ± 3.0	96 ± 192	n.d	0	0	
	b	0.1475	850	0.25	0.546 ± 0.010	4.63 ± 0.15	59.8 ± 5.1	8.40 ± 0.26	109.4 ± 8.9	20.18 ± 0.96	64	93	21.7 ± 1.1
			1100	0.25	0.0287 ± 0.0054	0.313 ± 0.080	4.0 ± 5.3	10.8 ± 3.4	139 ± 180	1.52 ± 0.54	72	7	
17-OD1-C1-582-649	a	0.1444	850	0.25	0.553 ± 0.011	7.01 ± 0.18	61.8 ± 5.4	12.57 ± 0.38	112.0 ± 9.8	36.9 ± 1.2	76	100	36.9 ± 1.2
			1100	0.25	0.045 ± 0.010	0.206 ± 0.088	5.2 ± 5.6	4.6 ± 2.2	115 ± 124	n.d	0	0	
	b	0.1648	850	0.25	0.5099 ± 0.0090	5.43 ± 0.16	54.6 ± 5.2	10.54 ± 0.30	106.9 ± 9.9	23.50 ± 0.93	71	96	24.4 ± 1.0
			1100	0.25	0.0527 ± 0.0056	0.312 ± 0.080	5.3 ± 5.4	5.8 ± 1.6	101 ± 99	0.92 ± 0.48	49	4	

Table C. 6 Continued

Sample name	Aliquot	Aliquot weight (g)	Heating temp. (deg C)	Heating time (hr)	Total ^{20}Ne released[1] (10^9 atoms)	Total ^{21}Ne released[2] (10^6 atoms)	Total ^{22}Ne released[3] (10^6 atoms)	^{21}Ne / ^{20}Ne[4] (10^{-3})	^{22}Ne / ^{20}Ne[4] (10^{-3})	Excess ^{21}Ne this heating step (10^6 atoms g^{-1})	Excess ^{21}Ne as % of ^{21}Ne released in this heating step	Percent of total excess ^{21}Ne released in this step	Total excess ^{21}Ne (10^6 atoms g^{-1})
	c	0.1569	850	0.25	0.4441 ± 0.0064	5.22 ± 0.19	48.5 ± 4.7	11.32 ± 0.40	106 ± 10	23.7 ± 1.1	71	100	23.7 ± 1.1
			1100	0.25	0.0320 ± 0.0062	0.168 ± 0.079	3.5 ± 4.8	5.0 ± 2.6	108 ± 148	n.d	0	0	
17-OD1-C1-781-819	a	0.1347	850	0.25	0.388 ± 0.010	7.89 ± 0.20	47.4 ± 5.4	20.15 ± 0.70	122 ± 14	49.7 ± 1.5	85	100	49.7 ± 1.5
			1100	0.25	0.018 ± 0.010	0.064 ± 0.087	2.7 ± 5.6	3.7 ± 5.2	156 ± 321	n.d	0	0	
	b	0.1369	850	0.25	0.4058 ± 0.0087	8.77 ± 0.18	51.2 ± 5.2	21.40 ± 0.49	126 ± 12	54.8 ± 1.3	86	99	55.5 ± 1.4
			1100	0.25	0.0310 ± 0.0076	0.194 ± 0.072	4.8 ± 5.3	6.2 ± 2.7	156 ± 170	0.73 ± 0.54	52	1	
17-OD1-C1-819-879	a	0.1512	850	0.25	0.381 ± 0.011	10.56 ± 0.32	53.1 ± 5.9	26.92 ± 0.88	138 ± 15	60.6 ± 1.5	87	98	61.7 ± 1.6
			1100	0.25	0.0334 ± 0.0089	0.272 ± 0.089	3.7 ± 5.8	7.9 ± 3.3	111 ± 169	1.10 ± 0.59	61	2	
	b	0.1365	850	0.25	0.392 ± 0.011	10.24 ± 0.22	48.9 ± 5.4	25.94 ± 0.85	125 ± 14	66.1 ± 1.6	88	98	67.4 ± 1.7
			1100	0.25	0.025 ± 0.010	0.264 ± 0.090	4.7 ± 5.6	10.3 ± 5.2	186 ± 224	1.37 ± 0.68	71	2	
17-OD1-C1-879-944	a	0.1472	850	0.25	0.414 ± 0.011	11.14 ± 0.35	53.9 ± 6.0	26.12 ± 0.81	129 ± 14	65.3 ± 1.7	86	100	65.3 ± 1.7
			1100	0.25	0.043 ± 0.010	0.164 ± 0.089	5.5 ± 5.6	3.7 ± 2.2	127 ± 129	n.d	0	0	
	b	0.1548	850	0.25	0.349 ± 0.010	11.55 ± 0.27	50.4 ± 5.4	32.78 ± 1.09	143 ± 15	67.5 ± 1.5	90	98	68.7 ± 1.6
			1100	0.25	0.035 ± 0.010	0.303 ± 0.087	4.2 ± 5.4	8.5 ± 3.4	119 ± 150	1.25 ± 0.58	64	2	

Table C. 6 Continued

Sample name	Aliquot	Aliquot weight (g)	Heating temp. (deg C)	Heating time (hr)	Total ^{20}Ne released[1] (10^9 atoms)	Total ^{21}Ne released[2] (10^6 atoms)	Total ^{22}Ne released[3] (10^6 atoms)	^{21}Ne / ^{20}Ne[4] (10^{-3})	^{22}Ne / ^{20}Ne[4] (10^{-3})	Excess ^{21}Ne this heating step (10^6 atoms g^{-1})	Excess ^{21}Ne as % of ^{21}Ne released in this heating step	Percent of total excess ^{21}Ne released in this step	Total excess ^{21}Ne (10^6 atoms g^{-1})

[1] Computed by comparison to ^{20}Ne signal in air standards. 1-sigma uncertainty includes measurement uncertainty of ^{20}Ne signal in this analysis and the reproducibility of the air standards

[2] Computed by comparison to ^{21}Ne signal in air standards. 1-sigma uncertainty includes measurement uncertainty of ^{21}Ne signal in this analysis and the reproducibility of the air standards

[3] Computed by comparison to ^{22}Ne signal in air standards. 1-sigma uncertainty includes measurement uncertainty of ^{22}Ne signal in this analysis and the reproducibility of the air standards

[4] Isotope ratio measured internally during each analysis and corrected for mass discrimination based on an air standard. Does not involve normalization to the Ne isotope signals in the standards, so the ratio computed from absolute Ne isotope amounts in previous columns may differ within uncertainty.

Table C. 7 Be isotope concentrations in quartz from Ong Valley surface and moraine boulders.

Sample name	Mass of quartz dissolved (g)	Chemical preparation lab	AMS lab	AMS ID	^{10}Be concentration (10^6 atoms/g)
Analyzed at UVM and PRIME					
17-OV-212-ERR	10.9563	UVM	PRIME	157717	19.09 ± 0.14
17-OV-213-ERR	5.6441	UVM	PRIME	157718	18.48 ± 0.23
17-OV-214-ERR	6.4486	UVM	PRIME	157719	18.54 ± 0.23
17-OV-215-ERR	19.1083	UVM	PRIME	157720	17.42 ± 0.14
17-OV-217-ERR	19.3843	UVM	PRIME	157721	18.11 ± 0.19
17-OV-218-ERR	19.4441	UVM	PRIME	157723	19.63 ± 0.18
Analyzed at LLNL					
11-OV-ER-117	0.9043	LLNL	LLNL	BE46147	25.15 ± 0.43
11-OV-ER-118	1.0429	LLNL	LLNL	BE46148	27.49 ± 0.46
11-OV-ER-119	1.0493	LLNL	LLNL	BE46149	28.28 ± 0.45

Notes:

1. Samples analyzed at UVM/PRIME reflect a blank subtraction of 88000 +/- 31000 atoms ^{10}Be (< 0.1% of total atoms present).

2. Samples analyzed at LLNL reflect a blank subtraction of 24000 +/- 3000 atoms ^{10}Be (< 0.2% of total atoms present).

3. ^{10}Be concentrations are normalized to the '07KNSTD' standardization of Nishiizumi et al. (2007).

Table C. 8 Step-degassing Ne isotope measurements for boulder samples from Ong Valley middle drift. Run on BGC "Ohio" system in 2015 and 2019.. Note: "n.d" = not detected.

Sample name	Aliquot	Aliquot weight (g)	Heating temp. (deg C)	Heating time (hr)	Total ^{20}Ne released[1] (10^9 atoms)	Total ^{21}Ne released[2] (10^6 atoms)	Total ^{22}Ne released[3] (10^6 atoms)	^{21}Ne / ^{20}Ne[4] (10^{-3})	^{22}Ne / ^{20}Ne[4] (10^{-3})	Excess ^{21}Ne this heating step (10^6 atoms g^{-1})	Excess ^{21}Ne as % of ^{21}Ne released in this heating step	Percent of total excess ^{21}Ne released in this step	Total excess ^{21}Ne (10^6 atoms g^{-1})
1. Analyzed September 2019. Concomitant analyses of CRONUS-A yielded 320.9 +/- 6.1 Matoms/g excess ^{21}Ne.													
17-OV-212-ERR	a	0.1487	850	0.25	0.483 ± 0.019	19.25 ± 0.79	67.9 ± 2.8	39.27 ± 0.92	140.1 ± 4.1	119.8 ± 5.3	93	99	120.8 ± 5.3
			1100	0.25	0.0794 ± 0.0090	0.377 ± 0.040	6.6 ± 1.2	4.72 ± 0.69	84 ± 17	1.0 ± 0.3	38	1	
17-OV-213-ERR	a	0.1584	850	0.25	0.349 ± 0.014	17.82 ± 0.73	53.3 ± 2.4	50.4 ± 1.4	152.3 ± 5.4	106.0 ± 4.6	94	100	106.3 ± 4.6
			1100	0.25	0.032 ± 0.010	0.149 ± 0.032	2.7 ± 1.1	4.6 ± 1.8	82 ± 44	0.3 ± 0.3	36	0	
17-OV-214-ERR	a	0.1566	850	0.25	2.099 ± 0.070	24.8 ± 1.0	230.3 ± 8.5	11.64 ± 0.14	109.50 ± 0.90	118.4 ± 6.6	75	92	129.0 ± 6.7
			1100	0.25	0.673 ± 0.023	3.65 ± 0.17	69.9 ± 2.9	5.40 ± 0.16	103.6 ± 2.5	10.6 ± 1.2	45	8	
2. Analyzed November 2019. Concomitant analyses of CRONUS-A yielded 323 +/- 17 Matoms/g excess ^{21}Ne.													
17-OV-215-ERR	a	0.1603	850	0.25	0.232 ± 0.011	16.45 ± 0.62	41.8 ± 2.0	70.7 ± 2.5	180.6 ± 7.8	98.3 ± 3.9	96	99	99.1 ± 3.9
			1100	0.25	0.0286 ± 0.0055	0.215 ± 0.033	2.6 ± 1.1	7.5 ± 1.8	92 ± 43	0.8 ± 0.2	61	1	
17-OV-217-ERR	a	0.1674	850	0.25	0.331 ± 0.014	24.11 ± 0.86	60.8 ± 2.7	72.7 ± 1.6	184.4 ± 5.5	138.2 ± 5.2	96	100	138.3 ± 5.2
			1100	0.25	0.0314 ± 0.0062	0.122 ± 0.028	3.1 ± 1.1	3.9 ± 1.2	99 ± 41	0.2 ± 0.2	24	0	
17-OV-218-ERR	a	0.1729	850	0.25	0.485 ± 0.019	28.0 ± 1.0	79.6 ± 3.5	57.7 ± 1.1	164.7 ± 4.3	153.8 ± 5.8	95	100	154.2 ± 5.8
			1100	0.25	0.0611 ± 0.0064	0.246 ± 0.035	5.6 ± 1.2	4.00 ± 0.66	92 ± 21	0.4 ± 0.2	26	0	
3. Analyzed August 2015. Concomitant analyses of CRONUS-A yielded 313.4 +/- 9.0 Matoms/g excess ^{21}Ne.													
11-OV-ER-117	a	0.1286	400	0.25	0.162 ± 0.010	22.4 ± 1.1	42.2 ± 2.2	137.3 ± 6.9	254 ± 15	169.7 ± 6.8	97	82	206.2 ± 7.0
			850	0.25	0.243 ± 0.012	5.46 ± 0.30	30.3 ± 1.9	22.25 ± 0.90	121.5 ± 7.2	36.6 ± 1.7	86	18	

Table C. 8 Continued

Sample name	Aliquot	Aliquot weight (g)	Heating temp. (deg C)	Heating time (hr)	Total ^{20}Ne released[1] (10^9 atoms)	Total ^{21}Ne released[2] (10^6 atoms)	Total ^{22}Ne released[3] (10^6 atoms)	^{21}Ne / ^{20}Ne[4] (10^{-3})	^{22}Ne / ^{20}Ne[4] (10^{-3})	Excess ^{21}Ne this heating step (10^6 atoms g^{-1})	Excess ^{21}Ne as % of ^{21}Ne released in this heating step	Percent of total excess ^{21}Ne released in this step	Total excess ^{21}Ne (10^6 atoms g^{-1})
			1150	0.2	0.029 ± 0.010	0.131 ± 0.049	4.6 ± 1.4	4.5 ± 2.3	154 ± 69	n.d.			
11-OV-ER-118	a	0.1517	400	0.25	0.764 ± 0.030	21.7 ± 1.1	96.6 ± 4.2	28.15 ± 0.52	123.6 ± 2.9	127.1 ± 5.1	89	66	191.7 ± 5.8
			850	0.25	1.029 ± 0.038	12.81 ± 0.66	116.7 ± 4.9	12.34 ± 0.22	110.5 ± 2.0	63.8 ± 2.7	75	33	
			1150	0.2	0.243 ± 0.012	0.856 ± 0.084	26.3 ± 1.8	3.49 ± 0.31	105.5 ± 6.9	0.9 ± 0.5	15	0	
	b	0.1385	400	0.25	0.755 ± 0.028	21.5 ± 1.1	95.8 ± 4.0	28.41 ± 0.50	123.4 ± 2.9	139.1 ± 5.3	89	71	195.6 ± 5.8
			850	0.25	0.910 ± 0.034	10.35 ± 0.55	100.6 ± 4.3	11.37 ± 0.21	107.7 ± 2.3	55.4 ± 2.3	74	28	
			1150	0.2	0.201 ± 0.011	0.739 ± 0.076	21.2 ± 1.6	3.73 ± 0.36	102.9 ± 7.8	1.1 ± 0.5	21	1	
11-OV-ER-119	a	0.1389	400	0.25	0.251 ± 0.013	15.25 ± 0.78	41.7 ± 2.2	60.2 ± 2.5	162.5 ± 8.4	103.7 ± 4.4	94	57	181.4 ± 5.5
			850	0.25	0.198 ± 0.011	11.46 ± 0.61	33.9 ± 2.0	57.2 ± 2.6	166 ± 10	77.7 ± 3.3	94	43	
			1150	0.2	0.0174 ± 0.0075	0.032 ± 0.038	2.2 ± 1.3	1.8 ± 2.3	125 ± 91	n.d.			

[1] Computed by comparison to ^{20}Ne signal in air standards. 1-sigma uncertainty includes measurement uncertainty of ^{20}Ne signal in this analysis and the reproducibility of the air standards

[2] Computed by comparison to ^{21}Ne signal in air standards. 1-sigma uncertainty includes measurement uncertainty of ^{21}Ne signal in this analysis and the reproducibility of the air standards

[3] Computed by comparison to ^{22}Ne signal in air standards. 1-sigma uncertainty includes measurement uncertainty of ^{22}Ne signal in this analysis and the reproducibility of the air standards

[4] Isotope ratio measured internally during each analysis and corrected for mass discrimination based on an air standard. Does not involve normalization to the Ne isotope signals in the standards, so the ratio computed from absolute Ne isotope amounts in previous columns may differ within uncertainty.

APPENDIX D

EXPLANATION OF ^{10}BE AND ^{26}AL NUCLIDE EXTRACTION PROCEDURES

Explanation of Beryllium and Aluminium Extraction Process

By

Marie Bergelin

Introduction

Cosmogenic nuclide dating is a widely used application in geosciences. Therefore, many research scientists are extracting either or both beryllium (Be) and aluminium (Al) from geological samples to be analyzed for the cosmogenic nuclide ^{10}Be and ^{26}Al by Accelerator Mass Spectrometry. The steps for such extraction procedure are performed almost daily across various cosmogenic nuclide laboratories and in most cases by undergraduate or graduate students.

One of the widely used extraction manuals by (Stone, 2004) has been adopted and modified by many laboratories. However, most of these manuals provide limited details and explanations for the chemical reasoning behind each step outlined in the manuals. The University of Vermont/National Science Foundation (UVM/NSF) Community Cosmogenic Facility is a cosmogenic nuclide laboratory dedicated to train students at a graduate level in sample processing and nuclide extraction techniques while also developing and freely disseminate sample processing methods. Therefore, the motivation for this document is to provide students working in these cosmogenic nuclide laboratories with an understanding of each step involved in the extraction of Be and Al.

In collaboration with the University of Vermont/National Science Foundation (UVM/NSF) Community Cosmogenic Facility, we have created a document that provides a detailed explanation for why each step is performed and their importance, which ultimately leads to the successful extraction of both beryllium and aluminium. Further, it provides details of the chemical reactions that occur and eventually cause Be and Al's isolation. Specifically, this document follows the steps outlined in the ‘Be/Al extraction manual’ published by the UVM/NSF Community Cosmogenic Facility.

Chemical Abbreviations

Al	Aluminium (Isotopes: ^{26}Al, ^{27}Al)	$HClO_4$	Perchloric acid
Al_3O_3	Aluminum oxide	HF	Hydrofluoric acid
$Al(OH)_3$	Aluminium hydroxide	HNO_3	Nitric Acid
B	Boron	H_2O	Water
Be	Beryllium (Isotopes: ^{9}Be, ^{10}Be)	H_2O_2	Hydrogen peroxide
$Be(ClO_4)_2$	Beryllium perchlorate	H_2SiF_6	Hexafluorosilicic acid
$BeCl_2$	Beryllium chloride	H_2SO_4	Sulfuric acid
BeO	Beryllium Oxide	K	Potassium
$Be(OH)_2$	Beryllium hydroxide	Mg	Magnesium
Ca	Calcium	NH_4OH	Ammonium hydroxide
Ca^{2+}	Calcium ion	Na	Sodium
Cl	Chlorine	Nb	Niobium
Cl^-	Chloride	O	Oxygen
ClO_4^-	Perchlorate	O_2	Dioxide
F	Fluorine	SO_4^{2-}	Sulfate
F^-	Fluoride	Si	Silicon
Fe	Iron	SiF_4	Silicon tetrafluoride
Fe^{3+}	Ferric ion	SiO_4	Quartz (silica)
$FeCl_4^-$	Tetrachloroferrate (Others: $FeCl_5^{2-}$ and $FeCl_6^{3-}$)	Ti	Titanium
Ga	Gallium	$Ti^{(IV)}Cl_6^{2-}$	Titanium hexachloride
H	Hydrogen	TiO_2	Titanium dioxide
H_2	Dihydrogen	Y	Yttrium
HCl	Hydrochloric acid		

Final Etching

- *Preform a final etching of the samples*. Prior to arriving at University of Vermont (UVM) cosmogenic laboratory, the samples were cleaned in 2% HF and rinsed in DI water. At UVM, all samples will need to undergo an additional final etching in which the samples are cleaned in hydrofluoric acid (HF) and nitric acid (HNO_3) over night and then rinsed in mill-q water and dried in an oven. This final cleaning, which occurs in the clean laboratory, in Teflon, and using milli-q ultra-pure water, allows for removal of any background contamination or atmospheric beryllium (Be) or aluminium (Al) that may have been picked up at laboratories using less clean water.

Weighing in Quartz

- *Weigh the samples*. This is important when calculating the concentration of ^{10}Be and ^{26}Al in the end as the concentration is based on the total amount of quartz mass. The sample mass should not exceed 22g; if a greater mass of quartz is used, the sample will not be fully digested in hydrofluoric acid. The Accelerator Mass Spectrometer (AMS) is able to detect isotope ratios of $^{10}Be/^{9}Be > 10^{-15}$ and $^{26}Al/^{27}Al > 10^{-15}$; if the approximate cosmogenic nuclide concentrations or age of the samples are known, the amount of quartz needed can then be calculated, keeping in mind that greater numbers of counts of the rare isotopes will yield higher-precision analyses.

- *Spike the samples with ^{27}Al carrier*. The samples should be spiked with ^{27}Al carrier such that a sample will have an Al total of 1500 μg. The amount of ^{27}Al carrier needed is calculated based on the amount of native ^{27}Al in the quartz quantified by Inductively Coupled Plasma Optical Emission Spectroscopy (ICP-OES).

- *Spike the samples with ^{9}Be carrier.* The samples are spiked with 250μg of ^{9}Be carrier. This is to provide sufficient total material for handling in the laboratory and to allow for $^{10}Be/^{9}Be$ ratio measurements by AMS. Because quartz only rarely contains native ^{9}Be (an assumption we will verify later in the process), all samples receive the same ^{9}Be spike.

- *Moisten the samples.* A few mL of milli-q water should be added to the sample before adding hydrofluoric acid to the sample. The water is added such that it completely moistens the sample. This is done to minimize the chance of a reaction between hydrofluoric acid and the quartz, and also to ensure that the isotopes added via carrier do not dry and volatize.

- *Create a UVM-A sample:* This quality control material, which was created at UVM, has a known $^{10}Be/^{9}Be$ and $^{26}Al/^{27}Al$ ratios. This serves as a control sample during AMS analyses and can help constrain uncertainty. It also may serve as an inter-laboratory comparison standard in the future. At UVM, one "UVM-A" quality control standard is processed alongside ever batch of samples.

- *Create a blank:* This is a blank sample which does not contain any quartz. If should contain very few of the rare isotopes. Carrier of the stable isotopes are added (~250 μg ^{9}Be and ~1500 μg ^{27}Al) as a known amount. Any measured rare isotopes are from (1) the carriers themselves, (2) contamination in the laboratory, and/or (3) background levels of the AMS. The measured ratio is used to correct for backgrounds and will be subtracted from the measured ratios of each sample. The spatial positions of the quality control standard and blank within a batch is rotated with every batch to appropriately quantify any rare isotopes introduced during column chemistry.

Adding Acid to Quartz

- *Add 100mL of 50% HF to the samples*. Concentrated hydrofluoric acid is added to fully digest the quartz samples. The amount of hydrofluoric acid needed should be about 5 times the mass of quartz added, such that 100 mL digest a max of about 20g of quartz based on the reaction between silica and hydrofluoric acid.

Quartz Digestion

- *Increase the temperature in stages.* During a full week, the temperature for the quartz digestion should be gradually increased from 65°C to 135°C. The increased temperature speeds up the digestion process. The reaction of quartz and hydrofluoric acid is an exothermic reaction in which energy is released in the form of heat. If temperature is increased too quickly, the reaction becomes uncontrolled and can release acid and Be into the hood, representing significant safety and contamination hazards.

  The following reaction is occurring:

  $SiO_{2\,(s)} + 6\ HF_{(l)} \rightarrow H_2SiF_{6\,(l)} + 2\ H_2O_{(l)}$

Removing ICP Aliquots

- *Take a 2mL and 4mL aliquot from the digested samples.* Two aliquot samples of different sizes are taken for ICP analysis. These aliquots are used to quantify the total Be and Al at high precision with ICP-OES. The aliquots are massed and represent ~2% and ~4% of the total sample mass. The AMS will measure a ratio of ^{10}Be/^{9}Be or ^{26}Al/^{27}Al. The total Be and Al measured by the ICP in the aliquots, which are the denominators of these measured ratios, are then used to calculate the total ^{10}Be and ^{26}Al in each sample. Usually, the sample only contains the ^{9}Be added as a carrier. However, infrequently quartz can contain native ^{9}Be, in which case it is critical to identify and correct for using the ICP data. Native ^{9}Be is most common in pegmatite lithologies but is occasionally present in other lithologies as well.

Two aliquots are taken from each sample such that an average can be used for the final concentration in a sample. If an error occurs during the aliquot preparation or measurement, then one serves as a back-up, such that the sample does not become lost. Further having two different sizes of the aliquots (2mL and 4mL), allows for the ICP to measure in two different places on the calibration curve.

- *Add 25µL of H_2SO_4.* Evaporation of sulfuric acid (H_2SO_4) only occurs at very high temperatures. H_2SO_4 is added such that when the ICP aliquots are dried down, the samples do not reach dryness while evaporating hydrofluoric acid. If H_2SO_4 is not added and the samples are completely dried, static build up could cause the dried down sample to fly out of the beaker and the aliquot would be destroyed. Adding H_2SO_4 also keeps all of the cations in solution, which facilitates complete redissolution.

- *Dry samples and aliquots overnight.* The samples and aliquots are dried down at 150°C and most of the fluoride will be evaporated as SiF_4 as the following reaction will take place:

$$H_2SiF_{6\,(l)} \rightarrow \text{heat} \rightarrow SiF_{4\,(g)} + 2HF_{(g)}$$

In addition, any water will also evaporate. At this stage, many of the cations in the sample are still bound with fluoride. It is critical to break apart these bonds so that the rest of the lab chemistry works properly. Therefore, the next steps will focus on perchloric acid ($HClO_4$) treatments of the samples to break the fluoride bonds.

- *Add 5 mL of Ga/Y spiked H_2SO_4 to the ICP aliquots*. The ICP aliquots are diluted in a Ga/Y spiked 0.5% H_2SO_4. This dilutant is very precisely spiked with 10ppm gallium (Ga) and yttrium (Y), which act as an internal standard and is used to correct for any instrumental drifts in the ICP.

  About 2mL of solution is needed to run a sample on the ICP under the aliquot method. The sample is diluted in 5mL H_2SO_4 solution such that if something goes wrong with the ICP, there is enough sample to re-run the sample and prevent data from being lost.

- *Let the samples sit for an hour*. This is to make sure that the sample contained in the H_2SO_4 droplet goes into complete solution as the acid is viscus.

ICP Measurements

This method is designed for high-precision analyses and is only run when the ICP is performing optimally. First, a calibration curve is built by measuring a blank, 1 ppm, 2 ppm, 4 ppm and 8 ppm standards for Be, and a blank, 10 ppm, 20 ppm, 40 ppm, and 80 ppm standards for Al. The standards all contain 10 ppm Ga and Y similar to our aliquots for the purposes of internal

standardization and drift correction. The same standards are then re-run as unknowns in order to check ICP performance. Only if the calibration curve and the standards re-run as unknows are in agreement, the samples are analyzed. The 2 mL samples are run first, then the standards again as unknowns, then the 4mL samples, and then the standards as unknowns at the end.

Perchloric Acid Drydowns

- *Add perchloric acid (four different times: 3 x 2mL and 1 x 4mL) to the samples*. During evaporation of fluoride, perchloric acid is added to the sample. The cations in the sample (including Be and Al) bond strongly with fluoride. Perchloric acid is added to break up this strong bond, such that the cations are bonding with the perchlorate (ClO_4^-). Any fluoride left in the sample (fluoride bonded to cations) will cause problems when preforming column chemistry as the cations will not be able to bond with the resin and be contained in the column during separation.

  The following reactions are occurring during evaporation of fluoride

  $H_2SiF_{6\,(l)} + 2\,H_2O_{\,(l)} \rightarrow \text{heat} \rightarrow SiF_{4\,(g)} + 2HF_{\,(g)} + 2H_{2\,(g)} + O_{2\,(g)}$

- *Dry samples on hotplate.* The samples are evaporating at 230°C to break up and drive off fluoride compounds.

Chloride Conversion

- *Add 2mL concentrated HCl to the samples.* Currently the cations (ex. Be and Al) are bonded with perchlorate; cation + ClO_4^- (ex. $Be(ClO_4)_2$). Adding hydrochloric acid (HCl) forces the cations to bond with chlorine through the reaction $Be(ClO_4)_2 + 2HCl \text{ —> } BeCl_2 + H_2O$. The cations want to bond with Cl^- rather than ClO_4^-. Having the cations in the proper form is important for the anion column method, which occurs in HCl.

- *Dry samples on hotplate.* The samples are dried for 90 min at 160°C. This drives off some of the water produced during chloride conversion.

Sample preparation for Anion Column

- *Add 5mL of 6N HCl to the samples*. The sample should be in strong (6N) HCl so that, upon interacting with the column resin, any iron (Fe) will bind to the resin and stay behind in the column. This dilution is done in two parts; an initial dilution and then a rinse of the beaker in order to quantitatively transfer all cations. The samples will change color on a spectrum of clear to yellow, where yellow indicates greater presence of Fe. The samples may also develop a cloudy, white precipitate which contains some (but not all) of the titanium (Ti) in the sample in the form of titanium dioxide (TiO_2). The blank should be completely clear since it contains neither Fe nor Ti.

- *Centrifuge the samples*. The samples are centrifuged to remove heavier and less soluble elements such as TiO_2 and any insoluble fluorides that may exist in the sample still, and occasionally any

mafic minerals which was stuck in the quartz grains as impurity. Any insoluble fluorides will cause problems for the column chemistry, as the anions are not able to bond with free cations in the column and could block the columns. No Al or Be is co-precipitated with the Ti and it is therefore removed by centrifuging before the anion exchange.

Anion Columns

The 3 mL anion columns contain Dowex 1X8 200e400 mesh resin and are built at UVM. The purpose of anion column chemistry is to remove Fe from the sample. The resin in the column either binds to or releases Fe, depending on the acid strength.

- *Drain the water from the anion columns*. The columns are stored containing milli-q water such that the resin always remains saturated.

- *Add 5 column volumes (15mL) 1.2N HCl*. This strips the column and releases any ions that may still be in the column. At this point all anions should have been released through column stripping after previous batch. However, this step is done as precaution that no previous residual is present.

- *Adding 3 column volumes (9 mL) 6N HCl*. Adding 6N HCl conditions the columns and saturates the pore space in the column. The conditioning has the same HCl strength as the samples. At this acid strength, the Fe in the samples will bind to the resin, allowing for Fe to be removed from the other cations in the samples.

- *Place the sample beakers under the columns.* Because Be and Al will pass through the resin as soon as the sample is loaded into the column, they need to be captured in Teflon beakers.

- *Load the sample into the column*. The samples are loaded into the column by pipette, leaving behind any precipitates at the bottom of the centrifuge tube to avoid any plugging of the column by precipitates. The sample, which is dissolved in a 6N HCl solution, will run into the column where some will be retained, and some will drain through. In strong HCL, Fe^{+3} forms a range of anionic chloride complexes; $FeCl_4^-$, $FeCl_5^{2-}$ and $FeCl_6^{3-}$. These anionic complexes bonds tightly to the anion exchange resin. Be and Al do not form strong chloride (Cl^-) complexes and elute from the column with the HCl. Some Ti in the form of $Ti^{(IV)}Cl_6^{2-}$ will bind, but most will drain through as cationic or neutral species, ending up with the sample containing Be and Al.

- *Add 3 column volume (9mL) 6N HCl after the sample has fully drained into the column*. This will ensure that all of the sample material (excluding the Fe) will be forced down through the resin and into the sample beakers. Since the same strength of HCl is used, the anionic complexes will remain in the resin and the non-binding cations will be eluted. At this point, the sample beakers are removed and placed onto the hot plate to dry overnight.

- *Add 5 column volumes of 1.2N HCl.* Adding a weaker acid to the column will strip the column, causing Fe(iii) chloride complexes to break up. Fe, along with potentially other cations previously retained in the column, will be released from the column, and discarded. This step serves to clean the columns and prepare them for the next use.

- *Add full column reservoir with milli-q water*. The column is washed through with milli-q water and stored in a 1 column of milli-q water for the next use.

Post-Anion Column

- *Add 140µL H_2SO_4 to each sample very precisely.* There are two reasons for why H_2SO_4 is added: (i) so that the samples do not reach dryness and is dried down to a droplet of H_2SO_4, and (ii) a sample having a 0.65M H_2SO_4 strength is needed for cation column chemistry the following day. The sample will eventually be loaded into the cation column with 4 mL of milli-q water; adding 140µL of H_2SO_4 will result in a desired 0.65M H_2SO_4 strength. This acid strength dictates the rate at which ions will move through the column, so the precision is critical for optimal cation column performance.

- *Dry the samples overnight*. The HCl is driven off at a sub-boiling temperature overnight.

- *Check for crystals*. If enough calcium ions (Ca^{2+}) are present in the sample, gypsum ($CaSO_4 \cdot 2H_2O$) are able to precipitate during evaporation. This is the first time the sample is introduced to H_2SO_4, in which sulfate (SO_4^{2-}) is present to form sulfate minerals. If this occurs, any samples with precipitate will need to be centrifuged to avoid damaging the columns. Samples having > 50 ppm of Calcium (Ca) will most likely have gypsum precipitate. Samples will be diluted in the same fashion as described below but transferred to a 15mL centrifuge tube instead of directly into the column. It is usually easier to handle any centrifuging needs in advance since that takes additional time if not.

Cation Columns

The 5 mL cation columns contain Dowex 50WX8 200e400 mesh resin and are built at UVM. The purpose of cation column chemistry is to separate Ti, Be, Mg, and Al.

- *Drain the water from the cation columns*. The columns are stored containing milli-q water such that the resin remains saturated.

- *Add 5 column volumes of 0.65M H_2SO_4*. This solution conditions the column such that the column resin becomes saturated with the same acid type and strength of the samples. The H_2SO_4 is spiked with hydrogen peroxide (H_2O_2), similar to the sample (see following steps), which serves to stain the Ti yellow/orange/red.

- *Prepare and then load the samples one at a time.* Because the acid strength is so important in this method, we do not want to dilute the samples in advance since evaporation will alter the acid strength. Work one sample at a time, diluting and then immediately loading into the column.

- *Add 7 drops of 2% H_2O_2*. Once the H_2O_2 is added, the sample may take on an amber/gold-red color. This color change occurs in the presence of Ti bonding as $TiO[H_2O_2])^{2+}$.

- *Load the sample into the column with 4mL of milli-q water with traces of H_2SO_4.* A total of 4 mL of milli-q is added to each sample, which, when combined with the 140 µL of concentrated H_2SO_4 added the day before, results in 0.65M H_2SO_4. The sample is loaded in two stages of 2mL milli-q; first 2 mL is used to dissolve the sample and transfer it to the column, then an additional 2mL is used as a washing to make sure all of the sample is being transferred to the column and not left behind in the beaker. This last step needs to be done quickly such that the sample gets mixed in the column and reaches a strength of 0.65M H_2SO_4 before passing through the cation column resin. Since the cation column chemistry is based on both solution acidic strength and volume, any changes to this could result in a poor separation of Ti and Be in the column resin. Allow the sample to drain into the column fully.

- *Place the Ti beakers under their respective columns. Then, once the sample has completely drained into the column resin, add 5.75 column volumes of 0.65M H_2SO_4.* Adding 0.65 M H_2SO_4 will cause the Ti to unbind from the resin and move downward through the column and into the beakers. Visually, an orange band can be observed moving through the column resin. $TiO[H_2O_2])^{2+}$ has a lesser charge than Be and Al, so the Ti ion will therefore pass through the column faster than Be and Al with a lesser acid strength. Afterward, remove the Ti beakers and set aside. The Ti fractions are saved until the following day until after the sample yield and purity have been verified, in case there are any problems with the sample. In the very rare occurrence of a column failure, Be can be recovered from the Ti fraction; however, in the vast majority of cases, the Ti fractions will be discarded to waste.

- *Place the Be beakers under their respective columns, then add 5 column volumes of 1.2N HCl.* Once all the Ti has moved through the column, a stronger acid of 1.2N HCl is added, which allows for Be to be eluted. Acid of this type and strength causes the Be ions to unbind from the resin and elute downward and ultimately into the sample beakers. Al, which binds much more strongly onto the resin, will stay behind. Afterward, the Be beakers get moved to the hot plate to evaporate overnight.

- *Add 10 column volumes of 1.2N HCl.* Once all the Be has been eluted, an additional 10 column volume of 1.2N HCl will cause Mg to follow, while Al is still retained in the column resin. Be and Mg has similar ionic strength properties. However, Mg runs slightly slower through the column. Therefore, the acidic strength is not changed, but the volume increased. Eluting of Mg is only important if the Al fraction of the sample is going to PRIME because, at charge state used by the PRIME AMS, a ^{26}Mg isobar will interfere with ^{26}Al detection. Mg is trapped in the waste tray and discarded.

- *Place the Al beakers under their respective columns, then add 4 column volume of 4N HCl.* Increasing the strength of HCl causes Al to be eluted from the column. The stronger acid causes the bonding between Al and the resin to weaken, and Al is released through the column and captured. This is the last step of the process because the Al binds most strongly with the resin. Afterward, the Al beakers get moved to the hot plate to evaporate overnight.

- *Add 4 column volumes of 4N HCL*. This final addition of stronger acid strips the column and releases any lingering cations. Because the columns are re-used from one batch to another, this serves as a final cleaning step before the next use.

- *Add a full column reservoir of milli-Q water.* The column is washed through with milli-Q water and stored in a 1 column of milli-Q water for next use.

Post-Cation Column

- *Dry Be and Al samples overnight to evaporate the HCl*. This will result in Be sample containing a droplet of H_2SO_4 left over from the column procedure. The Al sample will be in the form of a smaller white solid cake.

Redissolving

- *Add 8 mL of 1% HNO_3 to both the Be and Al samples*. This acid addition dilutes the samples and prepares them for quality control checking and pH-specific precipitation. The samples get capped, vortexed, and transferred to new, acid-washed 15mL centrifuge tubes. There is not a specific reasoning for using HNO_3 as opposed to any other acid. The goal of this step is to dilute the sample enough such that it can be neutralized in the following steps for precipitation of Be and Al. However, HCl is not feasible, and could cause issues during the AMS analysis if Cl is present in the sample.

Removing Yield Testing Aliquots

- *Remove 200μL and 50μL aliquots from the Be and Al samples, respectively.* A small amount of each sample is removed and diluted in 5mL H_2SO_4 for ICP analysis. This is to confirm that the separation of Ti, Be, and Al was successful, and that Be and Al is present in their respective sample beakers before proceeding. The reason for adding 5mL of volume is so that the ICP will have enough total aliquot sample to run, and so both the Be and Al concentrations will be diluted enough to be detected within the calibration range for the ICP. We verify that all Be and Al fractions are high-yield and pure before proceeding.

Precipitating and washing Hydroxide Jells

The purpose of the following steps force Be- and Al- hydroxide ($Be(OH)_2$ and $Al(OH)_3$) to form as gel and precipitate out of solution. For both Be and Al, this occur approximately at a pH of 8; this is the pH at which the solubility of both elements is at its minimum. Performing this precipitation rejects Ca, Na, and K, which remain in solution at pH 8.

- *Add a drop of methyl red.* Methyl red is a liquid pH indicator; it is red in acidic solution and green in basic solution. The color transition happens at a neutral pH of 7.

- *Add 10-15 drops of 30% NH_4OH to the Be samples and 3-5 drops to the Al samples*. Keep adding drops of ammonium hydroxide (NH_4OH) one at a time until the color changes from red/pink to yellow/green. This color transition should occur at a neutral pH of 7. Since the Be samples

contain H_2SO_4 in addition to nitric acid, they will require a more amount of a base to neutralize. It is important to perform this step slowly and gradually so as to avoid over-shooting; a pH that is too high will allow the Be and Al to become soluble again.

- *After the color change, add 1 extra drop of 30% NH_4OH to the sample.* After a pH of 7 is reached, an additional drop of 30% NH_4OH is added. This brings the solution to an approximate pH of 8, at which both Be and Al will form a hydroxide ($Be(OH)_2$ and $Al(OH)_3$) gel. Let the sample sit for an hour to ensure that the reaction has gone to completion.

- *Centrifuge samples for 10 min*. Centrifuging the sample will cause a small amount of clear gel to collect at the bottom of the sample tubes. This gel contains all the precipitated $Be(OH)_2$ and $Al(OH)_3$ for the corresponding samples. Because all of the samples contain the same mass of Be, the gels should all look the same. The Al gels, however, will be of varying sizes due to the different masses of total Al.

Drying Hydroxide Jells into Pellets

- *Decant the liquid from sample tubes*. At a pH of 8, all of the Be and Al in a sample should be in a hydroxide solid solution. Therefore, the remaining liquid is waste and can be discharged.

- *Wash with 8mL milli-Q water, vortex, and centrifuge the samples again, then pour off all of the liquid*. Washing the hydroxide gel in milli-Q water will rinse out the added methyl red pH indicator and remove any soluble cations such as K, Na and Ca that did not precipitate into the gels. It is important to move through this step efficiently as water has a lower pH than the solubility minimum of Be and Al. All of the water must be decanted such that only the gel is left at the bottom of the sample tubes. This is an important step for when drying the gel into pellets; minimizing the amount of leftover liquid will help the sample condense into a single, easy-to-handle pellet.

- *Dry down the hydroxide gel with increasing temperature of 65℃ - 98℃.* The gel is dried into a pellet. This is done in two temperature increments in order to retrieve all of the Be- and Al-hydroxide from the tube. The lower temperature step drives liquid out of the gel and condenses it into a pellet; the higher temperature step drives off any additional liquid from the walls of the centrifuge tubes.

Packing of Cathodes

This final step converts the samples from a hydroxide into an oxide form, then prepares the sample for AMS analysis. Due to the hazardous nature of Beryllium oxide (BeO), this process is never done by students.

- *Transfer the hydroxide pellets into quartz crucibles.* The crucible is a uniquely made quartz glass crucible which is free of boron. A Boron (B) free crucible is important as B and Be have similar mass and are difficult to separate during AMS. The dried hydroxide pellets are transferred to the quartz crucibles one at a time using purpose-built stainless-steel funnels.

- *Burn the Beryllium hydroxide pellets over a torch or in a furnace*. $Be(OH)_2$ dehydrates to form a soluble white powder of BeO. This is carcinogenic and represents a significant health hazard.

  $Be(OH)_2 \rightarrow heat \rightarrow BeO + H_2O$

- *Burn the Aluminium hydroxide pellets over a torch or in a furnace*. $Al(OH)_3$ dehydrates to form aluminium oxide (Al_2O_3).

  $2Al(OH)_3 \rightarrow heat \rightarrow Al_2O_3 + 3H_2O$

- *Add Niobium to the oxides*. Powdered Niobium (Nb) metal is added to help ionize the Be and Al during AMS analysis.

- *Break up the beryllium-/aluminium- oxide and niobium in the quartz crucible*. The oxide pellets and the Nb metal need to be gently broken up and mixed into a fully homogenized powder in order to ensure complete and even ionization on the AMS.

- *Pack the powder into cathodes.* This is the very last step in which the Be- and Al oxides are packed into the cathodes and shipped to the AMS lab. There are many AMS labs around the world, all of which have different types of cathodes; hence, the cathode-packing process is AMS specific.

References

Stone, J., 2004. Extraction of Al and Be from quartz for isotopic analysis. UW Cosmogenic Nuclide Lab Methods and Procedures, 1-8.